Synthesis and Characterization of Mn-based Spinels Grown by Molecular Beam Epitaxy

by

Miles Blanchet

A dissertation submitted to the Graduate Faculty of
Auburn University
in partial fulfillment of the
requirements for the Degree of
Doctor of Philosophy

Auburn, Alabama
May 7, 2022

Keywords: Thin Film, Molecular Beam Epitaxy, Manganese Spinel, Stoichiometry Map, Material Characterization, X-ray Spectroscopy

Approved by

Dr. Ryan Comes, Chair, Assistant Professor, Department of Physics
Dr. Byron H. Farnum, Assistant Professor, Department of Chemistry and Biochemistry
Dr. Marcelo Kuroda, Associate Professor, Department of Physics
Dr. David Maurer, Professor, Department of Physics
Dr. Minseo Park, Professor, Department of Physics

Abstract

A developed energy infrastructure that relies predominately on renewable energy is critical to the longevity of society. Water-splitting and fuel cell devices will have a place in this infrastructure, although this technology is still in its infancy. Implementation of this technology on a global scale requires effective devices that are also economically feasible to manufacture. Modern fuel cell devices incorporate effective but expensive material components such as platinum and iridium to perform at high levels, hindering their wide-spread use. However, recent investigations into metal-oxide spinel materials containing elements such as iron, cobalt, nickel and manganese have demonstrated their potential for use in fuel cell technology as an inexpensive alternative to precious metals. Despite their importance in catalysis and fuel cell research, many of these materials are understudied on the basic material property level. Studies on these materials from a thin film perspective are particularly sparse. A thorough understanding of these materials is essential for their implementation in water splitting and fuel cell technology. In order to investigate the properties of these important materials and facilitate their future use as catalysts, samples were synthesized using molecular beam epitaxy and studied using a wide array of characterization techniques.

$MnFe_2O_4$ single-orientation samples were grown with different crystal orientations in order to observe this effect on the material's catalytic properties. While $MnFe_2O_4$'s properties are widely understood in literature, this study is the first to investigate the oxygen reduction reactivity properties of $MnFe_2O_4$ grown as an epitaxial thin film. Single-crystalline $CoMn_2O_4$ and Co-rich $Co_{x+1}Mn_{2-x}O_4$ samples were grown and studied, and the material's electronic properties were found to be constant despite variable stoichiometry. X-ray photoelectron and absorption spectroscopy revealed tetrahedral Co^{2+} and octahedral Mn^{3+} coordination, and cation-oxygen bond lengths

quantifies the effect of Jahn-Teller distortion on stretched Mn^{3+} octahedra. X-ray Diffraction reveals the tetragonal crystal structure of the material and increased c-lattice parameter due to the Jahn-Teller effect. $Mn_xCo_{3-x}O_4$ samples from x = 0 to x = 1.28 were grown and studied, and manganese cations were found to be octahedrally coordinated. Most samples also show mixed Mn^{3+} and Mn^{4+} character, and greater c-lattice parameter and phase segregation tendencies with increasing manganese content away from Co_3O_4. The increased lattice parameters are likely due to Jahn-Teller-active Mn^{3+} octahedra, and phase segregation may occur due to structural incompatibility between cubic and tetragonal crystal structures associated with Mn^{4+} and Mn^{3+} octahedra, respectively. Mn^{3+} valence character is likely due to insufficient oxygen reactivity during sample growth, with Mn^{4+} being the proper valence state of the spinels. Cobalt valence also trends from mixed Co^{2+} and Co^{3+} towards predominately Co^{2+} with increasing manganese content, meaning Co^{2+} is the favored valence state. This study suggests that the single-crystalline phase of ideal $MnCo_2O_4$ is an inverse-type spinel comprised of Mn^{4+} and Co^{2+} valence states as opposed to the typical 2+ and 3+ states of most other spinels.

Acknowledgments

The journey of acquiring a doctoral degree, while prestigious in the eyes of many, is a tremendous undertaking. The personal advantages and disadvantages of beginning the pursuit must be thoroughly weighed beforehand, and extensive research including deliberation with others and self-introspection beyond what most would consider as sufficient is required. As far as my experience as a doctoral candidate goes, I am blessed to have been granted immense and essential help both through professional collaboration and encouragement from others.

In no particular order I gratefully acknowledge the assistance and services of the following individuals and groups: the highly respectable researchers of Pacific Northwest National Laboratory who have collected data, performed analyses, and given instruction and advice throughout the course of my research. These people include Dr. Tiffany Kaspar (XRD, Ellipsometry), Dr. Mark Bowden (XRD), Dr. Steven Spurgeon (STEM and EDS) and Bethany Matthews (STEM sample preparation). Dr. Steve Heald of Argonne National Laboratory for collecting and analyzing XAS data on multiple samples. Tami Isaacs-Smith for performing RBS, dicing large samples and instructing me on using various tools. Dr. Jonathan Heath and Dr. Marcelo Kuroda for creating multiple DFT models of $CoMn_2O_4$. Dr. Alexandria Bredar, Andricus Burton and Dr. Byron Farnum for their collaboration involved in performing catalysis experiments on $MnFe_2O_4$, and for helping me understand the field of catalysis as a whole. All the faculty, staff and fellow graduate students of Auburn University who have instructed me on the use of tools, experiments, software, data analyses and scientific knowledge throughout my PhD experience. The individuals who have helped me in this way include but are not limited to Dr. Ayayi Ahyi, Laith Alahmed, Dr. Michael Bozack, William Bowers, Dr. Shalinee Chikara, Max Cichon, Patrick Gemperline, Rajendra Paudel, Dr. Sydney Provence, Benajmin Schoene and Suresh Thapa. I'd

also like to acknowledge funding from Alabama EPSCoR Graduate Research Scholars Program through support from the National Science Foundation (NSF-DMR-1809847).

I'm thankful towards the Auburn University's Physics Department in funding me as a teaching assistant for multiple semesters, and for David Patrick for allowing me to teach predominately PHYS 1000 laboratory sessions which I became fond of. I'd like to thank the past and current Physics Department chairmen Dr. Allen Landers and Dr. James Hanson for guiding me and being accommodating and providing solutions for particular coursework challenges I faced. I'd also like to thank all the professors who have helped me learn material and provide advice throughout my coursework and in particular Dr. Jianjun Dong for encouraging me to reach out to my current advisor which had a drastically positive effect on my career trajectory. I'd like to give special thanks to Dr. Jonathan Heath and Dr. Ahmed Nemer who were invaluable study partners during the first few years of my coursework and were essential in allowing me to successfully pass the graduate doctoral exams. I'd like to thank my PhD defense committee who include Dr. Ryan Comes, Dr. Byron Farnum, Dr. Marcelo Kuroda, Dr. David Maurer and Dr. Minseo Park, for their guidance and commitment. Perhaps most importantly, I would like to thank Dr. Ryan Comes who has provided funding as a research assistant and who as an advisor has been consistently helpful, patient, encouraging and positive since we had met. Finally, I would like to thank all my friends and family both within and far from the state of Alabama for their encouragement and for providing respite from the constant tribulations of my academic pursuit.

Table of Contents

List of Tables

List of Figures

List of Abbreviations

AFM	atomic force microscopy
CMO	$CoMn_2O_4$ spinel
EDS	energy-dispersive X-ray spectroscopy
EXAFS	extended X-ray absorption fine structure
FCC	face-centered cubic
JT	Jahn-Teller
MBE	molecular beam epitaxy
MAO	$MgAl_2O_4$ spinel
MCO	$MnCo_2O_4$ spinel
MFO	$MnFe_2O_4$ spinel
Nb:STO	niobium-doped $SrTiO_3$ perovskite
OOP XRD	out-of-plane X-ray diffraction
ORR	oxygen reduction reactivity
RHEED	reflection high-energy electron diffraction
RBS	Rutherford backscattering
RMS	root mean square
RSM	reciprocal space mapping
STEM	scanning transmission electron microscopy
XANES	X-ray absorption near-edge structure
XAS	X-ray absorption spectroscopy
XPS	X-ray photoelectron spectroscopy
XRR	X-ray reflectivity

Chapter 1

Introduction

1.1 Motivation

The development of materials for alternative clean energy sources is central to much of condensed matter research today. Catalytic reactivity for the oxygen reduction reaction (ORR) and oxygen evolution reaction (OER) is an important property for technologies such as electrolyzers, metal-air batteries and fuel cells [1–7]. To date, expensive metals such as platinum dominate this field of research, having shown great promise in both ORR and OER [1,3,8,9]. However, economic considerations demand cheaper materials that offer comparable performance to platinum. Oxygen catalysis systems comprised of inexpensive materials such as transition metal oxides stand as alternatives to platinum. Spinel oxides containing earth-abundant elements such as cobalt, iron, manganese and nickel are particularly promising in this regard [1,10–12]. The spinel material $MnFe_2O_4$ (MFO) along with the Co-Mn spinel system with end members $CoMn_2O_4$ (CMO) and $MnCo_2O_4$ (MCO) exhibit ORR properties on par with platinum [1,11,13–16], making them promising for efficient and affordable catalysis devices as well as energy storage [17–20]. While the ORR properties of these spinels are impressive, a thorough understanding of their physical properties is required for their eventual use in the field of catalysis. This research seeks to characterize the spinels from a thin film perspective and thereby expand the body of knowledge surrounding these materials.

1.2 Oxygen Reduction Reactivity

ORR describes the propensity of a material to act as a catalyst in encouraging oxygen reduction reactions to occur. This set of chemical reactions involves the consumption of free electrons with oxygen gas to produce byproducts such as water or hydroxide (Table 1.1) [21].

During the course of the reactions, the zero oxidation state oxygen atoms of the O_2 decrease to a 2- state thereby reducing the oxygen. The solution acidity the reaction takes place in determines which set of oxygen reduction reactions will occur, with oxygen reacting with protons in acidic solutions and with water in basic solutions. For each environment, reactions can take either 4-electron or 2-electron pathways, with 4-electron pathways having lower redox potentials. In either case, the reaction leads to the acceptance of free electrons so that if a material with ORR properties acts as a cathode in an electrolysis device, a current can be generated. An example of a current generating electrolysis device utilizing an ORR material is seen in Figure 1.1. The ORR material acts as a cathodic electron acceptor during oxygen reduction reactions, while an electron donor material such as one exhibiting hydrogen oxidation reactivity (HOR) provides electrons as an anode [22]. In the case of an acidic medium, hydrogen oxidizes at the cathode to provide protons and electrons that are then transferred to the anode to be used in oxygen reduction. The current passing from anode to cathode can be used to charge a battery of transfer energy.

Table 1.1 Possible oxygen reduction reaction pathways based on solution media. The 2-electron pathway in alkaline solution is only accessible in mediums with pH of 11.6 and above, since HO_2^- will protonate below this [23].

Acidic aqueous solution	4-electron pathway	$O_2 + 4H^+ + 4e^- \rightarrow 2H_2O$
	2-electron pathway	$O_2 + 2H^+ + 2e^- \rightarrow H_2O_2$
		$H_2O_2 + 2H^+ + 2e^- \rightarrow 2H_2O$
Alkaline aqueous solution	4-electron pathway	$O_2 + 2H_2O + 4e^- \rightarrow 4OH^-$
	2-electron pathway	$O_2 + H_2O + 2e^- \rightarrow HO_2^- + OH^-$
		$HO_2^- + H_2O + 2e^- \rightarrow 3OH^-$

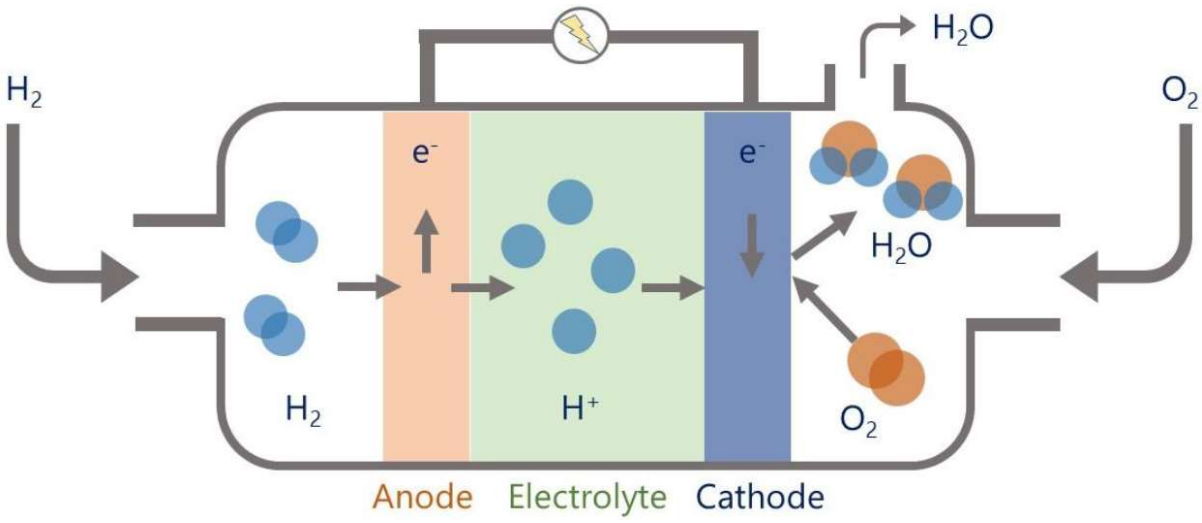

Figure 1.1 Example device schematic for utilizing oxygen and hydrogen to generate current with the assistance of ORR and HOR catalysts.

The Mn-based spinels MFO, CMO and MCO display high ORR properties primarily through their cations. The way they assist the ORR process is similar to the way platinum is understood to contribute to oxygen reduction. In the case of the inner-sphere electron transfer mechanism in alkaline media, platinum encourages the 4-electron pathway of creating hydroxide ions and bypassing the intermediary steps of the 2-electron pathway [24,25]. O_2 adsorbs to a free cation site and reacts with water to acquire a proton to form adsorbed HO_2^-, then reacts with water again to produce OH^- ions. The use of a catalyzing cation in this way reduces the energy and electric potential required to incite the ORR reaction [26]. The cations of spinels are able to contribute to oxygen reduction reactions partially for their oxidation state promiscuity [27]. Manganese in particular is easily able to take on 2+, 3+ and 4+ valence states, all of which are represented in the materials of this study. This promiscuity along with the affordable cost of most first-row transition metals is why MFO, CMO and MCO spinels are of such great interest to the catalysis community.

1.3 Basics of Materials

1.3.1 Spinel Structure

Normal-type spinels are solid-state metal oxide materials described by the formula AB_2O_4 where cation A generally possesses a 2+ formal charge in a tetrahedral site and cation B possesses a 3+ formal charge in an octahedral site. While most spinels such as MFO and MCO are understood to possess a face-centered cubic (FCC) Bravais lattice structure (space group $Fd\bar{3}m$) ([28–31], the Jahn-Teller (JT) interaction can induce a body-centered tetragonal lattice (space group $I4_1/amd$) in others such as in CMO [1,18–20,32–35]. This produces a 45° in-plane rotation of the a and b axes from the conventional cubic lattice and occurs because crystal-field splitting breaks the ordinarily cubic symmetry [4,34–37]. Specifically, the JT-active Mn^{3+} ions in CMO break the degeneracy of partially-filled electronic d-orbital states [38,39]. This leads to elongation of the c-axis parameter through octahedral distortion. The cubic spinel unit cells can be seen in Figure 1.2. Conventional in-plane lattice parameters for spinels with 1st row transition metals range between 8 to 9 Å [40], but JT distortion can cause out-of-plane parameters to lie past 9 Å [41]. conventional unit cell is usually There are 24 cation sites in each conventional unit cell, 8 of them being tetrahedrally coordinated and 16 octahedrally. The face-centered cubic configuration of atoms is considered close-packed and it's common practice to discuss the spinel unit cell as a collection of tetrahedral and octahedral polyhedra. There are a total of 56 individual atoms in a spinel unit cell.

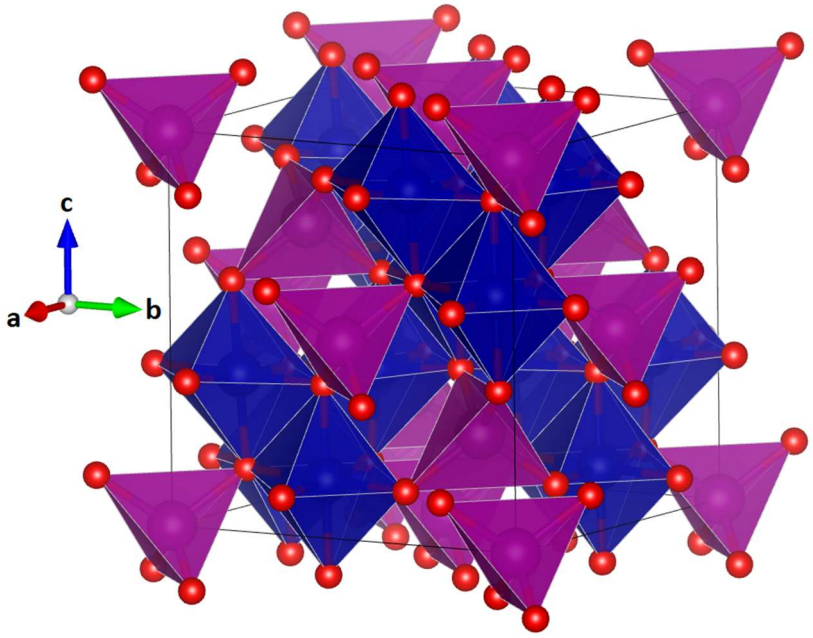

Figure 1.2 Conventional unit cell for a cubic structure AB_2O_4 spinel, with purple and blue polyhedral representing A and B cations, respectively.

1.3.2 Spinel Type

In contrast to the normal spinel structure with all A cations tetrahedral and B cations octahedral, the inverse spinel structure has all the A cations and half of the B cations octahedrally coordinated, leaving all tetrahedral sites to be occupied by B cations. The cations of a spinel have preferred coordinations in which the material's overall energy is lowest which causes a spinel to trend towards either normal or inverse. The structure type a spinel material adopts depends on cation formal charges and crystal field splitting effects [14,42,43]. Excessive growth temperatures and other non-ideal growth conditions can incite spinels to adopt intermediate structures between normal and inverse by increasing the probability of cation coordination defects. This comes in the way of excess lattice energy added to the system [44]. The general formula $(A_{1-\lambda}B_{\lambda})^{Th}[A_{\lambda/2}B_{2-\lambda}]_2^{Oh}O_4$ is able to describe all possible cases, with cations in parentheses

representing tetrahedral occupation and cations in brackets representing octahedral occupation. In the case of an ideal normal-type or inverse-type structure, the degree of inversion (λ) takes on values of 0 or 1, respectively. MFO and CMO of an ideal 1:2 cation ratio exhibit a normal spinel structure [29,32,33,45–47], as do the binary spinels Co_3O_4 [42,46] and Mn_3O_4 [42,46]. MCO has been reported to trend towards an inverse spinel [48–51] in which all the Mn and half the Co are octahedrally coordinated, while the remaining Co are tetrahedrally coordinated.

1.3.3 Cation Valences

As most spinels of the form AB_2O_4 show cation valences of A^{2+} and B^{3+}, MFO would be expected to possess Mn^{2+} and Fe^{3+} valences while CMO would show Co^{2+} and Mn^{3+}. Indeed, previous studies on single-crystalline samples of the two materials have confirmed these states [41,52]. Interestingly, findings on the cation valences of MCO are mixed, with some studies reporting Mn^{4+} character [51,53–55] and others only Mn^{3+} [49]. It is possible that rather than the typical 2+ and 3+ valences, MCO may possess Mn^{4+} and Co^{2+}. In addition to mixed results in literature, this idea is supported by the instability of tetrahedrally coordinated Co^{3+} being unlikely in this inverse-type spinel. Tetrahedral Co^{3+} is rarely observed in nature due to the unfavorable configuration of unpaired e_g orbitals associated with tetrahedral coordination [56]. Spinels that exhibit 4+ and 2+ character are rare but do exist, and are known as “4-2 spinels” in literature [57]. All oxygen anions take on valences of O^{2-} as in any metal oxide material, although oxygen interstitials or vacancies can cause cations to adjust their valences to uphold charge balancing.

1.3.4 Structure formation, variation and phase segregation

A variety of non-stoichiometric properties can contribute to structural changes in these spinels. Cation valence states affect ionic radii and bond lengths of polyhedral which in turn impacts the overall unit cell and lattice parameters [58]. JT distortion of cation polyhedral can also

have significant effects on structure such as in the case of CMO where Mn^{3+} octahedra drives significant increases in the c-lattice parameter [41]. Cation coordination environment with nearest-neighbor oxygen also affects ionic radius meaning variation in spinel inversion parameter leads to structural changes. Point defects such as cation interstitials or oxygen vacancies can also affect structure properties [41]. While a single-phase and homogenous configuration is well understood to exist for MFO and CMO, this may not be true for MCO. Some groups have reported phase segregation in MCO samples rather than single-crystallinity [12,59], and reports of mixed manganese valence character also shows nonuniformity in the material [51,53–55]. Multiple groups have reported the growth of single-crystalline MCO, but confirmation of true single-crystallinity of any material is often elusive in materials physics. It is possible that true single-crystalline MCO spinel is unstable in nature or at least relatively difficult to synthesize. It is also possible that synthesis condition variation across different research studies may account for effects such as phase segregation. The phase segregation behavior of MCO and its viability as a single-crystal will be discussed in a later chapter.

1.3.5 Stoichiometry and other parameter variation:

While spinels with ideal 1:2 cation ratios, valence states and cation coordinations are important to understand, off-stoichiometry spinels are of great interest to scientists as well. Catalytic properties can change greatly with the adjustment of cation stoichiometry [4], and properties such as cation valence and coordination also effect ORR performance [60–62]. Also, sample properties are often linked together such that variation in one property is directly related to changes in others. For instance, decreases in the overall valence state of manganese octahedra from Mn^{4+} towards Mn^{3+} leads to an increased number of JT-active polyhedra and generally a larger c-lattice parameter in the material. Increasing manganese concentration might lead to an increased

or decreased lattice parameter depending on the coordination environment of the additional manganese. Given the impressive ORR properties of CMO and MCO, a primary goal of this study has been to create a map of material properties as a function of cation stoichiometry for the entire cobalt-manganese spinel system from Co_3O_4 through Mn_3O_4. Identifying trends between material properties and stoichiometry allows for a better understanding of the materials overall, and are important for their use in future catalysis technology.

Chapter 2

Thin Film Growth and Characterization Methods

2.1 Advantages of Thin Films

Numerous studies involving MFO, CMO and MCO nanoparticles and nanocrystals already exist in literature [1,4,12,15,17–20,28,32,47,63,64]. A primary advantage of nanocrystalline materials characterization studies lies in the relative ease and accessibility of sample synthesis, especially considering the cost and complexity of most modern thin film deposition systems. However, nanocrystalline samples generally suffer from non-uniformity in sample dimensions, mixed crystal orientations, interface effects at grain boundaries and multi-phase behavior even within a single nanoparticle. Some materials characterization techniques are not possible with nanocrystal structures, and the high-entropy processes of most synthesis methods lead to defect-rich samples that adversely affect analysis results.

Thin film synthesis techniques generally yield samples that have greater dimension uniformity and lower surface roughness, and epitaxial film synthesis in particular can significantly decrease crystal orientation variation. Epitaxial thin film synthesis techniques are much more capable of forming materials in their single-phase or single-crystalline state. Samples created in this way are ideal for materials characterization research because it opens up research to experiments and analyses that rely on structure uniformity. Polarization dependent experiments such as out-of-plane X-ray diffraction and linear-polarization X-ray absorption spectroscopy require single crystal orientations across an entire sample. Relatively smooth samples with equal thickness throughout allows for the observation and interpretation of differences between surface- and bulk-sensitive experiments. Importantly for the purposes of catalysis experiments,

standardized, pore-free surface areas remove a significant variable when investigating these materials ORR properties.

Molecular beam epitaxy (MBE) is perhaps the champion of epitaxial thin film synthesis methods and has been used to create high-quality samples of a wide range of materials [41,65–68]. It is a slow synthesis process that grows thin films at rates in Ångstroms per minute, and offers precision control of growth parameters such as deposition rates and oxygen reactivity. The incredibly slow and controlled pace of thin film synthesis gives ample time for atoms to structure themselves to minimum energy, low entropy configurations. This results in samples with uniform structures and very few defects. This means that materials characterization results from experiments performed on these materials represent the ideal single-crystalline form of that material very closely. At the time of writing, there seems to be only one other study in which MFO thin films were grown using MBE [52], but crystal orientation and substrate differs significantly. Studies involving the growth of CMO or MCO using MBE do not seem to exist, and other general thin film studies are very sparce [49,69,70]. All samples within this study are grown using MBE, and the work represents a significant contribution to field of thin film growth, spinel material properties and future catalysis technology.

2.2 Molecular Beam Epitaxy

2.2.1 System and Functionality

Figure 2.1 shows the schematic for the MBE system used in this study. Base pressures of the chamber are kept to ultra-high vacuum within the range of 10^{-9} to 10^{-8} Torr, ensuring a contamination-free environment during growth. Such low pressures are attained through the use of turbo and cryo pumps, and a differential pump is used to target key systems in the chamber for increased pumping speed. Crucibles containing pure elemental metals and are heated to high

temperatures creating metal vapor fluxes that are directed onto a single substrate lying face-down on the stage. Higher temperatures increase the metal flux through the crucibles, and deposition rates onto the substrate are calibrated pre-growth using a quartz-crystal microbalance. Low chamber pressures ensure that no diffusion of metal vapor occurs and travels in a line-of-sight beam towards the substrate. Molecular beam deposition can be stopped using shutters at the effusion cell openings or below the stage. Oxygen gas is supplied to the growth chamber through a control valve that precisely sets the flow rate. Increasing flow rate increases the overall pressure in the chamber and therefore oxygen reactivity for the growth process. Oxygen pressures typically range between 10^{-6} and 10^{-5} Torr, and is not enough to impede metal deposition beams. Oxygen reactivity can be significantly increased by using a radio-frequency plasma source that separates O_2 into O^- ions. To provide enough energy for proper crystal formation of the film, the stage is heated to particular temperatures. Oxygen reactivity and stage temperature conditions must be set correctly to values within a narrow range window or the spinel structure will not form. The conditions must also be set and stable before deposition begins since a film growth that begins with an incorrect crystal structure is encouraged to continue forming that incorrect structure. After film growth is complete, shutters are closed to stop deposition and the stage is slowly cooled down to room temperature.

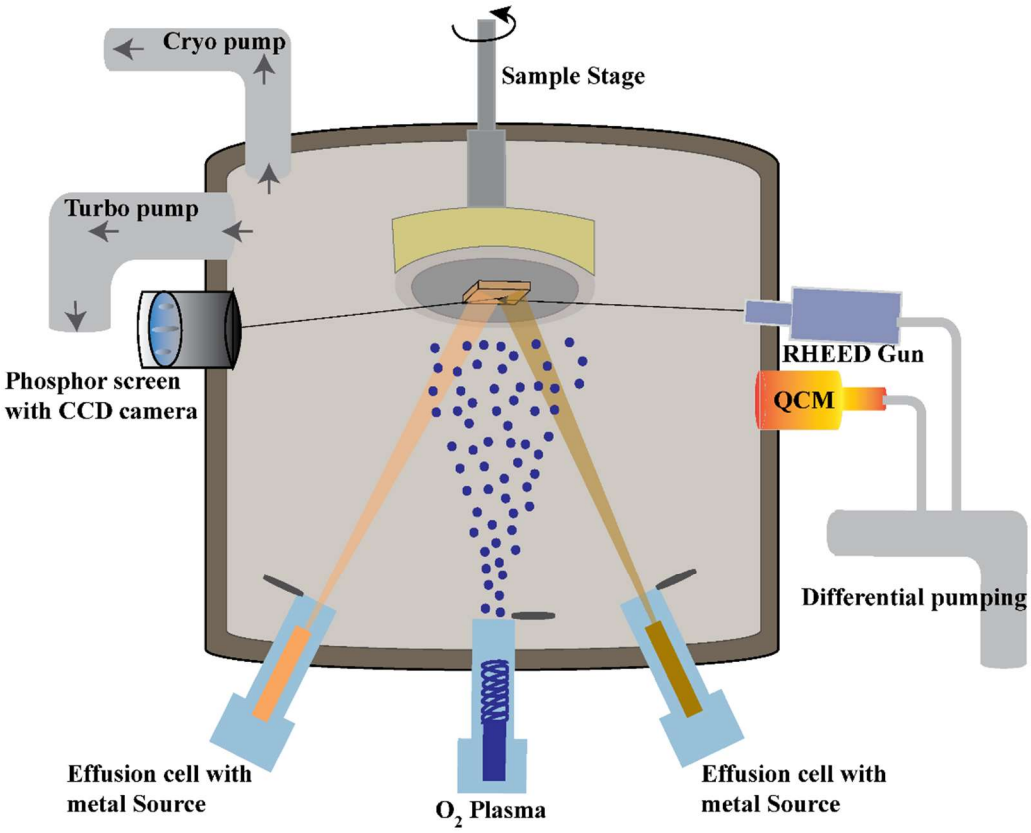

Figure 2.1 MBE system schematic used in sample growth.

Spinel materials that are ideally normal- or inverse-type can take on character of the opposing type through excess energy put in during sample synthesis. Lattice energy increases as partial inversion character trends away from ideal and cations configure themselves in unfavorable coordinations [44]. However, MBE deposits single atomic layers at a time at incredibly slow growth rates, and deposited cations are likely to arrange themselves in minimum-energy coordination environments. Therefore it is likely that the samples of this study, particularly those of single-crystalline or single-phase quality, trend far towards the spinel type that is ideal for the

respective material. This is especially true for all MFO and CMO samples, as characterization experiments show that these samples have excellent crystal structure quality.

2.2.2 Layer by Layer Growth

The most commonly desired growth mode of MBE is layer-by-layer growth in which films are formed one atomic layer at a time across the entire area of a substrate [71]. Films grown in this way have very smooth surfaces with subnanometer root mean square (RMS) roughness. Films grown in this way are of uniform dimension, structure and crystal orientation, and are ideal for materials characterization experiments that benefit from surface uniformity. While it is the most common in studies involving MBE samples, this growth mode can only be achieved in situations where the desired film's structure matches that of the substrate's. Specifically, the in-plane lattice constants of the film must close enough to the substrate's such that the bottom layer atoms of the film can bond directly with the top layer atoms of the substrate without mismatch defects (Figure 2.2(a)). This growth mode creates a smooth transition at the film-substrate interface and is easily achieved when the film and substrate are of the same crystal structure and orientation.

Since the substrate will be orders of magnitude thicker than the film, the in-plane lattice parameter of the film will match that of the substrate and induce in-plane lattice strain throughout the film from interface to surface [72]. This will affect both in-plane and out-of-plane lattice parameters of the film and often alters the material properties of the sample. The effects of strain must be addressed when reporting findings on heavily-strained samples, as relaxed-structure samples may exhibit significantly different properties. At a certain film thickness, the film will relax to allow for a more favorable structure and form dislocations at the substrate-film interface. Relaxation occurs when the increased lattice energy associated with film strain becomes sufficiently greater than the energy associated with dislocations at the interface, which takes place

at greater film thicknesses. The thickness at which films relax increases the closer the substrate and film are in in-plane lattice constant. Therefore, if strained films are desired for a scientific study, proper substrates with similar lattice constants to the film should be chosen. While the (111) crystal plane represents the minimum energy surface of a spinel [73], spinel films will be incentivized to grow along the (001) plane if the substrate's lattice parameters are consistent with the spinel's (001) in-plane lattice parameters. In this study, layer-by-layer growth along (001) was achieved for all CMO and MCO films using cubic structure $MgAl_2O_4$ (MAO) spinel substrates (MTI Corporation) with a lattice parameter of 8.083 Å.

2.2.3 Island Growth

Island growth modes occur when a film's in-plane lattice constant does not match the substrate's. The bottom layer of atoms will gather together at random locations on the substrate surface instead of being evenly spread as in layer-by-layer growth [71]. The gathering points act as a seed to form islands upon the substrate that grow larger in both width and height as deposition continues. The resulting film is far rougher than in layer-by-layer growth and makes characterization experiments that rely on surface uniformity impossible. Despite the non-uniform surface shapes of island growth, ideally-set oxygen reactivity, stage temperature and other growth conditions will still allow for single-orientation films to form as in layer-by-layer growth. As the film deposits further, the islands become larger. The interface between islands will generally show defects preventing single-crystalline island films, but the islands themselves are able to take on single-crystalline quality. Films of this growth mode are also higher in surface area which increases the overall ORR properties of the sample [24]. Misfit dislocations at the substrate-film interface automatically form and the resulting islands and film structure take on a relaxed state in the rest of the film (Figure 2.2(b)). As desirable as layer-by-layer growth often is, island growth modes can

be an unavoidable circumstance when no suitable substrates exist for a particular study. For instance, an MFO film sample may require a conductive substrate in order to be used for ORR catalysis experiments after synthesis [74]. While spinel substrates that are both conductive and suitable for a layer-by-layer growth of MFO are not readily available, niobium-doped $SrTiO_3$ perovskite (Nb:STO) conductive substrates can be used instead, albeit leading to an island growth mode.

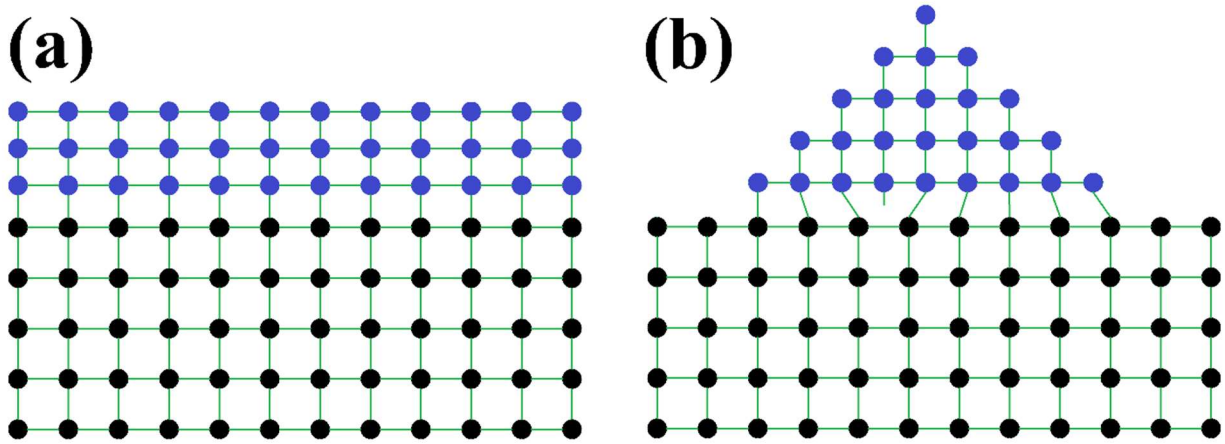

Figure 2.2 Bonding structure and film-substrate interface for a typical a) layer-by-layer growth mode and b) island growth mode.

2.3 Material Characterization

2.3.1 Reflection High-energy Electron Diffraction

Reflection high-energy electron diffraction (RHEED) is an invaluable characterization tool that allows for determination of a sample's structure. The RHEED system is located inside the growth chamber and is used *in-operando* throughout a film growth process. RHEED works by directing high-energy electrons towards the sample surface at a glancing angle, causing some electrons to scatter off atoms on the sample's surface and illuminate a phosphor screen to create a

diffraction pattern [75]. The diffraction pattern is formed according to the periodic position of atoms on the sample and is used qualitatively to determine film structure and can be used quantitatively to determine in-plane lattice constants. An example RHEED pattern formed from the surface of an MAO substrate is shown in Figure 2.3(a). Positions on the diffraction pattern are reciprocal-space representations of physical distances between unit cells of the sample surface. Intensity peaks can be thought of as being made along vertical lines or at horizontal dimension positions on the diffraction pattern, and distances between these vertical lines represent physical distances in-plane between atoms. Larger spacing between vertical diffraction lines indicates smaller distances between crystal planes. Pristine surfaces such as those of finely-polished MAO substrates will create single intensity spots along vertical diffraction lines, while point defects on surfaces will show intensity streaks along these positions such as those shown in Figure 2.3(b) for a CMO film [76].

RHEED images can be collected in real time to allow for video monitoring of the sample during the growth process from substrate surface to final film surface and sample cooling. Also, RHEED is a highly surface-sensitive technique and diffraction patterns are produced from electron scattering from the top one or two atomic layers of the sample. A consistent RHEED pattern throughout the film growth process indicates a uniform structure from bulk to surface and is the first indication of a single-crystalline or single-phase film. This also provides a way for confirming successful layer-by-layer growth modes in films. As seen in comparing both patterns in Figure 2.3, identical vertical diffraction line positions between substrate and film indicate epitaxial strain during growth and constant in-plane lattice parameters. Since island-growth modes lead to films that automatically form in a relaxed state, spacing between diffraction line positions of the substrate will be different from those of the film. Also, the added third dimensional nature of island

growth structures creates additional opportunities for electron interference and multiple intensity spots form along the vertical diffraction lines [76]. This type of RHEED pattern is seen with MFO films grown on Nb:STO substrates due to the island growth mode.

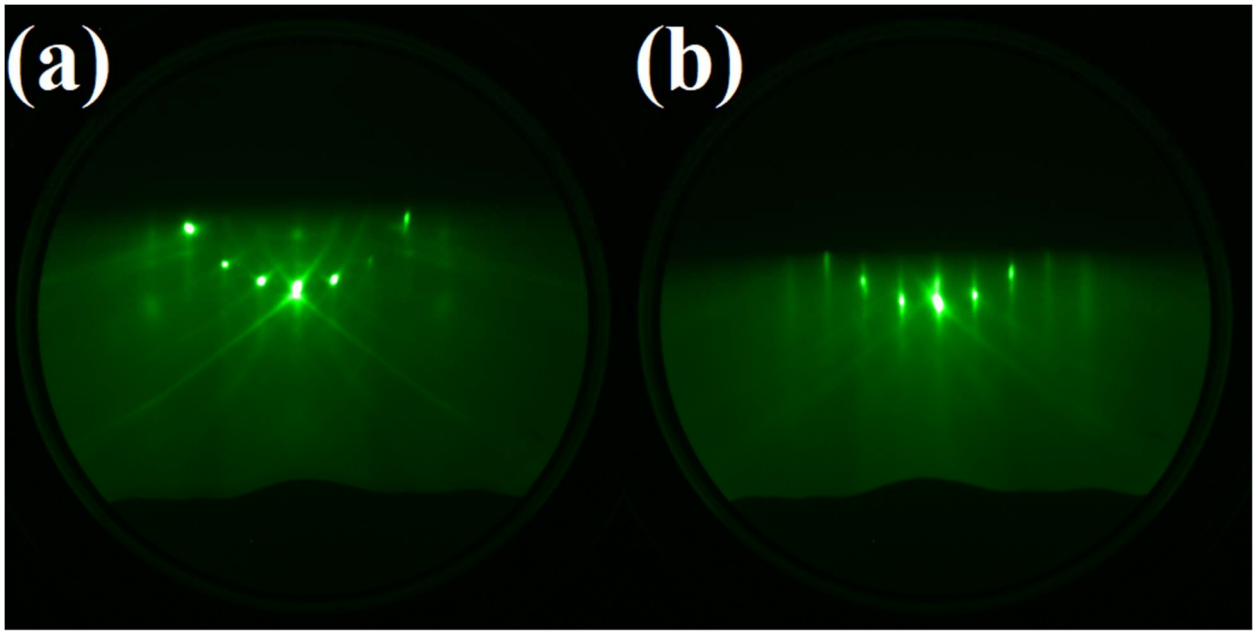

Figure 2.3 RHEED patterns of an a) MAO substrate and b) CMO film. Intensity spots of the substrate line up at identical positions to vertical intensity streaks of the film, indicating in-plane epitaxial strain.

The oxygen reactivity and stage temperature conditions that are ideal for a material's formation may not be suitable for maintaining its structure once deposition stops. In some cases, phase reconstruction may begin after shutters are closed if conditions are not suitably adjusted [77]. This reconstruction generally occurs at the surface and can be seen through changes in RHEED diffraction patterns, although the phase change may extend into the film's bulk beyond the sensitivity of RHEED. In the case of CMO, oxygen pressure used during film growth must

decrease by almost an order of magnitude to prevent phase reconstruction and maintain the spinel structure during sample cooling. This indicates that the material over-oxidizes during cooldown if oxygen reactivity is not reduced. This may happen through the spinel structure's Mn^{3+} octahedra trending towards Mn^{4+}, thereby thwarting JT distortion and forcing a structure change.

The constant bombardment of high-energy electrons in RHEED can have adverse effects on some materials. Some materials such as MFO show no visible indications of being affected by RHEED. However, CMO films that involved constant bombardment of RHEED electrons during the growth process showed visible streaks or blotches along the surfaces of the sample where electrons were incident. It is possible that electrons of RHEED reduced cation valences creating non-spinel structures or phase segregation. The adverse effect of RHEED on materials such as CMO can be greatly diminished by blanking the electron beam whenever possible. While RHEED images are typically generated in real time, a small collection of single RHEED pattern images collected every few minutes is sufficient for confirming a successful film growth.

2.3.2 Atomic Force Microscopy

Atomic force microscopy (AFM) is an invaluable tool in studies involving thin films. A primary function of AFM is to create maps of a sample's surface topography (Figure 2.4) but AFM can also be used to create maps of charge distribution, capacitance and other electrostatic properties [78]. AFM measures topography by using a cantilever that scans over the entire surface of a sample. The cantilever is electrostatically repelled over the surface and variation in height over a surface causes the cantilever to move up or down with the topography [79]. This movement is translated to topography through variation of a laser that reflects off the top side of the cantilever into a detector during scanning. Epitaxially strained samples created through layer-by-layer growth show topography maps with highly smooth surfaces, while maps of samples of island growth

modes clearly show the resulting islands on the surface. A sample's roughness can be quantified by calculating the root mean square (RMS) roughness of the scan window, and all layer-by-layer grown samples of this study possess RMS roughness below 1 nm. AFM can also show phase segregation or surface faceting in samples that experience this during growth.

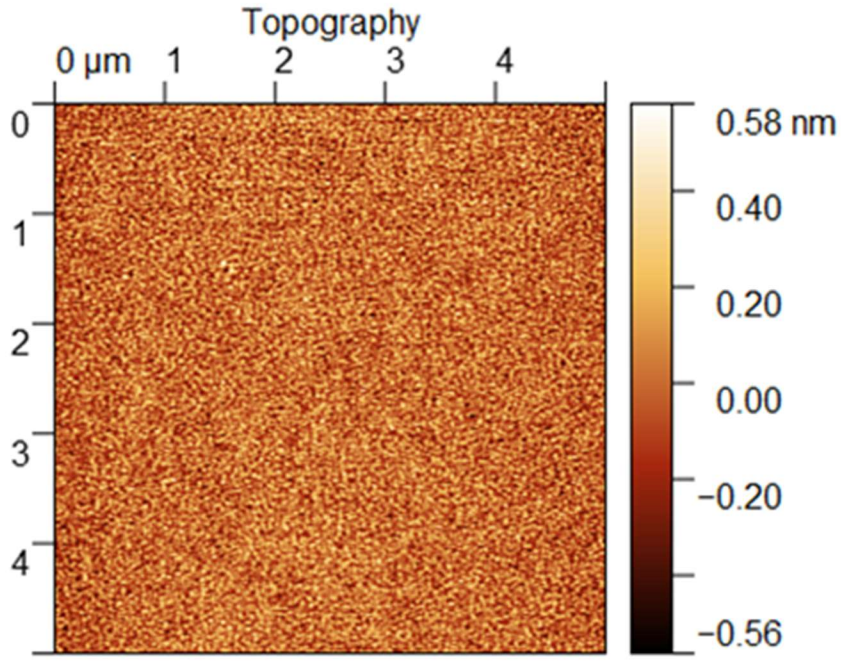

Figure 2.4 Example AFM topography map depicting a CMO sample.

2.3.3 Scanning Transmission Electron Microscopy

Scanning transmission electron microscopy (STEM) performed on materials can show a clear cross-sectional image of thin films in atomic detail [80]. Figure 2.5 shows a STEM image of a CMO film including the substrate, film and platinum capping layer deposited during the STEM sample preparation process. STEM sample preparation involves isolating and lifting out a thin cross-section of a thin film sample, thinning it to ~100 nm or less in width and generating a map of the cross-section using a transmission electron microscope. During imaging, a high potential difference (~300 kV) accelerates electrons towards the sample cross-section's flat surface. The

electrons are incident along the vector normal to this flat surface. Some electrons travel through the sample, deflecting off atoms as they pass through. This causes the electrons to leave the sample at off-normal angles. In dark field imaging in particular, some electrons enter an annular detector that counts the number of electrons passing through at the particular angles associated with the detector's width. The electron beam scans one small section of the sample at a time, and a higher number of electrons being detected indicates that the average atomic number of that section of the sample is higher. STEM images give an easy visualization of sample dimensions including film thicknesses. It supports claims of single-crystallinity that become apparent through the use of RHEED during sample growth. It also can show the film-substrate interface of samples in detail and reveals epitaxial strain in films that were synthesized through layer-by-layer growth modes. STEM will also show phase segregation or other structural variation of a film, and provide a way to measure film thickness and surface roughness of island-growth surfaces.

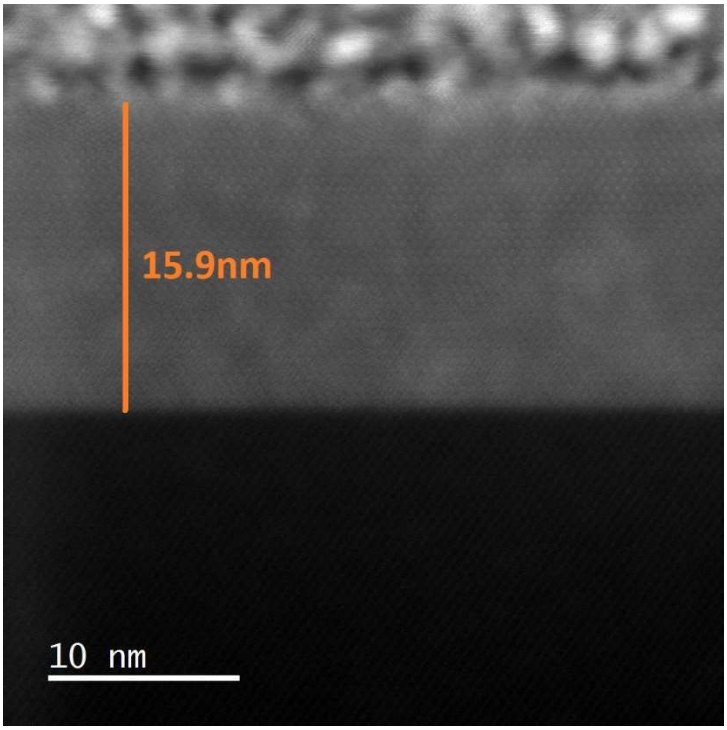

Figure 2.5 Example of a cross-sectional STEM image of a CMO sample depicting an MAO substrate below the CMO film, with amorphous platinum above which is to protect the sample during STEM preparation.

Energy-dispersive X-ray spectroscopy (EDS) is an analysis that is sensitive to the atomic number of atoms and shows elemental concentrations as a function of position in an electron microscopy image [81]. EDS measures the photon energy of fluorescent X-rays being emitted while electrons are incident on a sample. The fluorescent X-ray energy corresponds to the element of the atom generating it, allowing for an elemental map of a sample to be created. EDS is particularly useful in observing multi-phase behavior in materials by illustrating uneven distributions of cations. This has been seen in MCO in the past where EDS showed the material to phase segregate into CMO and Co_3O_4 [12]. All STEM samples in this study were prepared using a standard liftout procedure using an FEI Helios DualBeam 660 SEM-FIB. Initial cutting was

performed using an ion beam voltage of 30 kV but final milling voltage of 2 kV to ensure smooth sample edges. Bright-field STEM images were collected using a JEOL GrandARM-300F microscope at a voltage of 300 kV. EDS maps generated from STEM samples were created using a dual JOEL Centurio detector.

2.3.4 X-ray Diffraction

X-ray diffraction (XRD) provides structural information of a material based on the size and orientations of its unit cells [82]. Samples of high-crystalline quality give peaks at particular X-ray path angles according to Bragg's law, and the existence of these characteristic peaks confirms the cubic or tetragonal crystal structure of the spinel samples. Out-of-plane (OOP) XRD in particular is ideal for analyzing thin films of uniform crystal-orientation such as those of this study and is sensitive to the out-of-plane lattice direction only. Diffraction occurs at particular X-ray path angles according to Bragg's law and their angular position can be used to calculate a film's c-lattice parameter. Peaks associated with the FCC spinel structure's (004) or (222) diffraction condition are most relevant to this study, and appear in OOP XRD spectra depending on the growth orientation of the film. Spinel films grown on (001)-oriented MAO or Nb:STO substrates also grow along the [001] lattice direction, while spinels grown on (111)-oriented Nb:STO also grow along [111].

XRD is a bulk-sensitive experiment and so spectra of thin film samples will display diffraction peaks of both substrate and film. Due to its larger volume, substrate peaks are significantly sharper and higher-intensity than film peaks. Despite their nanometer-range thickness and broader shape, the peaks of high-crystallinity single-phase films show clear angular positions for calculation of c-lattice parameters. OOP XRD spectra of highly-crystalline thin films also display intensity maxima at periodic angular positions on either side of the main diffraction peak

[82]. These thickness fringes appear due to the interference between X-rays that reflect off the substrate-film interface and the film surface itself. Thickness fringes are an indication of high-crystallinity and smooth surfaces because interruptions to periodicity in the lattice or irregularities in the surface prevents the constructive interference of X-rays. The position of these fringes primarily depends on the thickness of the film and provides a method of determining film thickness along with X-ray reflectivity. Thickness fringes are seen in all CMO samples supporting the claim of their single-crystallinity.

In samples that underwent phase segregation during growth, OOP XRD will clearly show this by displaying multiple film peaks in the spectra. This phenomenon is prevalent in some samples in the range near MCO's stoichiometry, and phase segregated spectra can show secondary peak locations that are quite varied in angular position and peak broadness. However, most phase segregated spectra in this stoichiometry range show primary film peaks with relatively narrow broadness suggesting a single phase dominates the film's structure. OOP XRD spectra were gathered using a Rigaku SmartLab diffractometer system with a Cu Kα source, and filtered appropriately for thin film samples using a parabolic mirror and two-bounce Ge(220) monochromator.

2.3.5 Reciprocal Space Mapping

OOP XRD is sensitive only to the out-of-plane lattice direction, but reciprocal space mapping (RSM) can be used to learn information on a material's in-plane direction [83]. In OOP XRD, the X-ray source and detector adjust their relative positions such that the angle between them is directly along the sample's surface normal. This maximizes the signal along the sample's out-of-plane direction but leaves no sensitivity in-plane. In RSM analysis, the source and detector's median angle is adjusted to have both an in-plane and out-of-plane component to give information

on both a material's c-lattice parameter and a- and b-parameters. The result is a map that gives X-ray intensity as a function of both in-plane and out-of-plane lattice constants (Figure 2.6). RSM is important in thin film samples for being able to confirm lattice strain with layer-by-layer growth modes. For instance, Figure 2.6 shows a map depicting a CMO film on an MAO substrate. The y-axis and x-axis indicates out-of-plane and in-plane lattice dimensions, respectively. While CMO has a larger out-of-plane parameter, the in-plane parameter of both CMO and MAO are the same which puts X-ray intensity from both materials along the same vertical line on the map. RSM of MFO samples grown on Nb:STO do not show film strain because island growth modes lead to relaxed epitaxial films, but strain is seen in CMO and MCO films grown on MAO. RSM was performed using the same setup for standard OOP XRD with a rotational stage attachment that allows for additional degrees of freedom so that in-plane diffraction conditions can be accessed.

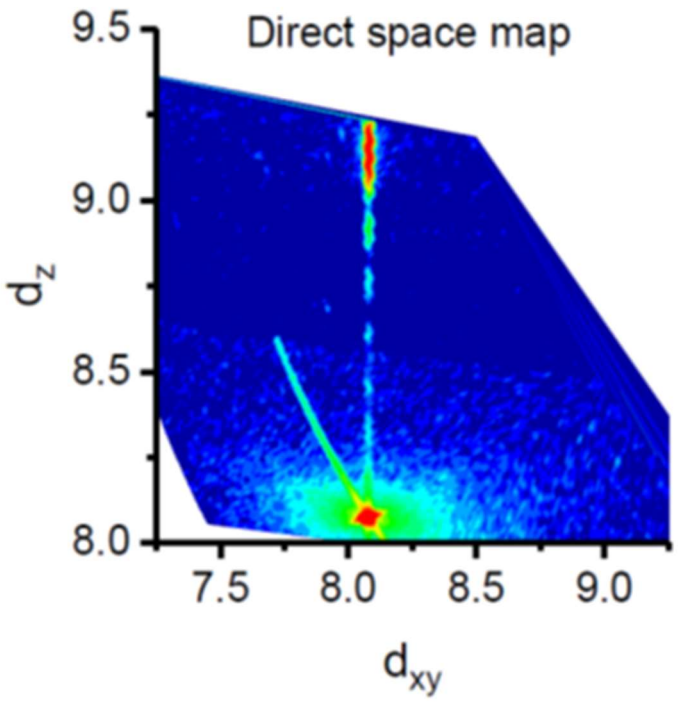

Figure 2.6 RSM map of a CMO film on an MAO substrate showing high intensity X-ray signal (red) aligned along the same vertical position, indicating both substrate and film have the same in-plane lattice parameters.

2.3.6 X-ray Reflectivity

X-ray reflectivity (XRR) is commonly used with thin films to measure sample thicknesses [84]. The principles of XRR are similar to those of thickness fringe generation in OOP XRD. Constructive interference between X-rays that reflect off the substrate-film interface and the film surface itself cause periodic intensity peaks at different angular positions. Thicker films will lead to a higher frequency of peaks, and XRR spectra can be fit to give a sample's film thickness, mass density and surface roughness (Figure 2.7). The X-ray source and detector scan at glancing angles from the sample surface and generally do not have include standard diffraction peaks in the spectra. While film thickness has little impact on a sample's material properties, confirmation of film strain

through RSM along with XRR results gives lower bounds of film thicknesses for which a material remains epitaxially strained to a substrate without relaxing.

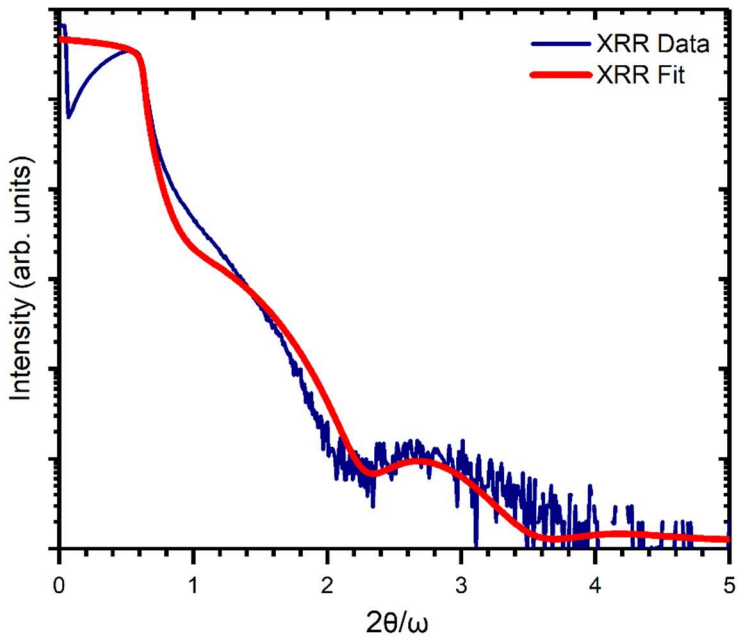

Figure 2.7 XRR fitting example of an MFO film showing periodic intensity.

Film surfaces that are too rough prevent meaningful XRR spectra to be generated as the technique relies on the uniform reflection of X-rays off both the film surface and substrate-film interface. This allows for thickness determination of layer-by-layer growth mode films such as for CMO and MCO on MAO, but not for some island growth films such as for MFO on Nb:STO. While single-phase or single-crystalline samples can be fit using one single layer of a particular thickness, roughness and density, some XRR spectra can be better fit using multiple layers with different parameters indicating a phase segregated structure for the film. This would be seen in samples that undergo surface reconstruction after growth, or some MCO samples that are seen as

multi-phase in their XRD spectra. XRR was performed in tandem with OOP XRD, and used an identical experimental setup.

2.3.7 Rutherford Backscattering

Rutherford Backscattering (RBS) was performed on CMO and MCO samples to calculate their cation stoichiometry. RBS works by bombarding samples with high-energy ions such as helium nuclei and measuring backscattering intensity of ions off atoms in a sample as a function of channel number [85]. Intensity at higher channels represents backscattering off atoms closer to the surface and off atoms of higher atomic number coincidentally. For these films grown on top of MAO, this makes backscattering intensity from cobalt and manganese atoms stand out clearly from magnesium or aluminum signal from the substrate, and from oxygen with its lower atomic number. RBS was performed using a 6HDS-2 tandem, National Electrostatics Corporation Pelletron through helium nuclei bombardment.

RBS data can be fit to determine elemental concentration in a sample (Figure 2.8), and the cobalt-manganese stoichiometry of every sample can be easily determined due to how isolated the these cation peaks are from the rest of a spectrum. Elemental concentration from fitting is primarily dependent on the area ratio between peaks, meaning stoichiometry results are valid regardless of a film's thickness, crystal structure or oxygen content. RBS is also a bulk-sensitive experiment, making stoichiometry determined from fits reflective of an entire film and not just the surface. In this way, RBS stoichiometry is not adversely affected by surface effects such as phase reconstruction as X-ray photoelectron spectroscopy is. While cobalt and manganese peaks are separated in channel number enough to be deconvolved and fit, iron and manganese peaks experience great channel overlap due to their small difference in atomic number by one. This

makes determination of stoichiometry in MFO films through RBS impossible, and other methods such as XPS or EDS must be used to determine MFO cation stoichiometry.

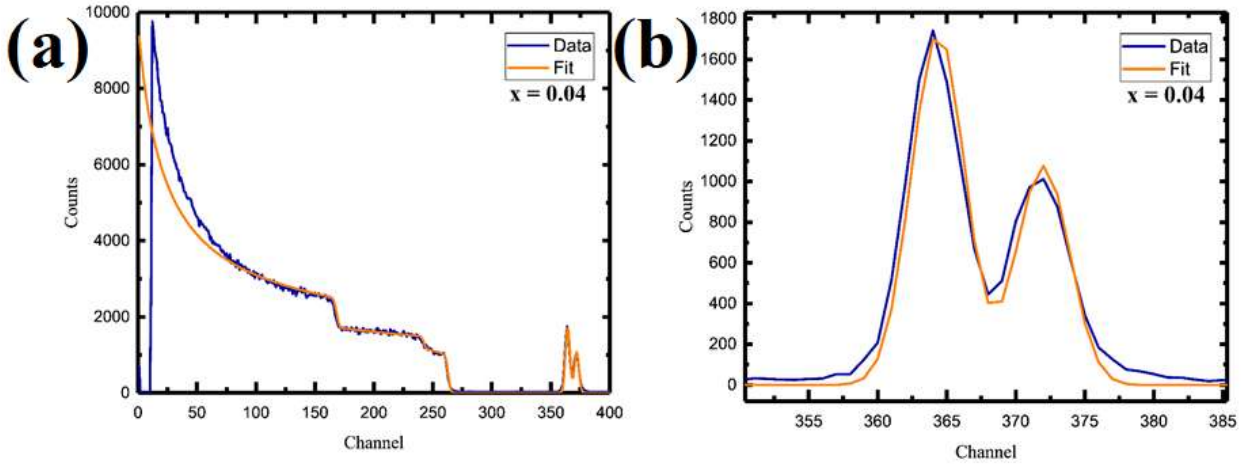

Figure 2.8 RBS fitting example of a CMO-MAO sample showing (a) the entire spectrum including signal from the substrate and (b) a close-up of the cobalt and manganese metal peaks.

2.3.8 X-ray Photoelectron Spectroscopy

X-ray photoelectron spectroscopy (XPS) is a popular surface-sensitive materials characterization technique that gives information on a sample's elemental stoichiometry, valence state and bonding environment. It works through the principles of the photoelectric effect in which X-rays of sufficient energy cause electrons in the material to be ejected out to vacuum level [86]. The electrons are ejected in all directions but some enter through an analyzer that counts the number of electrons passing through at given kinetic energies. Conservation of energy dictates that a photoelectron's kinetic energy is based on the incident X-ray energy, analyzer work function and previous binding energy environment of the electron. From this, the previous binding energy environment can be calculated and XPS spectra show photoelectron count intensity as a function of binding energy in the material.

Electrons excited from the same subshell state such as Co 2p or O 1s will have similar binding energies but effects such as spin-orbit and multiplet splitting will lead to variance in electron binding energies within a single subshell [87]. This leads to spectra regions with complex shapes and features that form according to the number of electrons at particular binding energies within a region. An example spectrum region is seen in Figure 2.9(a) depicting Mn 2p. The region can be analyzed both by inspection and through fitting software to determine properties of the region's element and the material overall. Mn 2p and other transitional metal 2p regions generally form two peaks due to spin-orbit splitting, one representing electrons from the $2p_{1/2}$ state and one for $2p_{3/2}$ state. A multiplex scan in XPS refers to the acquisition of several key spectrum regions of a sample during one experiment. The emphasis of multiplex scanning is slower scanning and higher resolution data for a small number of electron shell regions. For instance, a multiplex of a CMO film may include the regions Co 2p, Mn 2p, Mn 3s and O 1s specifically.

A survey scan refers to the acquisition of a single low-resolution spectrum of the sample through the entire binding energy range of the system. An example XPS survey for an MFO sample is seen in Figure 2.9(b). Typical X-ray sources, such as Al Kα with X-rays of about 1400 eV, will have sufficient energy to excite core and valence electrons from most electron shells of the 1st-row transition elements [88]. This is important for studies of MFO, CMO and MCO where XPS analysis of manganese, cobalt and iron relies heavily on their 2p regions.

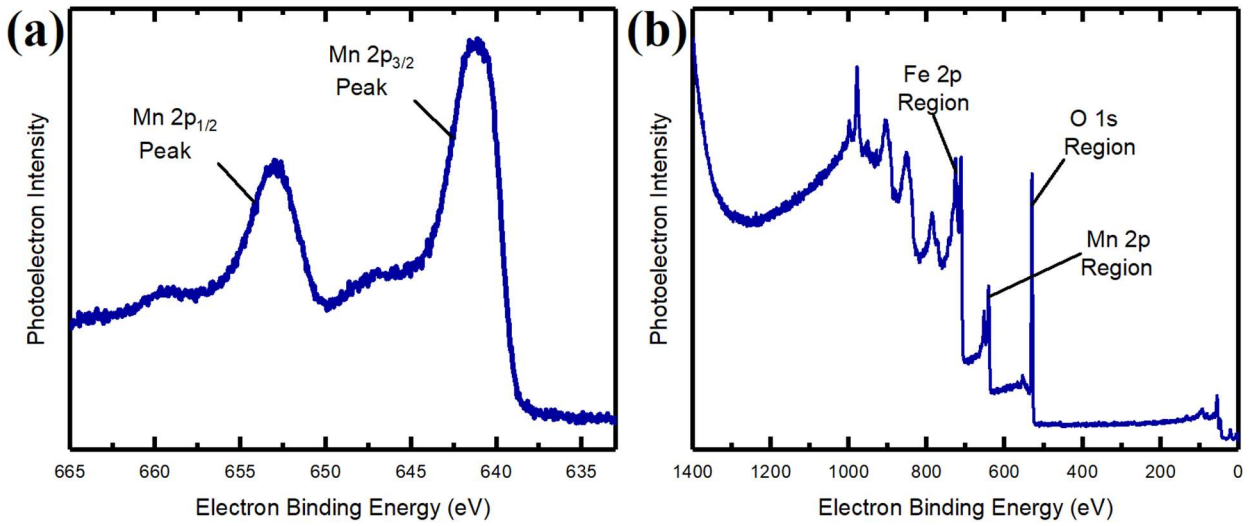

Figure 2.9 XPS spectra of a) Mn 2p region from a multiplex and b) survey from an MFO sample. The location of the satellite in Mn 2p is characteristic of Mn^{2+} specifically.

The high resolution spectra from multiplex scans allows for trustworthy identification of material properties based on spectral features or shapes. For instance, the existence and location of satellite features in a cation element's 2p region is characteristic of the cation's valence state [89]. This was essential in identifying the Co^{2+} and Mn^{3+} valence states in CMO samples [41]. Greater concentrations of an element in a sample leads to increased intensity in a spectrum region meaning that spectra of different regions can be integrated for their area and compared to one another to calculate elemental ratio. Stoichiometry determination in this way relies on the use of normalizing sensitivity factors specific to each electron shell region, or area comparisons have no physical meaning. Unfortunately, using XPS to calculate stoichiometries in a sample is prone to inaccuracy due to variation between spectral shapes between samples and because proper integration bounds of a region are often uncertain. Even so, stoichiometry determination using XPS was attempted for MFO samples due to the unavailability of RBS for this purpose. Survey

scans should routinely be performed on every sample of a thin film study such as this one, particularly to check for possible contamination of unexpected elements on the surface. Surveys provide proof of a sample's general composition and while quantification is not recommended due to their low resolution, stoichiometry estimations can be made based on the relative height of features from different electron shell regions.

XPS is an especially surface-sensitive with penetration depths of no more than 10 nm depending on the incident X-ray energy and beam angle [90]. This surface sensitivity is important in thin film studies of samples whose film and substrate share elemental composition, such as $SrNbO_3$ perovskite on $SrTiO_3$ [91]. Results from this study show that for an Al Kα source with a 45º incidence, the vast majority of XPS intensity signal comes from the top 6 nm of a sample. This is because an XPS of a 6 nm thick MFO film grown on Nb:STO shows a clear but incredibly faint photoelectron signal of strontium and titanium from the substrate.

Use of a monochromator setup is essential for the generation of high resolution XPS data. Without one, incoming X-rays will have a range of energies leading to broadening of spectral features. The emission of electrons leaves holes in the energy levels of atoms and without a way for additional electrons to fill the holes, a sample will accumulate a positive charge over time. This positive charge affects the kinetic energies of negatively charged photoelectrons thereby affecting intensity counts at given binding energies and adversely affecting XPS spectra over time. Samples that are conductive do not suffer from this because electrons from ground will refill holes continually, but this cannot happen in insulating samples. To prevent sample charging over time, an electron gun neutralizer provides electrons to the sample to fill holes created by photoemission. Use of a neutralizer will give a negative charge to a sample, but the charge value is constant in time. The constant negative charge will shift the entire spectrum in energy however every data

point will be shifted by the same value such that spectral feature shapes are retained. Energy shift calibration is performed post-acquisition to place peaks common between spectra of different samples to the same value, such as shifting all spectra such that O 1s peaks are positioned at 530 eV [41].

Once a sample grown using MBE is exposed to atmosphere, the sample will accumulate adsorbed water and carbon species on the surface and greatly affect the bonding environment of atoms and thus adversely affect resulting XPS spectra [92]. Quantification of XPS of contaminated samples in this way becomes invalid, and qualitative characterization by inspection become unreliable. XPS performed on samples *in-situ*, or immediately after growth and before air exposure, will provide data that is a true reflection of the material's surface. All XPS of samples in this study was performed *in-situ* using a PHI 5400 system refurbished by RBD Instruments. The system is connected through vacuum transfer line with the MBE growth chamber, allowing surfaces to be measured before exposure to atmosphere. The system used an Al Kα X-ray source equipped with a monochrometer at 45º incidence. An electron neutralizer was used throughout the XPS measurements and all vacuum sample spectra were appropriately energy shifted so that their single O 1s region peaks were placed at 530 eV.

2.3.9 X-ray Absorption Spectroscopy

X-ray absorption spectroscopy (XAS) is a widely-sought bulk-sensitive experimental technique that provides data that is sensitive to multiple material properties including atomic valence, coordination and bond lengths. XAS spectra are created by incident X-rays causing core shell electrons to be excited into unoccupied states, leaving core shell holes [93]. For the XAS fluorescence data used in this study, higher-shell electrons fill the newly-created gaps which in turn releases detectable fluorescent X-rays. The incoming X-rays are created at synchrotron

facilities to provide a continuous range of X-ray energy to give spectra of fluorescent X-ray intensity as a function of incident X-ray energy. The XAS spectra used in this study refer to the K-edge region that focuses on the range of incoming X-ray energies that excite 1s electrons to unoccupied states, although there is also L-edge XAS that focuses on the excitement of 2p electrons. XAS data is a powerful tool that is highly valuable but difficult to acquire because it requires the reservation of beam time at large synchrotron facilities such as those at national laboratories.

Figure 2.10(a) shows an example XAS spectrum of the cobalt K-edge. Spectra are separated into two regions: X-ray absorption near edge structure (XANES) and extended X-ray absorption fine structure (EXAFS). The primary feature of XANES is the K-edge shelf which is a large spike in intensity that represents the incident X-ray energies becoming sufficient to excite 1s electrons to unoccupied states. Other features of XANES may include pre-edge peaks that form due to structural properties such as the cation's coordination environment [94]. EXAFS contains periodic variations in fluorescent X-ray intensity that come from the interaction of excited 1s electrons with neighboring atoms. Incoming X-rays can also be set to linearly polarizations, allowing for two sets of spectra from orthogonal polarizations that are sensitive to the in-plane and out-of-plane lattice directions separately. Differences between spectra of orthogonal polarizations reflect linear dichroism in the material and electronic structure variation between the two directions. This is the case for CMO in which JT distortion causes distortion of Mn^{3+} octahedra to stretch out-of-plane, leading to structural and electronic differences between lattice directions as seen in XAS [41]. Spectra of both in-plane and out-of-plane polarizations were collected for cobalt and manganese K-edge regions of a number of samples. All XAS Fluorescence data was collected at the Advanced Photon Source of Argonne National Laboratory at Sector-20 BM.

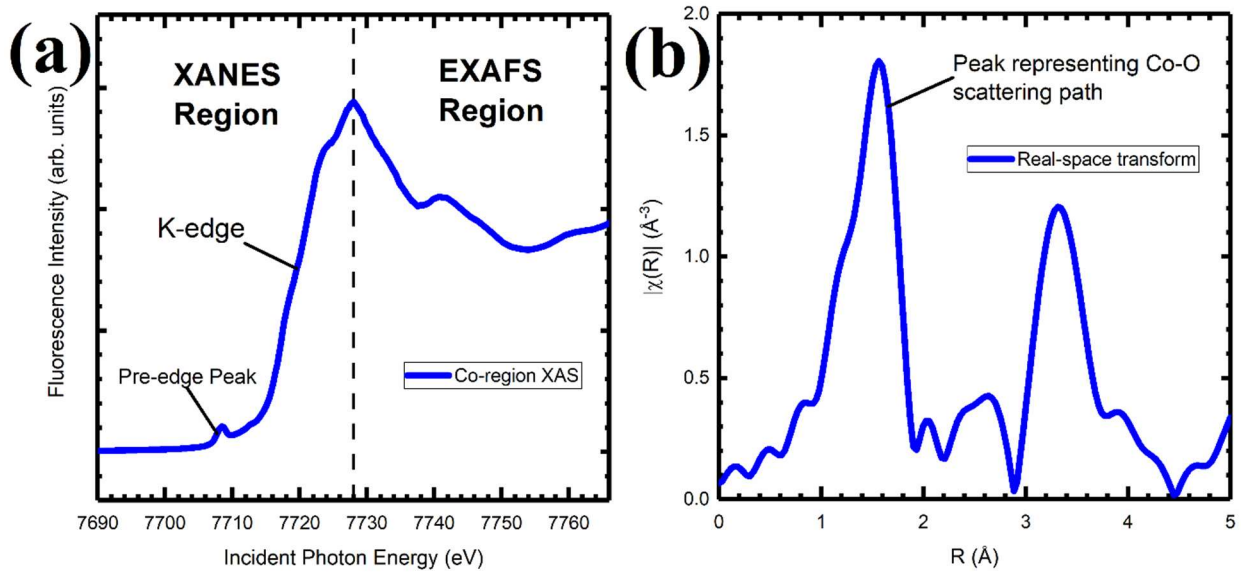

Figure 2.10 a) Example XAS spectrum separating XANES and EXAFS regions and indicating key features. b) Transformed spectrum converting XAS periodicity to real space intensities.

Overall shapes of XAS spectra of multiple samples can be compared with each other to determine trends between samples of differing stoichiometry. For instance, invariability in both cobalt and manganese spectra for both in- and out-of-plane polarizations show how little the electronic properties of CMO change with stoichiometry [41]. In the XANES region, relative shifts of the K-edge shelf towards higher binding energies is an indication of higher cation valences which allows for qualitative determination of valence states [95]. K-edge XAS spectra will sometimes show pre-edge peaks at energies below the characteristic K-edge shelf. These pre-edge peaks can be an indication of multiple material properties but in the case of the cobalt K-edge region, a high-intensity pre-edge peak is an indication of tetrahedral coordination in the case of Co^{2+} cations [96].

Linear combination fitting of XAS spectra attempts to determine the percent composition of a single spectrum between two or more reference spectra of other materials. It seeks to determine the intensity percentage of each reference's spectrum such that the percentages add up to the best possible fit to the sample's spectrum. Such analyses are found in other studies involving cobalt and manganese XAS spectra [97–99] and are best used when the sample material is comprised of perfect versions of the reference materials. The analysis is often used to quantify cation valence state of a sample using reference standards containing known valence states. For example, using linear combination fitting to determine the manganese valence of an unknown sample using CMO with Mn^{3+} and MnO_2 with Mn^{4+} as standards. Accurate valence state determination in this way is prone to error, particularly when samples and standards do not share the same structure. This is because XAS spectra are sensitive to multiple material properties including crystal structure, and spectral features can vary wildly despite having identical cation valence states. However, qualitative trends in electronic valence can be made between samples such as the cobalt valence state of Co_3O_4 generally increasing with the introduction of manganese, as will be shown in a future chapter.

As energy shifts between XAS spectra indicate changing valence states, plots of the intensity's first-order derivative as a function of energy can be analyzed to analyze trends in cation valence between different samples. This analysis has been used in previous studies involving XAS spectra for both cobalt and manganese [100–102]. Varying degrees of slope in XAS spectra lead to the generation of individual peaks in their derivative plots, and these peaks can be assigned to particular valence states of the material. For instance, XAS derivative plots of Co_3O_4 show two distinct peaks corresponding to the Co^{2+} and Co^{3+} valence states of the material. These peaks are sufficiently separated in energy and the ratio between the peak heights is an indication of the ratio

between Co^{2+} and Co^{3+} cations in the material. Using this analysis to determine exact ratios between cations of different valence states is inadvisable due to the complexity of XAS spectra, but qualitative trends between samples can be shown. For instance, Co_3O_4 in this study shows a larger Co^{3+} peak than Co^{2+} which reflects that 2/3 of the spinel's cobalt is in a 3+ valence state. Similarly, CMO which is solely comprised of Co^{2+} shows a larger Co^{2+} peak in XAS derivative plots.

Samples such as Co_3O_4 with both Co^{2+} and Co^{3+} character reveal two distinct peaks in XAS derivative plots, widely separated in energy. However, Mn^{3+} and Mn^{4+} peaks for samples in this study are very close in energy and samples that show both Mn^{3+} and Mn^{4+} character reveal one distinct peak as opposed to two. The lack of two distinct peaks makes evaluation of manganese valence between the two valence states impossible using peak intensity. However, the energy position of the peak relates to the sample's overall manganese valence state, with higher energy positions corresponding to higher valence states. This allows for qualitative trends in manganese valence to be identified between samples which will be shown to be useful in characterizing MCO samples with mixed manganese valence character.

2.3.10 Extended X-ray Absorption Fine Structure Analysis

Incident X-rays in the EXAFS region have sufficient energy to excite core electrons to unoccupied states just as they do at the K-edge, but the region is shaped with periodic intensity due to the interaction of excited electrons with neighboring atoms [94]. Higher incident X-ray energies cause excited electrons to have kinetic energies equal to the extra photon energy from what is required for excitation. These electrons can then be described as a waveform that emits in all directions around the central atom, with wavelength and wavenumber corresponding to the electron's kinetic energy. The electron's waveform reflects off neighboring atoms in the form of

scattering and travels back towards the central atom. When the emitted and reflected electron waveform constructively interferes and is in phase at the central atom location, the absorption coefficient for the electron excitation event increases and thus the probability of a fluorescent X-ray being created increases. When the emitted and reflected electron waveform destructively interferes or is out of phase, the absorption coefficient decreases. The energy of the electron determines the wave number of the outgoing electron waveform, and this leads to alternating constructive-destructive interference at the central atom location with changes in the electron's kinetic energy and thus incident X-ray energy.

The energy periods of the EXAFS region between higher and lower fluorescence intensity depends on the distance between a central atom and the scattering neighbor atom. This means information on atomic bond lengths is embedded in XAS data and can be fit to determine these bond lengths [103]. A Fourier transform is performed on an XAS spectrum to convert the spectrum's periodicity to amplitudes in real space, thereby allowing for extraction of bond length values in terms of physical distances. An example of a transformed XAS spectrum is shown in Figure 2.10(b). Peaks in the transformed spectrum indicate electron scattering events with neighboring atoms, and the peaks are fit to extract bond lengths between the central atom and the scattering neighbor. Peaks found at the lowest radial distance value correspond with the central atom's nearest-neighbor in a crystal lattice. In the case of CMO and MCO, the nearest-neighbors to the cobalt and manganese central atom sites are neighboring oxygen which form either tetrahedral or octahedral polyhedra. Some peaks in transformed spectra often overlap greatly with each other, making their fitting for bond lengths difficult. However, the nearest-neighbor oxygen peaks for these spinels are generally deconvolved from other peaks, making their fitting much more straightforward and bond length determination more reliable.

The nearest-neighbor oxygen bond lengths for the cobalt and manganese cations of CMO and MCO were the focus in this study. While extracting the bond lengths themselves is important, many other material properties can be inferred from their values and from the shape of transformed XAS spectra. Cation valence and coordination environment affects the atomic radii of cations [58], allowing for bond lengths determined through fitting to point towards particular cation valence states and coordination between tetrahedra and octahedra. This means that EXAFS fitting can be used to determine trends in these material properties as a function of cation stoichiometry, as will be shown in later chapters. In samples whose cations exhibit mixed-coordination or valence behavior, multiple nearest-neighbor bond lengths may form in the material. This is often seen in EXAFS spectra through the generation of abnormally-shaped or multiple peaks where one peak for a single bond length ought to be. Spectra that show this are a good indication of phase segregation in a material and this will be shown in some MCO samples in a later chapter.

Chapter 3

Study of $MnFe_2O_4$

3.1 Basics of $MnFe_2O_4$

MFO is a cubic structure spinel that favors the normal-type coordination configuration in which all manganese and iron cations are tetrahedrally and octahedrally coordinated, respectively [28,29,47]. Cation valences follow the typical 2+ and 3+ combination found in most spinels leading to Mn^{2+} and Fe^{3+} sites [52]. Compared to CMO and MCO, MFO has been the subject of numerous studies and is well understood from a materials characterization perspective [28,29,47,104]. Its ORR properties have also been explored by many groups in the past, although these studies focus on the material in a nanocrystalline or nanoparticle form [12,15,16,105]. Prior to this work, there had been no studies investigating ORR properties of epitaxially-grown MFO thin films. Also, only one other study exists concerning the study of MFO thin films grown by MBE [52], and it was involving a non-perovskite substrate. To further investigate MFO's ORR properties and contribute a study that further demonstrates its synthesis using MBE, MFO samples were grown and characterized with the primary objective of providing samples for use in catalysis experiments. Particular interest laid in examining the difference in ORR activity between the (001) and (111) facet faces of MFO in which (111) was previously found to show more impressive ORR properties [106]. Fe_3O_4 spinel thin films were also grown and studied for their ORR properties so that the role of manganese cations in MFO's catalysis might be better understood.

3.2 Sample Growth Parameters

MFO films were grown on either (001)-oriented or (111)-oriented Nb:STO conductive perovskite substrates (0.7 Nb wt%, MTI corporation) using MBE. MAO substrates are a closer lattice match to MFO, but conductive substrates were necessary for successful implementation of

catalysis experiments. Substrates were sonicated in acetone and isopropyl alcohol for about 5 minutes each before being loaded into the MBE chamber. Mn and Fe metals were deposited concurrently during growth and effusion cells were kept at constant temperature, with deposition rates calibrated using a quartz-crystal microbalance pre-growth. The sample stage was heated to a constant temperature using an infrared ceramic heating source and measured via a thermocouple on the stage, which causes an overestimation of ~50-100 ºC relative to the substrate surface temperature. Samples were grown at 525 ºC setpoints and subsequently cooled to ambient temperatures over ~30 minutes. O_2 gas was introduced into the chamber and maintained at ~$7.0x10^{-6}$ Torr during film growth and cooling. Fe_3O_4 was grown at the same conditions on (001)-oriented Nb:STO, except O_2 gas pressure was maintained at ~$4.5x10^{-6}$ Torr.

3.3 Measuring Oxygen Reduction Reactivity

A primary way in which a material's ORR properties are investigated is through allowing it and its cations to engage in oxygen reduction reactions as a cathode and measure the resulting current density through the material as a function of applied potential. To carry this out, MFO and Fe_3O_4 samples were made into rotating disk electrodes after sufficient material characterization was performed so that electrocatalysis experiments could take place using the films [107]. For proper implementation, the film surface must be immersed in a solution in which ORR takes place. Figure 3.1 shows a top-down schematic of an electrode with the film facing outward with an electrode cross section depiction of the layers adhered to the back of the sample. Epoxy covers every part of the electrode except for the film so that no other surfaces participate in ORR, such as the Nb:STO of the substrate. The electrode rotates while immersed so that O_2 molecules within the alkaline solution can more readily come in contact with cations of the film thereby initiating their participation in oxygen reduction reactions. While the electrode is immersed in alkaline

solution, a potentiostat setup is connected to concurrently set a potential difference between the solution and the sample while measuring the current passing through the electrode. The potential difference encourages cations of the film to engage in oxygen reduction reactions and electrons used in the reduction reactions to travel through the back of the sample to the surface. From these experiments, plots of current density through the electrode as a function of applied potential are generated. A brief discussion on the results of these experiments is found at the end of the chapter.

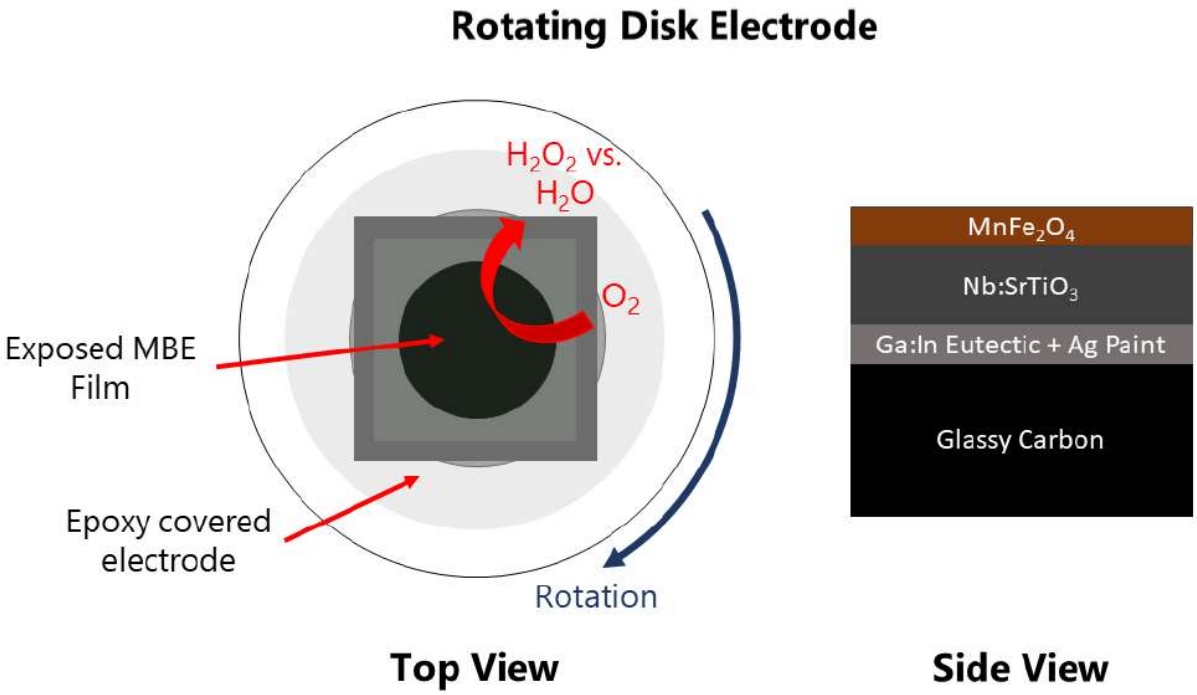

Figure 3.1 Top-down schematic of an electrode with the film facing outward and electrode cross section depiction of the layers adhered to the back of the sample.

The choice of a conductive substrate is mandatory so that current might easily pass through the electrode samples. While MFO and Fe_3O_4 grown on an insulating spinel such as MAO leads to high-quality layer-by-layer growth modes because they are identical structures and close in

lattice parameter, catalysis experiments would not be possible. Use of a Nb:STO perovskite substrate leads to an island growth mode and thus a rougher film surface, but it does allow for current to pass through the sample. Also, samples grown with an island growth mode still form single orientations and the islands themselves will be single-crystalline so long as conditions are ideal. This is the case for the MFO and Fe_3O_4 films of this study as seen through the characterization experiments performed on them. The uniformity of the thin film samples also make them ideal for catalysis experiments since surface area is directly related to ORR performance [24].

3.4 Substrate Crystal Orientation

Use of an Nb:STO substrate also allows for tuning of the resulting film's crystal orientation faceting at the surface. Nb:STO substrates with two distinct polished surface cuts were used to grow films: (001) and (111). Substrates with (001) cut surfaces lead MFO and Fe_3O_4 films to also take on a (001) crystal orientation along the growth direction, while substrates with (111) surfaces lead to MFO films with an (111) orientation as well. This is to say, a vector normal to a sample's surface lies parallel to both the substrate's and film's out-of-plane lattice direction vectors. MFO islands that formed on (001)-oriented samples grew in such a way as to expose a large amount of (111) faceting along the surface area of the islands. This led to islands that grew at predominately 36º angles with the surface in order to form (111) faceting along the side walls.

This behavior occurs primarily because the (111) crystal orientation represents the lowest energy surface of a spinel, meaning that the overall lattice energy will be reduced with a higher amount of (111) surface faceting as opposed to any other orientation [73]. The low energy surface also explains why (111)-oriented MFO films form smaller islands at the surface. (111)-oriented films already grow along the lowest energy surface, meaning that islands do not have to form 36º

angles to expose the lowest energy surface along the surface area. The overall roughness of (111)-oriented samples are thus significantly lower than (001)-oriented samples. Two MFO films that have identical stoichiometry, crystal structure and film thickness, but have differing amounts of crystal faceting exposed along their surfaces are ideal for a catalysis study investigating the effect that surface faceting has on a material's ORR properties. Catalysis experiments were carried out on two MFO samples that differed in this way, but results were inconclusive and both samples showed a comparable amount of ORR [74]. This could be because while (001)-oriented MFO might show a smaller amount of (111) faceting at the surface (thereby decreasing ORR activity [106]), it also shows higher surface area due to taller island morphology (thereby increasing ORR activity [24]).

3.5 Structure Properties

RHEED images in Figure 3.2(a,b) show the after-growth diffraction patterns of the 6 nm MFO films. The images show that MFO grown on (001)-oriented Nb:STO forms (001)-oriented spinel structures with island-like surface quality, while MFO grown on (111)-oriented Nb:STO forms a (111)-oriented spinel structure with both island and planar-like surface quality. These patterns persist throughout the growth process indicating that the orientations are uniform and have the same crystal structure throughout the films. Due to this surface morphology difference, (001)-oriented MFO possesses greater surface area in the form of pronounced islands compared to (111)-oriented MFO, which is more planar. Being of an island growth mode, all film crystal structures are considered fully relaxed with no in-plane lattice strain. AFM images show that the (001)-oriented MFO films have much higher surface roughness than the (111)-oriented film, consistent with RHEED results (Figure 3.2(c,d)). RMS roughness of the (001) and (111) films are 3.2(0.5)

nm and 1.0(0.5) nm, respectively, which further indicates the greater surface area of (001)-oriented samples. RHEED and AFM of the 16 nm MFO and 21 nm Fe_3O_4 film are found in the appendix.

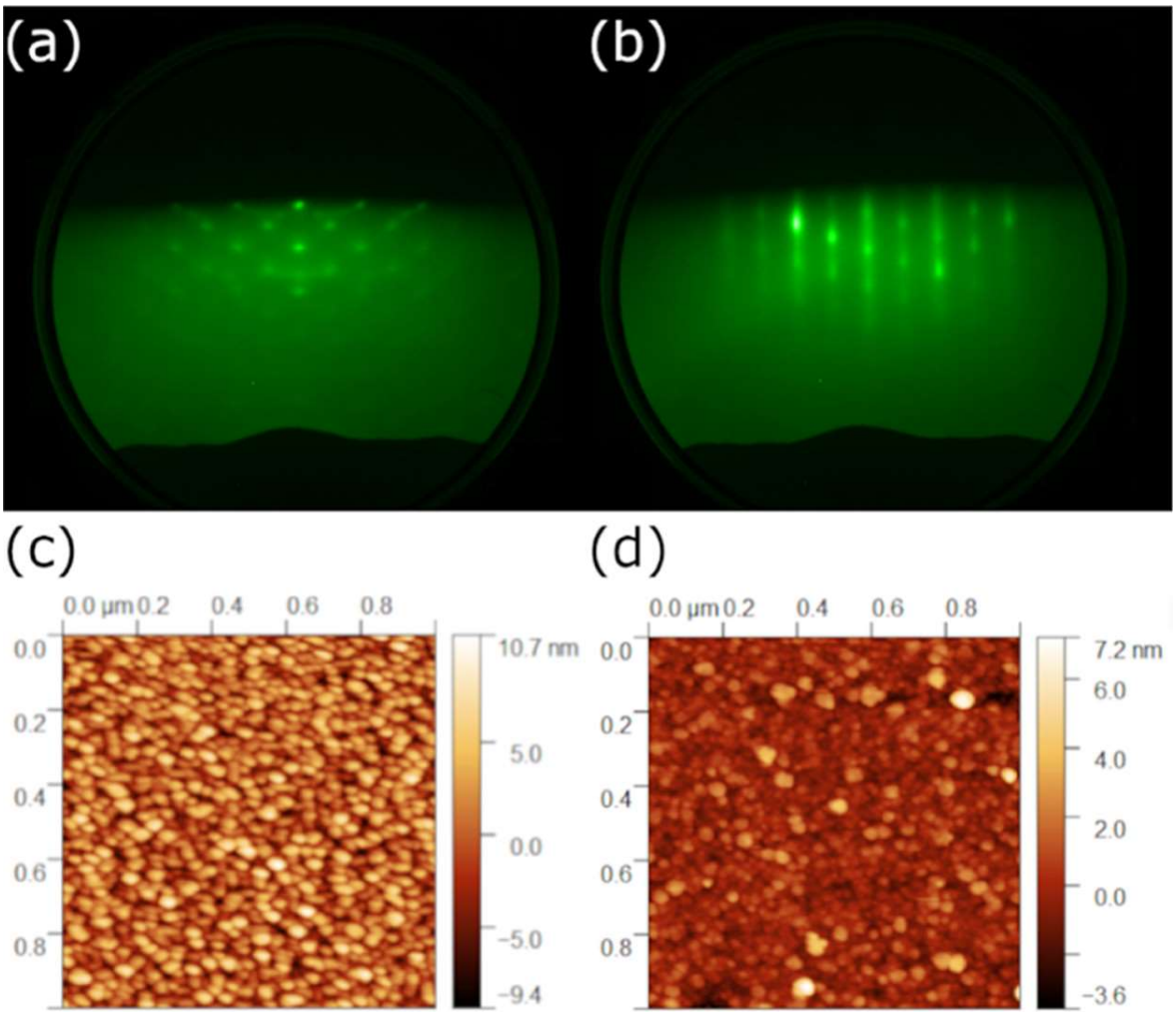

Figure 3.2 RHEED and AFM analysis of $MnFe_2O_4$ films grown on (a,c) (001) and (b,d) (111) substrates.

Out-of-plane XRD results for the MFO and Fe_3O_4 films are shown in Figure 3.3. (001)-oriented $MnFe_2O_4$ (Fe_3O_4) samples show (004) film peaks at 42.5 ° (43.3 °), close to the (002) substrate peak at 46.4 °. The (111)-oriented $MnFe_2O_4$ sample shows a (222) film peak at 36.6 °,

close to the (111) substrate peak at 40.0 °. c-lattice parameters of $MnFe_2O_4$ (Fe_3O_4) films are calculated to be 8.50(1) Å (8.35(1) Å) and the distance between (111) planes of $MnFe_2O_4$ to be 4.91(1) Å. These parameters are consistent with those found in literature for $MnFe_2O_4$ and Fe_3O_4 spinels [108,109]. Thickness of the $MnFe_2O_4$ film grown on (111) Nb:STO was determined using an XRR fit, but this could not be done for films grown on (001) substrates due to their significantly higher surface roughness. Thicknesses of these rougher films were calculated by comparing the composition, QCM calibration rates and growth time between all samples, while using the XRR thickness of $MnFe_2O_4$ grown on (111) Nb:STO in particular as a reference. Sample thicknesses, along with Mn-Fe stoichiometries, are shown in Table 3.1. XRD performed on samples after catalysis experiments indicated that there was no change in crystal structure during the process (Appendix).

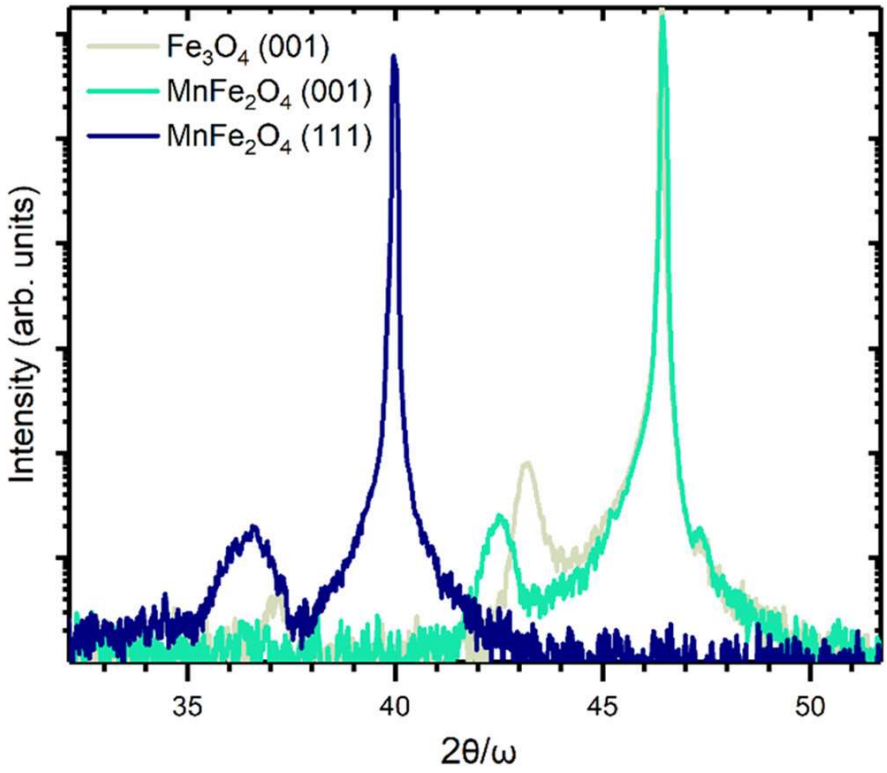

Figure 3.3 OOP XRD of MFO and Fe_3O_4 samples, showing large Nb:STO substrate peaks and smaller film peaks.

Table 3.1 Sample crystal orientations, thicknesses and cation stoichiometry.

Film	Orientation	Thickness (nm)	Mn at%	Fe at%
MFO	(001)	16(1)	31	69
MFO	(001)	6(1)	38	62
MFO	(111)	6(1)	34	66
Fe_3O_4	(001)	21(1)	0	100

STEM performed on (001)-oriented MFO shows the film's rough topography through a cross-sectional view of a surface island (Figure 3.4(a,b,i)). The island shows a 36º slope that faceted in order to expose a (111) spinel surface to the outside, thereby minimizing the lattice's energy [73]. The (111)-oriented MFO sample would show a much more level surface with smaller

islands, leading to reduced surface area overall. EDS shows an even distribution of Mn and Fe throughout the film reflecting a single phase and no cation migration to the surface (Figure 3.4(c-h)).

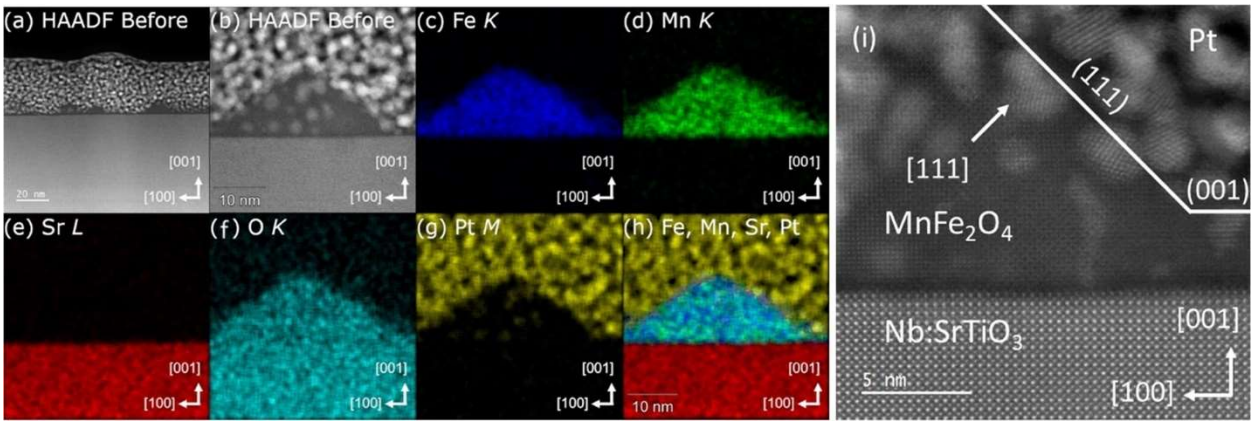

Figure 3.4 STEM and EDS of (001)-oriented MFO.

3.6 X-ray Photoelectron Spectroscopy

XPS data for Mn 2p and Fe 2p are shown in Figure 3.5, with stoichiometry results included in Table 3.1. Mn-Fe stoichiometry for samples still under vacuum was determined by comparing areas of the Mn 2p and Fe 2p regions after implementing sensitivity factors of 2.42 and 2.686, respectively, and Shirly background subtraction. Reliable stoichiometry determination from XPS is difficult without $MnFe_2O_4$ standards, and atomic concentration determined from XPS here should be considered as a high-Mn bound and low-Fe bound. RBS can often be used to determine stoichiometry but since Mn and Fe are so close in atomic number, metal peaks in the RBS spectra would be convolved and wouldn't be possible to fit with $MnFe_2O_4$ samples. It is possible that the MFO films' surface stoichiometry changed after catalysis experiments were performed, and the way to determine this would be to perform XPS after these experiments and determine

stoichiometry again. However, exposure to atmosphere greatly affects the bonding environment of a sample's surface, and 2p region spectra shapes among after-air samples varied wildly which made valid comparisons impossible. All spectra were binding energy-calibrated to place O 1s peaks at 530 eV (Appendix).

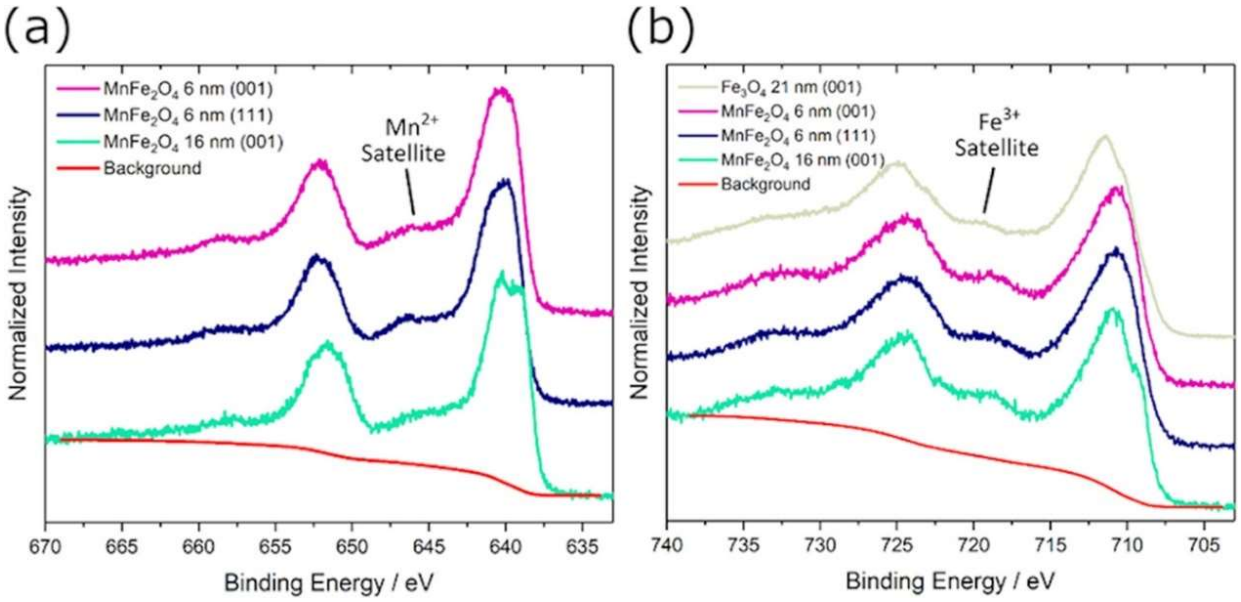

Figure 3.5 XPS spectra of (a) Mn 2p and (b) Fe 2p regions for MFO and Fe_3O_4.

Position of the satellites next to the Mn $2p_{3/2}$ peaks indicates a Mn^{2+} valence state [89], while position of the satellites next to the Fe $2p_{1/2}$ peaks indicates a Fe^{3+} valence for MFO samples [110]. Also, Fe 2p shows a satellite peak of mixed Fe^{2+} and Fe^{3+} valence for Fe_3O_4 [110]. In this way, XPS confirms the proper valence states that are expected for MFO and Fe_3O_4. Mn 3s spectra are comprised of two peaks, and the binding energy separation between them can be used to determine Mn valence [111]. However, the Fe 3s peak overlaps with Mn 3s region making definite valence determination from Mn 3s unreliable for MFO. XPS performed on samples after catalysis

experiments showed that the overall Mn^{2+} and Fe^{3+} valence character of MFO samples were unchanged after the process (Appendix).

As XPS is a surface-sensitive experiment, signal from a film's substrate is generally not seen in spectra if the film above is sufficiently thick. Before the catalysis experiments performed on samples were fully developed, it was suspected that early iterations of the experiments had the detrimental effect of stripping parts of the MFO film away from the substrate during the process. XPS performed on MFO after one of these early experiments showed this through the existence of large Sr and Ti peaks of the Nb:STO substrate that should be hidden underneath the MFO film (Figure 3.6(b)). In particular, an XPS survey showed high intensity peaks at the Sr 3p and Ti 2p regions at ~277 eV and ~460 eV, respectively. An interesting but unintended finding from XPS analysis of these samples has to do with the sensitivity depth of XPS. The survey of an MFO sample still under vacuum that is 6 nm thick shows a faint but visible indication of the Nb:STO substrate underneath. This was seen through small but clearly noticeable peaks at the Sr 3p and Ti 2p regions. It indicates that as a lower bound, XPS analysis for our system with an X-ray incidence angle of 45º is sensitive to just over the top 6 nm of a sample.

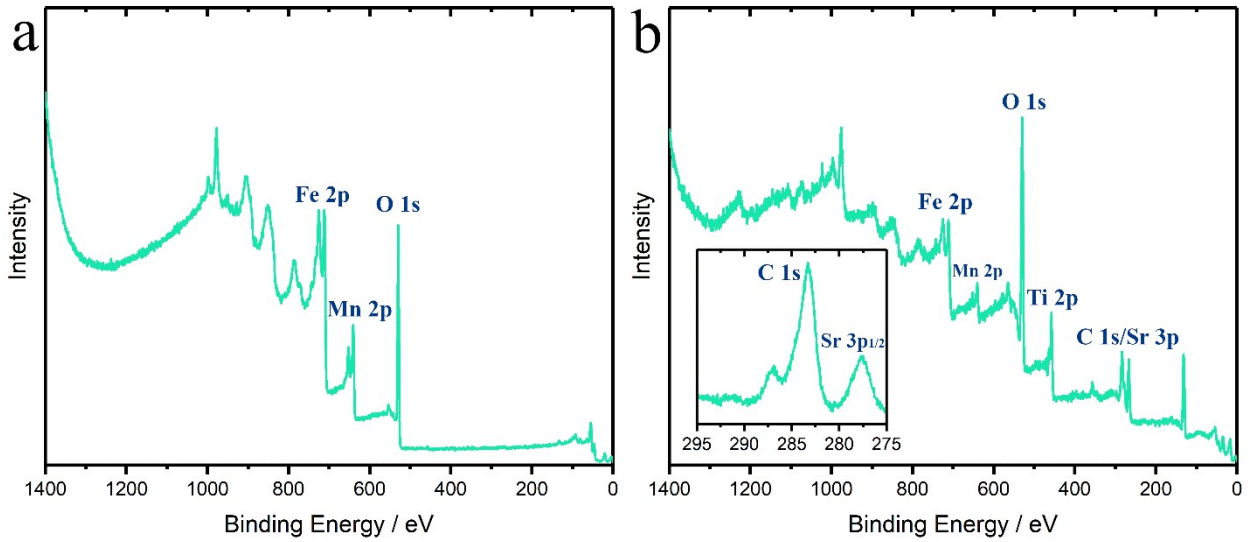

Figure 3.6 (a) XPS survey of an MFO sample under vacuum that shows only Mn, Fe and O signal and sufficient film thickness. (b) Survey and C 1s region inset showing Sr and Ti signal from the Nb:STO substrate, visible after the MFO film was partially stripped away during early catalysis experiments.

3.7 ORR Results from Catalysis Experiments

The following is a brief discussion of a few key findings from the catalysis experiments performed on the MFO and Fe_3O_4 samples. A more detailed discussion on the results can be found in a published journal article that covers the findings in depth [74]. Despite the hypothesis that MFO samples with more (111)-faceting would show better ORR activity than samples with more (001)-oriented faceting, this could not be explicitly determined from the catalysis experiments on these samples. This can be seen from analysis of the current density vs. applied voltage plots shown in Figure 3.7. In these experiments, samples in the form of electrodes were immersed in an alkaline solution and spun at particular rotations per minute to allow the slow-diffusing oxygen molecules to spread across the film surface and participate in catalysis. A potential was applied to the rotating

samples in solution starting from a higher applied potential to a lower potential. Figures 3.7(a-c) each show results for particular MFO samples which differ in terms of film thickness, and out-of-plane crystal orientation between (001) and (111). For each sample, there is a large rise in current magnitude when the applied potential reduces to ~0.2 V vs. RHE, which signifies the point in which the MFO sample starts to contribute to oxygen reduction reactions as a catalyst. In the context of these experiments, the higher the applied potential is when the current magnitude rises and catalysis begins, the better the ORR properties of the sample. As seen in Figure 3.7(a-c), the maximum current magnitude increases with higher rpm which occurs since oxygen is able to spread across the sample surfaces more readily.

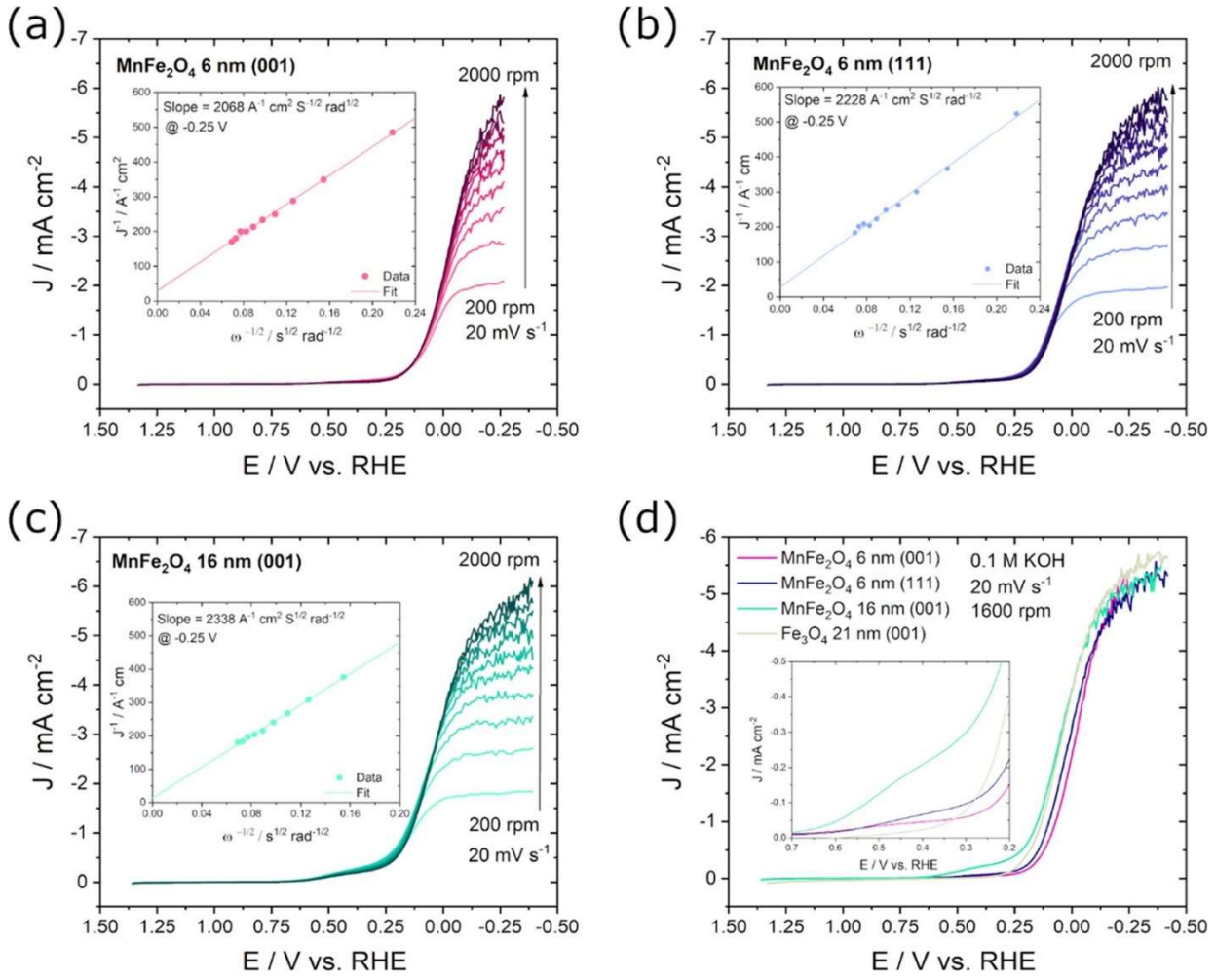

Figure 3.7 Current density vs. applied voltage plots for MFO and Fe_3O_4 samples, and at different rotation speeds. Data collected in an alkaline solution with O_2 to allow for sample cations to participate in oxygen reduction reactions. Here, a rise in current magnitude indicates when catalysis begins and this onset taking place at a more positive applied voltage indicates better ORR performance.

Figure 3.7(d) is the most important plot for comparing ORR activity between samples. It shows the 1600 rpm data for all three MFO samples along with one high-quality Fe_3O_4 sample on the same graph of current density vs. applied potential. The 6 nm (111)-oriented MFO film shows

a current magnitude rise and catalysis onset at a slightly higher applied potential compared to the 6 nm (001)-oriented MFO film. This indicates that the (111)-oriented MFO sample has better ORR properties than the (001)-oriented MFO sample. This was expected since the (111)-oriented MFO sample should have more (111) surface faceting than the (001)-oriented sample, and the (111) surface facet of MFO has shown higher ORR activity than the (001) facet before [106]. However, the thicker 16 nm (001)-oriented MFO sample shows catalysis onset at an even higher potential than for the 6 nm (111)-oriented MFO sample indicating the (001) sample shows better ORR. This should not be the case since the (111) sample is supposed to have a greater amount of (111) surface faceting and thus should show greater ORR properties. The conclusion is that the either the effect of surface faceting on MFO's ORR properties is not as significant as originally thought, or the variation in other properties between samples such as cation stoichiometry or film thickness has a greater effect on ORR properties than surface faceting prevalence.

A significant finding from the catalysis experiments is that the manganese cations of MFO do not contribute to the ORR properties of the material, and the catalysis onset and current magnitude rises seen in Figure 3.7 are solely because of activity from atomic iron sites. This was determined based on the applied potential in which catalysis onset took place. As seen in Figure 3.7(d), catalysis took place at around ~0.2 V vs. RHE in all samples including MFO and Fe_3O_4 which contains only iron cations. A material will begin contributing to oxygen reduction reactions when the applied potential is such that cations in the material are allowed to reduce from higher to lower valence states. The applied potential of ~0.2 V vs. RHE where catalysis is seen to occur in these samples corresponds to the applied potential in which iron is allowed to reduce from Fe^{3+} to Fe^{2+}. This was determined from another experiment measuring current density versus applied potential of these samples in which the samples were immersed in an inert N_2 environment instead

of an alkaline solution with O_2. A plot of this data is seen in Figure 3.8. Since the experiment took place in an N_2 environment, no catalysis could occur and variations in current density with applied potential reflect only the reduction and oxidation events of manganese and iron cations. As shown in Figure 3.8(a), the large rises in current magnitude at around 0.2 V vs. RHE indicates the applied potential in which iron reduces from Fe^{3+} to Fe^{2+}. Two other current magnitude rises are seen at around 0.92 and 0.65 V vs RHE, and these correspond to the reduction of Mn^{4+} to Mn^{3+} and Mn^{3+} to Mn^{2+}, respectively. As seen in Figure 3.7, there was no catalysis onset associated with these manganese reduction potentials, like there is with the iron reduction potential of ~0.2 V vs. RHE. This indicates that manganese cations did not contribute to catalysis in the MFO samples.

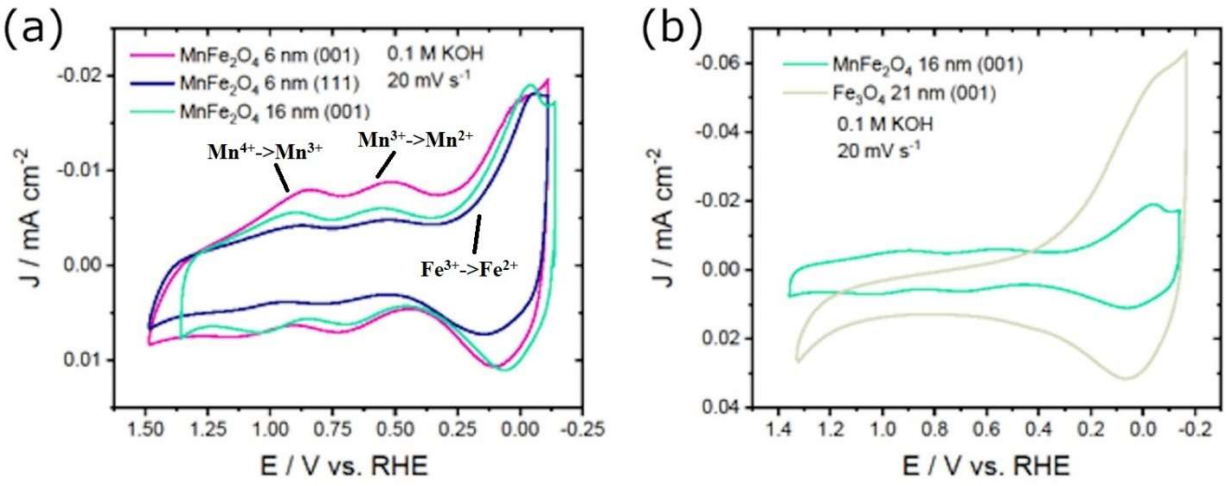

Figure 3.8 Current density vs. applied voltage plots in an N_2 environment with no rotation. An N_2 environment prevents oxygen catalysis from taking place but still permits reduction and oxidation of cations. Rises in current magnitude indicates when cation redox takes place.

3.8 Conclusion

This study is the first to involve catalysis experiments that investigate the ORR properties of MFO as an epitaxial thin film. Studying ORR in this way has many advantages including

guaranteed surface area uniformity between samples and zero porosity. The MFO and Fe_3O_4 films of this study are ideal representations of the materials as confirmed by clear spinel structure spectra in XRD and proper cation valence states in XPS. The analysis potential of XPS as a surface-sensitive technique was demonstrated by confirming that early catalysis experiments severely damaged MFO films and by using a 6 nm sample to identify the system's sensitivity depth. The novel use of a conductive Nb:STO substrate allowed for the implementation of samples as electrodes in catalysis experiments, and allowed for easy tunability of MFO's growth orientation between (001) and (111). While it was unclear if surface facet prevalence played a large role in the catalysis experiment results, it was found that iron cations are the sole contributor to the ORR properties of these high-quality MFO samples. This study is among the few to showcase the MBE growth of MFO thin films and the only to demonstrate the growth of MFO on Nb:STO.

Chapter 4

Study of $CoMn_2O_4$

4.1 Basics of $CoMn_2O_4$

The Co-Mn spinel system with end members $CoMn_2O_4$ (CMO) and $MnCo_2O_4$ (MCO) exhibits ORR properties on par with platinum [1,11,13,14], making these materials promising for efficient and affordable catalysis technologies as well as energy storage [17–20]. While CMO has been synthesized and studied in nanoparticle and nanocrystalline forms [1,4,12,17–20,32], characterization reports on CMO thin films are limited [70,112]. Coherent single crystal epitaxial films provide opportunities to tune properties through strain and to characterize fundamental material properties in the absence of grain boundary effects.

CMO is a tetragonal crystal structure spinel [1,18–20,32–35] that favors the normal-type configuration [32,33,45,46], and whose cations exhibit the typical 2+ and 3+ valance states common in most spinels [41]. This means that CMO possesses Co^{2+} and Mn^{3+} cations in tetrahedral and octahedral coordination, respectively. While most spinels possess a cubic crystal lattice structure, the Jahn-Teller (JT) effect induces the structure to take on a tetragonal structure. This occurs through the existence of Mn^{3+} octahedra where crystal-field splitting breaks the cubic symmetry [4,34–37]. Specifically, the JT-active Mn^{3+} ions in CMO break the degeneracy of partially-filled electronic d-orbital states [38,39]. This leads to elongation of the c-axis parameter through octahedral distortion, as illustrated in Figure 4.1(a).

Here, we focus on understanding the Co-Mn spinel material system through synthesis of epitaxial single crystal CMO thin films grown using MBE. We grew $Co_{1+x}Mn_{2-x}O_4$ films that vary in stoichiometry from ideal to increased cobalt, and studied them using characterization techniques to identify patterns between stoichiometry and material properties. We determine structural and

electronic properties of CMO that are contested or unreported in literature such as cation valence states through x-ray photoelectron spectroscopy and cation-oxygen bond lengths from x-ray absorption spectroscopy. We also present electronic structure calculations for models of CMO through use of density-functional theory

4.2 Sample Growth Parameters

The present work involves synthesis and characterization of epitaxial thin film samples of CMO with different metal stoichiometries, grown using MBE. All samples were grown on (001) $MgAl_2O_4$ (MAO) spinel substrates due to its isostructural template and small in-plane lattice mismatch with CMO. MAO's conventional in-plane parameter is 8.083 Å, while CMO's primitive in-plane parameter has been reported as 5.716 Å [1], which is equivalent to a conventional parameter of 8.144 Å after a 45° in-plane rotation. This produces a lattice mismatch of ~0.8% so that CMO experiences minor epitaxial strain. MAO substrates were sonicated in acetone and isopropyl alcohol for 5 minutes each before being loaded into the MBE chamber. Co and Mn metals were deposited concurrently during film growth and effusion cell temperatures were kept constant, with deposition rates calibrated pre-growth using a quartz-crystal microbalance. The sample stage temperature was controlled by employing an infrared ceramic heating source and measured via thermocouple on the stage, producing an overestimation (~50-100 ºC) relative to the substrate surface temperature. All samples were grown at 500 ºC temperature setpoints and subsequently cooled to ambient temperature over ~30 minutes. Atomic oxygen was introduced into the growth chamber by a radio-frequency plasma source with 300 W RF power. Oxygen plasma pressure was maintained at ~2.0×10^{-5} Torr during growth and decreased to ~2.9×10^{-6} Torr during cooldown of the sample stage.

4.3 Experimental Methodology Details

RHEED was used to monitor the growth process. Preliminary growths showed that lengthy exposure to RHEED adversely affected CMO films, forming a streak visible to the naked eye along the line the RHEED electrons were incident upon. To minimize this effect, use of RHEED was limited to quick bursts for image acquisition during and after sample growth (<2 seconds every 1-2 minutes). After cooling, samples were analyzed using *in-situ* XPS. Spectra were shifted to place their O 1s metal-oxygen bond peaks to 530 eV binding energy to compensate for the effect of the neutralizer (Appendix). Spectroscopic ellipsometry (SE) measurements were performed using a rotating analyzer based instrument with a compensator (V-VASE; J.A. Woollam Co., Inc.) over the spectral range from 0.4 to 5.8 eV. Data were fit to a general oscillator model after fixing the film thickness to specified values to extract values for the refractive index, n, and extinction coefficient, k. The absorption coefficient, a, was calculated from the extinction coefficient as $a = 4pk/l$, where l is the incident wavelength.

4.4 Results and Discussion

4.4.1 Structural Properties

For each of the $Co_{1+x}Mn_{2-x}O_4$ samples, the cation ratios were determined via RBS. This study focuses on four samples comprising nearly ideal CMO (x = 0.04) and Co rich cases (with x up to 0.24). Film thicknesses were determined through RBS fitting and XRR (Appendix). AFM images reveal extremely smooth films with root-mean-square roughness of less than 0.15 nm. RHEED patterns of the films match those of their MAO spinel substrates with slight streaking, owing to the small lattice mismatch between film and substrate and the smooth layer-by-layer growth (Figure 4.1(b)). Moreover, the unchanging diffraction patterns obtained with RHEED throughout the growth process show that the films are single-crystalline. RSM shows that films

are strained to the substrate with identical a- and b- lattice parameters, consistent with the unchanging RHEED pattern during growth. STEM-BF and EDS maps (Figure 4.1(c,d)) confirm that the film exhibits excellent compositional uniformity, without phase separation or defects, and that it possesses a sharp interface with the substrate. XRD of the samples aligns with a tetragonal crystal structure (Figure 4.1(e)) and confirm that they are all single-phase. Calculation of the *c*-lattice parameter from the films' (004) XRD reflections gives the values found in Table 4.1. All are reasonably close to values reported in literature (c = 9.252 Å [1], c = 9.095 Å [113]) and vary with stoichiometry. Epitaxial strain should only have a small effect on these parameters (~0.8% lattice mismatch). As will be explained later, we believe the increase in lattice parameter from x = 0.04 to x = 0.14 is due to excess Co filling interstitial sites as Co^{2+} tetrahedra, thereby expanding the crystal along the c direction. The decrease in lattice parameter beyond the x = 0.14 level could be attributed to excess Co replacing the JT-active Mn^{3+} octahedra with Co^{2+} octahedra.

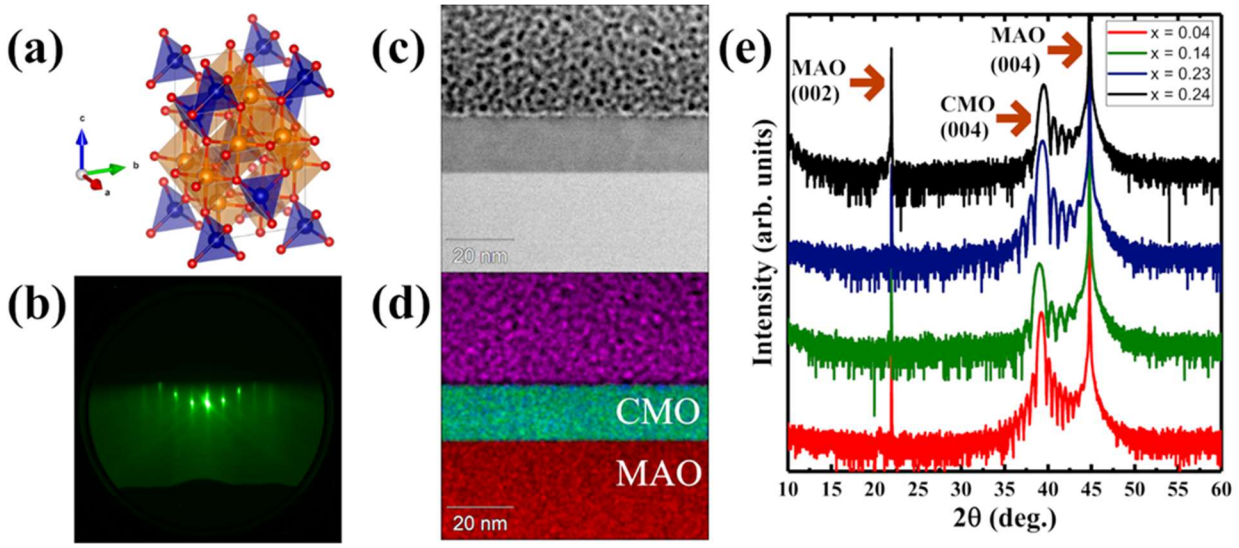

Figure 4.1 (a) Crystallographic model of $CoMn_2O_4$, where Co tetrahedra and Mn octahedra are shaded blue and orange, respectively; (b) RHEED image of CMO film after growth; (c-d) Cross-sectional STEM (c) and EDS map (d) of representative sample showing smooth MAO/CMO interface and homogeneous CMO film (red-Al K, green-Mn K, blue- Co K, magenta- Pt M edges); (e) Out-of-plane XRD of the four $Co_{1+x}Mn_{2-x}O_4$ films.

Table 4.1 c-lattice parameters of CMO samples calculated from (004) peaks of XRD data.

$Co_{1+x}Mn_{2-x}O_4$ Sample	c-lattice Parameter (Å)
x = 0.04	9.19(1)
x = 0.14	9.24(1)
x = 0.23	9.16(1)
x = 0.24	9.15(1)

4.4.2 X-ray Photoelectron Spectroscopy

XPS data for Co 2p, Mn 2p and Mn 3s are shown in Figure 4.2 with peak information found in Table 4.2. Despite changes in stoichiometry, overlapping spectra for various samples of both the Co 2*p* and Mn 2*p* spectra show that their peak shapes are nearly identical when

normalized, with $2p_{1/2}$ and $2p_{3/2}$ peaks at the same location. All Co 2p spectra possess a satellite peak on the high binding energy side of the Co $2p_{3/2}$ peak that is characteristic of the Co^{2+} valence state (Figure 4.2(a)) [89]. The Mn 2s and Co $L_3M_{23}M_{45}$ Auger regions overlap with Co 2*p* and contribute to a feature on the low binding energy side of each Co $2p_{3/2}$ peak located from about 778 eV to 770 eV. All Mn 2*p* spectra suggest a Mn^{3+} valence state due to the absence of an isolated satellite peak between the Mn $2p_{3/2}$ and Mn $2p_{1/2}$ peaks (Figure 4.2(b)), although delineation between Mn^{3+} and Mn^{4+} can be challenging for this region [89]. The binding energy separation between the multiplet peaks of Mn 3*s* can also be used to more readily identify Mn valence [111]. Fits to the Mn 3*s* peak for all CMO samples agree well with a 3+ formal charge (Figure 4.2(c), Table 4.2). The XPS data indicate that the CMO samples have identical cation valences despite changes in cation stoichiometry. Introducing excess Co would be expected to produce either a Co^{3+} ion on an octahedral site or charge transfer to yield a Co^{2+} and Mn^{4+} octahedral pair [11,114], which could lead to a hole on the Mn site. However, XPS shows static Co^{2+} and Mn^{3+} valence states with increasing Co. Excess Co remains as Co^{2+} regardless of whether it is tetrahedral or octahedrally coordinated.

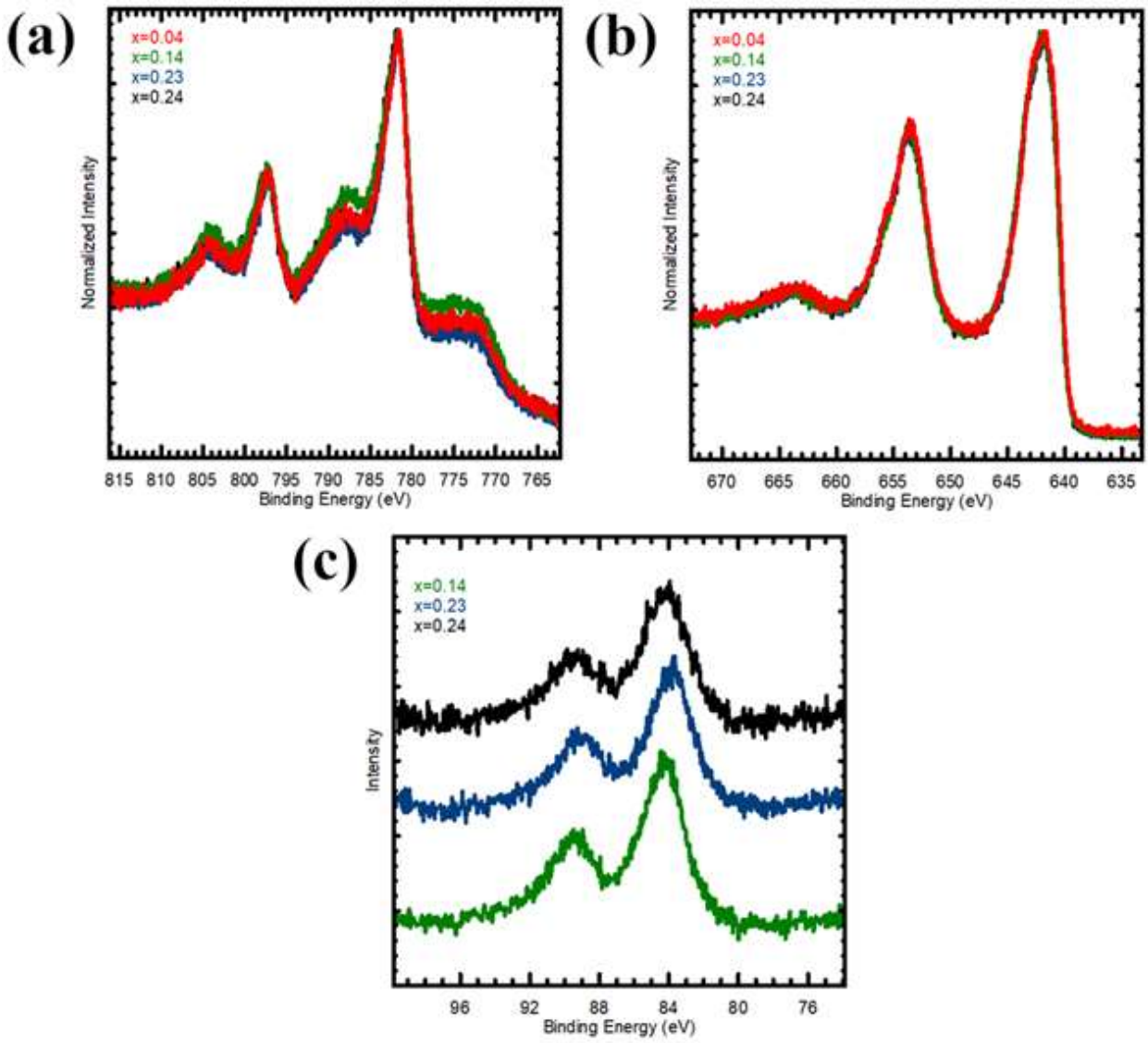

Figure 4.2 XPS data of (a) Co 2p; (b) Mn 2p; and (c) Mn 3s peaks for several samples.

Table 4.2 XPS Co and Mn $2p_{3/2}$ peak positions and Mn 3s multiplet separation values with valence state references [111].

	Peak Position (eV)		Separation	Mn^{2+} Ref:
Stoichiometry	**Co $2p_{3/2}$**	**Mn $2p_{3/2}$**	**Mn 3s (eV)**	5.68 eV
x = 0.04	781.7(1)	641.9(1)	-	**Mn^{3+} Ref:**
x = 0.14	781.7(1)	642.0(1)	5.2(2)	5.26 eV
x = 0.23	781.6(1)	641.8(1)	5.2(2)	**Mn^{4+} Ref:**
x = 0.24	781.8(1)	642.0(1)	5.2(2)	4.53 eV

4.4.3 X-ray Absorption Spectroscopy

To better understand the structural and chemical effects of substituting Co for Mn in the system, we performed XANES and EXAFS measurements on the $x = 0.04$ and $x = 0.14$ samples. Co and Mn *K*-edge XANES data of two CMO samples are shown in Figures 4.3(a,b). Since our RHEED and XRD data show single-crystalline films, polarization-dependent measurements follow selection rules for different transitions from the Mn and Co 1*s* states. The line shape differences—linear dichroism—between the in-plane and out-of-plane polarizations are due to the tetragonal structure asymmetry of CMO from the JT effect, with the Mn region showing particularly large dichroism. To our knowledge, there have been no previous reports of polarization-dependent K-edge measurement on single-crystals of either CMO or related JT-active Mn_3O_4. Pre-edge peaks (labeled "B") at ~6540 eV are consistent with predictions for JT-distorted Mn^{3+} in Mn_2O_3 and MnOOH [115]. All Mn *K*-edge data also show a large pre-edge feature at ~6550 eV (labeled "C") to the left of the usual *K*-edge peak location (labeled "D"). We could find no report of such a feature in polarized Mn *K* edge XANES, including theoretical models of many different Mn minerals [115]. Tetragonal $LaSrMnO_4$ with Mn^{3+} valence exhibits polarization-dependent dichroism, but no "double peak" feature like we observe here [116]. The feature is most

reminiscent of polarization-dependent effects in tetragonal ferroelectric titanates, including $PbTiO_3$ and $BaTiO_3$[117]. We tentatively attribute this feature to degeneracy breaking of the unoccupied Mn 4*p* states due to the JT distortion such that Mn $4p_z$ states accessible with perpendicularly-polarized x-rays lie at lower energy than the $4p_x$ and $4p_y$ orbitals. The in-plane measurements on both films are similar to what has been observed in $NiMn_2O_4$ inverse spinel films with a primarily Mn^{3+} valence [118].

As is the case with the XPS data, changes in sample stoichiometry had minimal effect on the XANES spectra. This suggests that there are no significant changes in the chemical coordination or electronic valence due to varying stoichiometry, at least up to the $x = 0.14$ excess Co threshold. The Co^{2+} and Mn^{3+} cation valences determined in XPS are also supported by inspecting XANES. Cation *K*-edges shifted towards higher photon energies indicate a higher cation valence state, and the in-plane-polarized Co and Mn *K*-edges of CMO are close to those of CoO (Co^{2+}) and Mn_2O_3 (Mn^{3+}) oxide [119,120], respectively. The Co K-edges of both samples exhibit relatively large pre-edge peaks at ~7708 eV (labeled "A"). Tetrahedral symmetry enhances the hybridization of cation-oxygen bonds, increasing the prevalence of 4*p*/3*d* hybridization in unoccupied orbitals which permits dipole transitions that contribute to pre-edge intensity. In the case of the normal spinel CMO, the lack of inversion symmetry in tetrahedra promotes hybridization of cation-oxygen bonds [96]. This pre-edge peak is seen in Co *K*-edges of $Zn_{1-x}Co_xO$ in which Co atoms are also tetrahedrally coordinated [119,121]. The peak intensity for each polarization on both samples is consistent with 100% tetrahedral coordination when compared to $Zn_{1-x}Co_xO$ data. These results between samples suggests that the additional Co for the $x = 0.14$ sample remains in tetrahedral coordination. This leads to the idea that Co interstitials cause the c-lattice parameter to increase between $x = 0.04$ to $x = 0.14$.

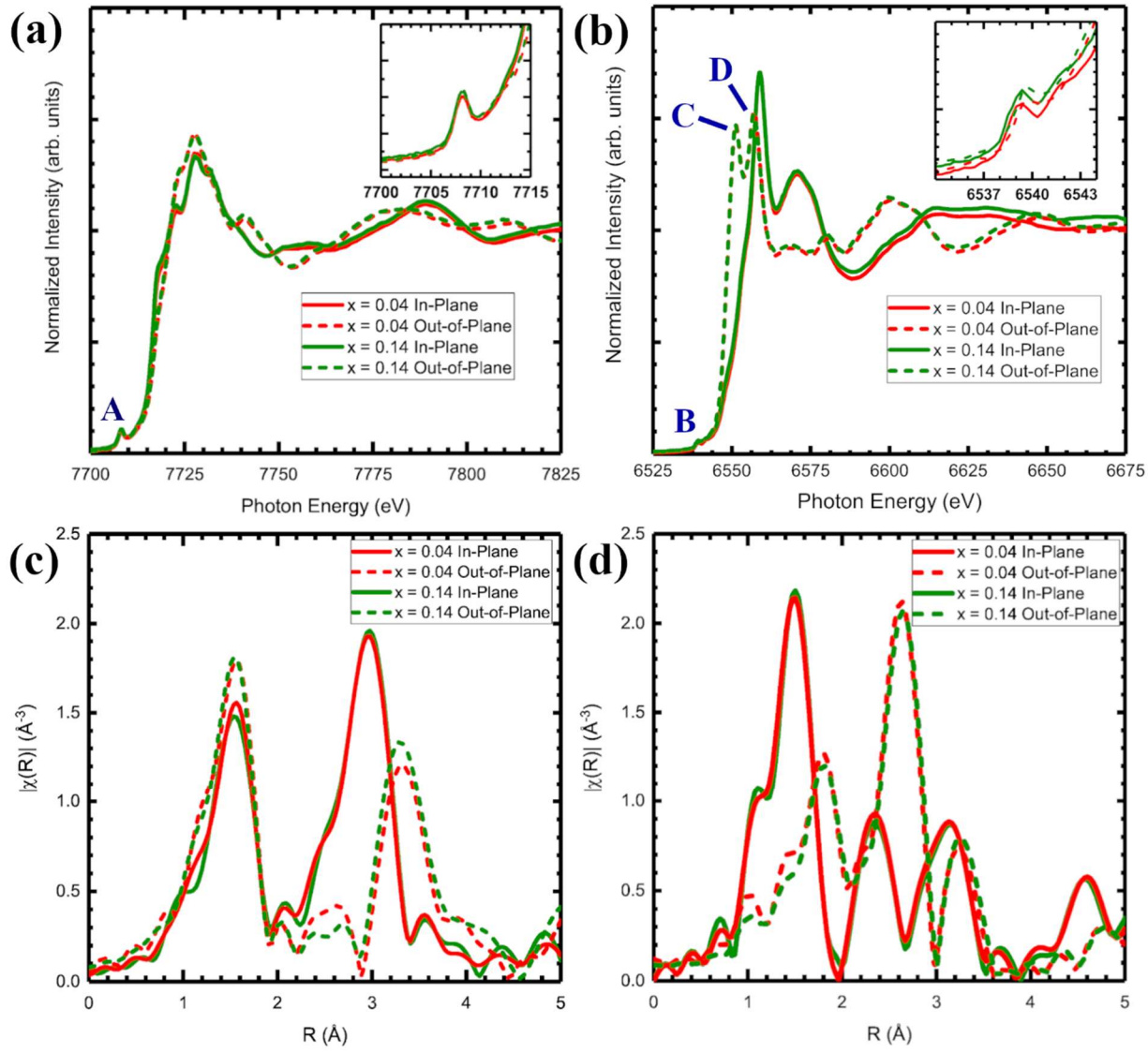

Figure 4.3 (a) Co K and (b) Mn K edge XANES for in-plane (parallel) and out-of-plane (perpendicular) polarizations; (c) Co and (d) Mn EXAFS extracted from XANES data in (a) and (b). Insets show pre-edge peak close-ups for both Co and Mn XANES.

4.4.4 Extended X-ray Absorption Fine-Structure Spectroscopy Analysis

From fits to the EXAFS data, we calculate the nearest-neighbor Co-O and Mn-O bond lengths for both the in-plane and out-of-plane polarizations (Table 4.3). There are no appreciable

differences between the two stoichiometries, indicating that introducing excess Co into CMO hardly affects bond lengths. There is no significant variation in the Co-O bond lengths between the two polarizations, which would follow from a nearly undistorted tetrahedral coordination of the Co atoms. We see no evidence of Co occupation in octahedral sites in the lattice. As would be expected from the JT distortion of Mn^{3+}, out-of-plane Mn-O bond lengths are larger than in-plane ones. The EXAFS bond lengths are compared to the combined Shannon crystal radii of the cation-oxygen bond [58] and the structure results from XRD on powder CMO [122]. The Co-O combination is consistent with bond lengths from EXAFS, while the Mn-O combination lies between the in-plane and out-of-plane bond lengths from EXAFS. This indicates that the octahedra experiences not only elongation along the c-lattice parameter, but also in-plane compression. The Mn-O bond lengths we report from EXAFS are also similar to those reported in $LaSrMnO_4$, which found 1.90(1) Å in-plane and 2.27(3) Å out-of-plane [116]. We note that the bond lengths may be affected slightly by the epitaxial strain between substrate and film, which would induce a slight in-plane reduction and out-of-plane expansion of the bond lengths.

Table 4.3 Co-O and Mn-O nearest neighbor bond lengths from EXAFS fits, as well as the combined crystal radii [58] and XRD results of powder CMO [122] for reference.

	In-Plane (Å)		**Out-Of-Plane (Å)**		**Crystal Radii (Å)**		**XRD Reference (Å)**	
Sample	**Co-O**	**Mn-O**	**Co-O**	**Mn-O**	**Co-O**	**Mn-O**	**Co-O**	1.967
***x* = 0.04**	1.97(1)	1.91(2)	1.96(1)	2.22(1)	1.96	2.02	**Mn-O, In**	1.965
***x* = 0.14**	1.97(2)	1.91(2)	1.96(1)	2.23(1)			**Mn-O, Out**	2.227

4.4.5 Density Functional Theory and Spectroscopic Ellipsometry

To better understand the electronic properties of stoichiometric CMO, we employed DFT+U models with different spin configurations, ranging from ferromagnetic systems (M_{FM} =

12 μ_B per formula unit) to antiferromagnetic (M_{AFM} = 0). CMO is known to be ferrimagnetic at lower temperatures and exhibits paramagnetism at room temperature [32,122,123]. While several features were similar across the different magnetic phases/structures (e.g. an indirect band gap for both spin populations), our description focuses predominately on the low-temperature ferrimagnetic phase (M = 3 μ_B), in which Mn atoms alternate between spin-up and spin-down, while Co atom spins are all parallel, to approximate the electronic structure. The in-plane lattice parameter found from first principles is 8.18 Å while the c-lattice parameter (c = 9.35 Å) presents in reasonable agreement with that obtained from XRD data. Figure 4.4 shows the projected density of states (DOS) and band structure of the ferrimagnetic case. An indirect band gap of approximately 0.8 eV is observed for the ferrimagnetic case. Band gaps ranged from approximately 0.5 eV (in the AFM case) up to approximately 0.8 eV in the ferrimagnetic model. The valence band in all cases arises as a result of the hybridization of the $3d_{z^2}$-orbitals of Mn or Co, and O-p bands as observed in Figure 4.4(b). The conduction band, in contrast, is formed by contributions from Mn-$3d_{x^2-y^2}$, O-p_x and O-p_y.

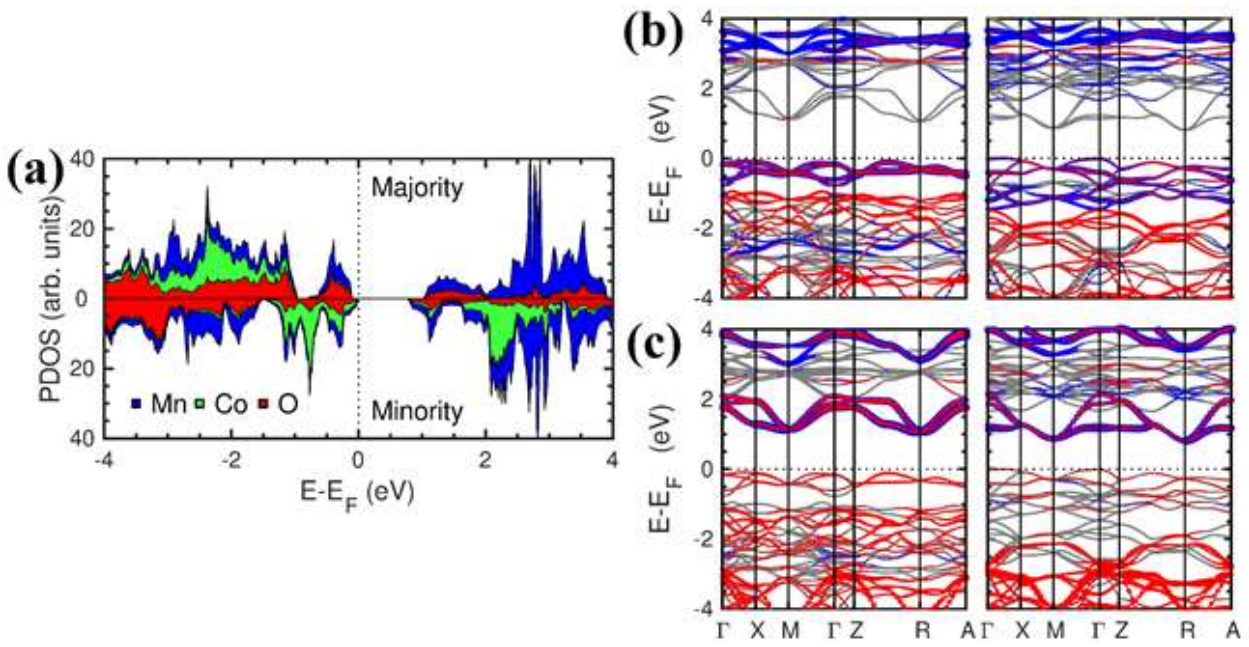

Figure 4.4 Electronic properties for the ferrimagnetic system (M = 3 μ_B) (a) Spin-polarized projected density of states indicating contributions from Mn (blue), Co (green) and O (red) localized atomic orbitals. Spin polarized band structure for spin majority (left) and minority (right) denoting contributions from: (b) Mn d_{z^2} (blue) and O p_z (red); (c) Mn $d_{x^2-y^2}$ (blue), O p_x and O p_y (red). The Fermi energy is placed at the valence band edge.

Figure 4.5 shows the dielectric (Figure 4.5(a)) and optical absorption (Figure 4.5(b)) of the CMO samples derived from fits to the spectroscopic ellipsometry data. All samples show similar absorption behavior regardless of stoichiometry differences, implying similarities in optical band gaps and electronic structure. Absorption features are located at similar photon energies, with no additional peaks appearing due to either free carriers (Drude response [124]) or optical transitions from different cation site occupancy. Two clear absorption peaks (inset to Figure 4.5(b)) are centered around 0.8 eV and 1.9 eV, respectively. Figure 4.5(c) shows the XPS valence spectrum of a CMO sample.

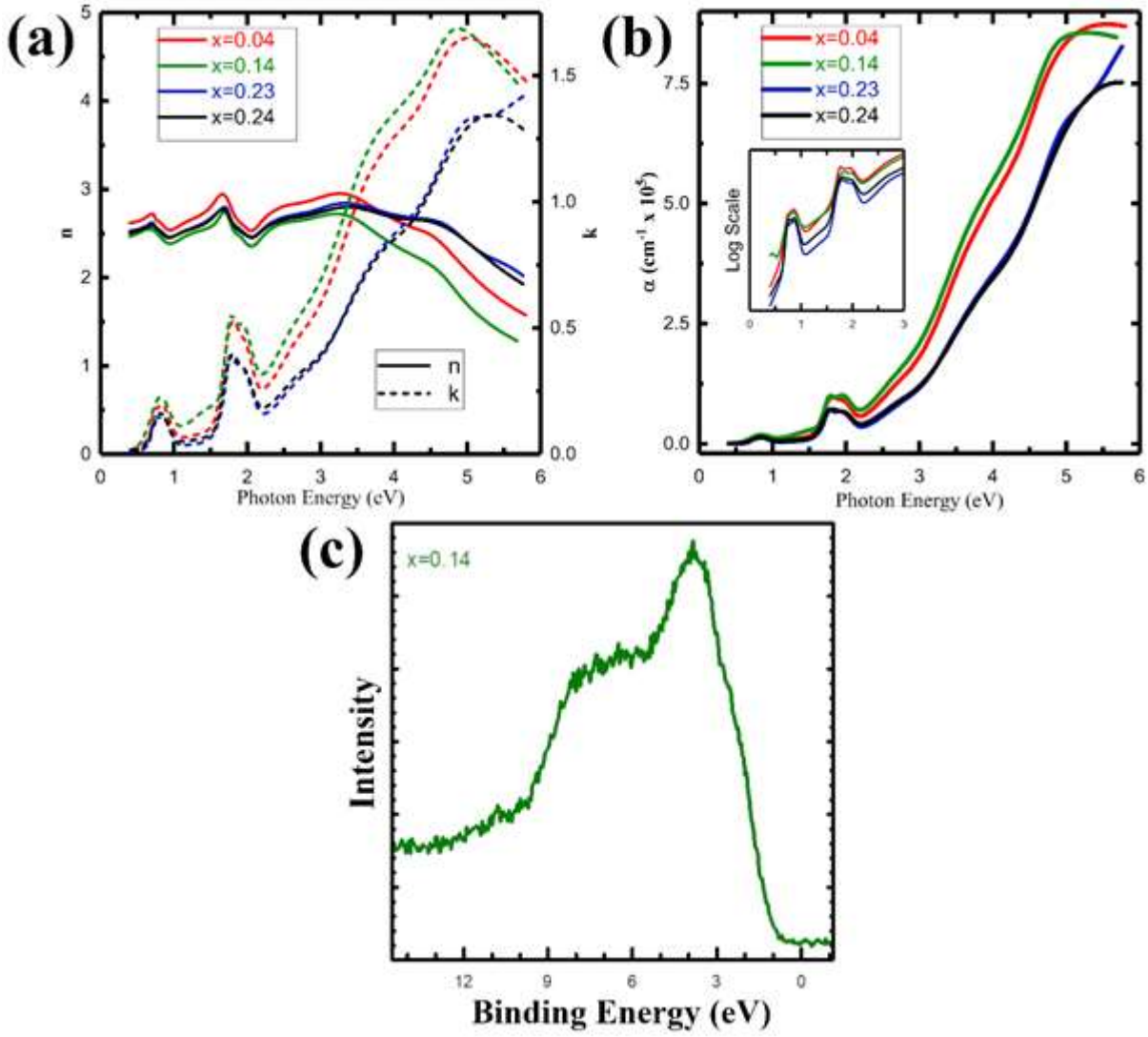

Figure 4.5 (a) Spectroscopic ellispometry data for various x values showing index of refraction n and extinction coefficient k. (b) Absorption coefficient for all 4 samples; (c) Valence band XPS data for x = 0.14.

In relating experiment to theory, we qualitatively compare the ellipsometry data to the DFT+U model of the ferrimagnetic case. The two absorption peaks likely represent transitions within the minority spin DOS, while the rise in intensity at higher energy represents allowed oxygen 2p to cation 3d transitions. The peak at 0.8 eV can be paired with the model's transition

from the hybridized Mn $3d_{z^2}$-O p_z valence band to the unoccupied Mn $3d_{x^2-y^2}$-O $p_{x/y}$ conduction band. Meanwhile, the peak at 1.9 eV can be paired with the transition from the Co-dominated minority valence band density around -0.8 eV to Co states in the conduction band. The narrow nature of these two optical transitions observed suggests that the Co and Mn *d* states may be more localized than the DFT model indicates. The strongest peak at ~3 eV binding energy likely corresponds to the large Co majority spin intensity at -2 eV in Figure 4.4(a).

4.5 Further Discussion

Our spectroscopic characterization results indicate that CMO exhibits little change in properties with increases in Co concentration from stoichiometric $CoMn_2O_4$. However, XRD shows the c-lattice parameter to increase from ideal $Co_{1+x}Mn_{2-x}O_4$ at $x = 0.04$ to $x = 0.14$, and then decrease with higher Co content at $x = 0.23$ and $x = 0.24$. XPS and XANES show static cation valences of Co^{2+} and Mn^{3+} despite changes in stoichiometry. This suggests that point defects induced during growth may drive changes in the system to preserve the Co^{2+} and Mn^{3+} formal charges instead of forming either an octahedrally-coordinated Co^{3+} ion or charge transfer to produce octahedral Co^{2+} and Mn^{4+}. XANES and EXAFS indicate that additional Co^{2+} ions are tetrahedrally coordinated at least up to $x = 0.14$, even though all tetrahedral lattice sites are filled. Co-O bond lengths from EXAFS remain almost unaffected by increased Co concentration, whereas octahedrally coordinated Co^{2+} should show variation since it is thought to be JT-active [39,42]. We believe that tetrahedral Co interstitials cause this c-lattice parameter increase with increasing Co from $x = 0.04$ to $x = 0.14$.

For additional Co^{2+} to remain tetrahedrally coordinated in the crystal, two types of point defects to consider are Co^{2+} interstitials and Mn^{3+} vacancies. An interstitial Co^{2+} requires Co-O bond lengths of ~1.96 Å in tetrahedral coordination, as seen from EXAFS. For this, there are 48

sites per conventional unit cell that are available depending on the tilting and bond angles of their surrounding polyhedral. In the case of no oxygen defects, charge balancing dictates that for every three Co^{2+} interstitials there must be two Mn^{3+} vacancies. Oxygen vacancies and interstitials should also be considered, but they are unlikely if we assume cation coordination is unchanged. There are no sites for oxygen interstitials that would leave Co or Mn coordination unaffected. Oxygen vacancies would change Co coordination since every lattice oxygen contributes to the tetrahedral geometry of existing Co^{2+}. Interestingly, we see no evidence of degradation in RHEED patterns with increasing Co concentration, so the crystal is seemingly tolerant of such point defects.

XRD shows the c-lattice parameter to decrease from $x = 0.14$ to $x = 0.24$ which would not follow from tetrahedral Co interstitials. It is more likely that in this higher-Co regime, excess Co^{2+} replaces Mn^{3+} in octahedral sites, although we lack XANES/EXAFS data for samples with greater Co, $x = 0.23$ and $x = 0.24$. With less JT-active Mn^{3+} octahedra, the c-lattice parameter would decrease. Tetrahedral Co interstitials could still be present in the higher-Co samples, but it seems there is a threshold between $x = 0.14$ and $x = 0.23$ in which cation substitution takes place.

While our films are single-crystalline as determined through RHEED and XRD, MCO nanoparticles have been seen to phase segregate into CMO and Co_3O_4 spinel [12]. It is possible that at our MBE growth conditions, there is a high-Co threshold in which extra Co would spill over to create Co_3O_4 after filling available interstitial sites in CMO. There could also be a range of differing growth conditions in which this phase segregation occurs with a low likelihood of Co interstitials forming. In particular, higher oxygen reactivity may encourage this phase segregation by allowing excess Co to form Co_3O_4 rather than filling interstitial sites in CMO. There could also be a range of differing growth conditions in which any excess Co would lead to increased cation valences either by forming Co^{3+} or transferring charge to form Mn^{4+}. This should also be more

likely at greater oxygen reactivities and might allow for a seamless transition from CMO to MCO without encouraging Co interstitials or phase segregation. Indeed, cation interstitials in CMO decreased as oxygen reactivity during growth increased [125]. Since MCO is predominately an inverse-type spinel [29,35–37], a transition from CMO to MCO would see Mn remain in octahedral coordination and some Co turn to octahedral coordination. Since MCO has a cubic structure [48], it should be that there are no JT-active Mn^{3+} octahedra that cause distortion. This suggests that the cation valences of single-crystal MCO would be Mn^{4+} and Co^{2+} as opposed to Mn^{2+} and Co^{3+}, and that a seamless transition from CMO to MCO would see an increase in Mn valence rather than Co valence. In the case of an increasing Mn valence, the c-lattice parameter would be expected to decrease since it is octahedrally coordinated Mn^{3+} that favors JT distortion. In fact, the JT distortion may be a significant driving force preventing the formation of Mn^{4+} states, as this ionic configuration would be energetically unfavorable in the tetragonal structure.

4.6 Conclusion

In this study we demonstrated the first growth of single crystal $Co_{1+x}Mn_{2-x}O_4$ spinel thin films with stoichiometries that range from ideal to increased Co. The structural and electronic properties of the samples were analyzed using an array of techniques that include *in-situ* XPS, XRD, STEM, XANES, EXAFS and SE. Co and Mn cations show consistent 2+ and 3+ valences across all stoichiometries. Additional Co causes Co and Mn cations to remain tetrahedrally and octahedrally coordinated, respectively, up to $x = 0.14$, then causes Mn to be substituted by Co in octahedral sites up to $x = 0.24$. All samples exhibit similar optical absorption behavior and cation-oxygen bond lengths. The fact that the electronic properties of these materials are barely affected by the replacement of Mn^{3+} with Co^{2+} may be attributed to the introduction of Co interstitials and Mn vacancies. This suggests that CMO's impressive ORR catalytic properties [1,11,13,14] would

be evident with various Co^{2+}/Mn^{3+} stoichiometries, potentially making it more stable under electrochemical conditions. It is possible that there is a high-Co threshold or differing set of growth conditions in which extra Co may form a secondary phase of Co_3O_4 as seen with $MnCo_2O_4$ [12], or lead to a smooth transition from $CoMn_2O_4$ to single crystal $MnCo_2O_4$.

Chapter 5

Study of $MnCo_2O_4$

5.1 Basics of $MnCo_2O_4$

MCO has been reported in literature to be a cubic, inverse-type spinel that does not experience any JT distortion [30,31,48,49]. It has shown to exhibit a high degree of ORR, surpassing the activity of MFO and CMO in some cases [1,11,13]. There have been numerous studies of the material in nanocomposite form [1,4,12,19,63,64], but very few studies involving thin films samples [49,69] and none reporting the growth of MCO using MBE. However, studies involving the experimental characterization of MCO have shown mixed results in literature, with some reporting single-phase samples and others reporting phase segregation and mixed-valence composition [12,51,53–55,59]. This suggests that it is either very difficult to synthesize high-quality single-phase MCO, or that a stable single-crystalline version of MCO does not exist. Also, conflicting reports on material properties such as cation valence indicates that there is room for studies that investigate the basic properties of MCO.

While 2+ and 3+ are the cation valences of most spinels, single-crystalline MCO may instead possess Mn^{4+} and Co^{2+} for valence states. In the case of standard Mn^{2+} and Co^{3+}, inverse-type MCO would place Co^{3+} into tetrahedral coordination which is a highly unfavorable configuration for this cation [56]. This leads to the idea that cobalt may instead take on a much more favorable 2+ valence with manganese adjusting itself to Mn^{4+} for charge balancing against O^{2-}. Other studies of MCO showing Mn^{4+} character support this idea [51,53–55] although without single-phase samples and reliable characterization, it is difficult to confirm. Spinels that exhibit 4+ and 2+ character are rare but do exist, and are known as “4-2 spinels” in literature [57]. As to this writing, there seems to be no studies that report MCO as a 4-2 spinel. This study seeks to

characterize MCO for its material properties including cation valences and investigate its phase segregation behavior while also providing a literature-first example of its thin film synthesis by MBE.

Understanding MCO of an ideal $MnCo_2O_4$ composition is critical to its future use in catalysis technology but studying how the material properties change with stoichiometry is also important. This includes how Co- and Mn-rich MCO behaves, but also investigating compositions that trend far towards Co_3O_4 and $CoMn_2O_4$. For this reason, $Mn_xCo_{3-x}O_4$ samples with a wide range of cobalt-manganese ratios were grown and studied from Co_3O_4 to $CoMn_2O_4$ with numerous samples in between. Findings from these samples act as a characterization map showing the material properties as a function of stoichiometry for the entire cobalt-manganese spinel system. For the purposes of this study, MCO-region and CMO-region indicate samples whose $Mn_xCo_{3-x}O_4$ stoichiometry lies below and above x = 1.5, respectively.

5.2 Sample Growth Parameters

MCO films were grown on (001)-oriented MAO spinel substrates (MTI corporation) using MBE. Substrates were sonicated in acetone and isopropyl alcohol for about 5 minutes each before being loaded into the MBE chamber. Mn and Co metfals were deposited concurrently during growth and effusion cells were kept at constant temperature, with deposition rates calibrated using a quartz-crystal microbalance pre-growth. The sample stage was heated to a constant temperature using an infrared ceramic heating source and measured via a thermocouple on the stage, which causes an overestimation of ~50-100 ºC relative to the substrate surface temperature. Samples were grown at 500 ºC setpoints and subsequently cooled to ambient temperatures over ~30 minutes. Oxygen gas was introduced into the chamber and maintained at set flow rates during film growth and cooling which resulted in varying oxygen pressures as indicated in Table 5.1. Significantly

lower oxygen pressures are required during cooldown to prevent surface reconstruction of MCO as in CMO, as was seen in RHEED when oxygen pressure was not lowered after deposition. As was the case in CMO, use of a radio-frequency plasma source was necessary to significantly increase oxygen reactivity by creating O^- ions out of O_2. RHEED was used as sparingly as possible, fearing that high energy electron incidence would adversely affect film quality as was the case with CMO synthesis.

RHEED patterns of all samples after cooling revealed them to contain spinel-structure phases, although some patterns show rough or defect-rich surfaces. Two example RHEED patterns are shown in Figure 5.1: one indicating a high-quality Co_3O_4 surface and another indicating a rough or defect-rich surface for an MCO sample. As will be seen, these lower-quality RHEED patterns may correlate closely with phase segregation or mixed-valence character of some samples. Stoichiometry of samples was determined by RBS fitting (Table 5.1), which is straight-forward due to the deconvolution of cobalt and manganese signal from other backscattering intensity. Film thickness was determined through fitting of XRR (Table 5.1) which was also straightforward due to the smooth film surfaces. RMS surface roughness was determined from AFM topography maps created for samples, all indicating smooth surfaces with RMS roughnesses below 1 nm.

Table 5.1 Stoichiometry, oxygen plasma synthesis pressures and film thicknesses of MCO-region samples. Film thicknesses determined with about 0.1 nm of uncertainty.

$Mn_xCo_{3-x}O_4$, x =	Oxygen During Growth (Torr)	Oxygen During Cooling (Torr)	Film Thickness (nm)
1.28	2.29E-05	3.43E-06	9.3
1.22	2.29E-05	3.37E-06	9.9
1.10	2.12E-05	3.27E-06	14.9
1.07	2.29E-05	3.37E-06	11.1
1.02	2.12E-05	3.27E-06	14.6
0.93	2.31E-05	3.76E-06	14.5
0.84	2.31E-05	3.79E-06	12.5
0.84	3.01E-05	4.16E-06	14.1
0.76	3.01E-05	4.31E-06	7.0
0.74	2.12E-05	3.27E-06	13.9
0.67	2.14E-05	3.48E-06	12.7
0.52	2.96E-05	4.08E-06	12.0
0.47	2.08E-05	3.42E-06	12.1
0.46	2.12E-05	3.42E-06	11.4
Co_3O_4	2.93E-05	4.47E-06	9.1

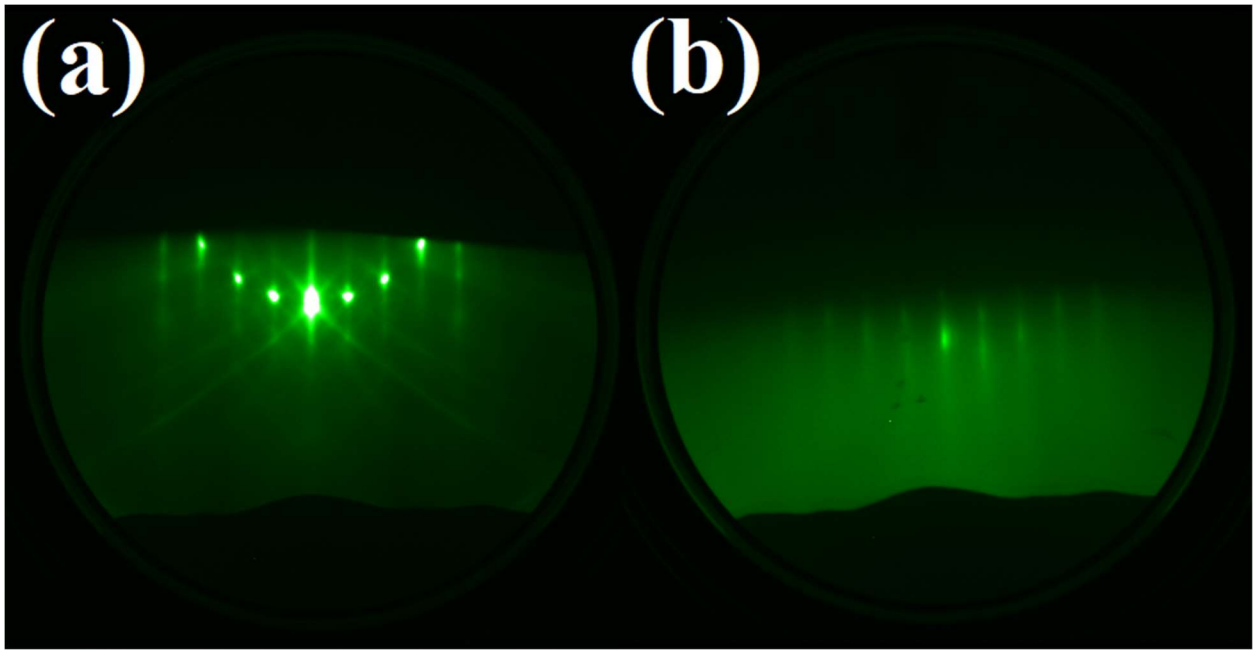

Figure 5.1 RHEED patterns for an a) high quality surface of Co_3O_4 and b) rough or defect-rich surface of an MCO-region sample ($Mn_xCo_{3-x}O_4$, x = 0.39). This MCO sample appears multi-phase in XRD which may explain its lower-quality surface.

5.3 Results and Discussion of Co_3O_4

5.3.1 Basics of Co_3O_4

Co_3O_4 is on the furthest Co-rich end of the cobalt-manganese spinel system and is a useful starting point for a discussion on MCO's properties as a function of stoichiometry. Co_3O_4 has a cubic crystal structure that trends towards a normal-type spinel [42,46,126]. It exhibits typical 2+ and 3+ cation valences placing Co^{2+} and Co^{3+} in tetrahedral and octahedral coordination, respectively [127]. Co_3O_4's lattice parameter of 8.086 Å [128] is very close to the MAO substrates' of 8.083 Å leading to a layer-by-layer growth mode with very low lattice strain. High-quality single-crystalline samples of Co_3O_4 were grown and studied using a variety of characterization methods. This confirmed known properties of the ideal material but also provided a baseline for

studying how the cobalt spinel changes with the introduction of manganese. The growth of Co_3O_4 thin films by MBE has been reported in literature before including synthesis using MAO substrates [129,130]. However, this study also involves EXAFS analysis of XAS data for the determination of Co-O bond lengths, which is highly valued in materials characterization.

5.3.2 Structure and Electronic Properties of Co_3O_4

High-quality RHEED images taken through the Co_3O_4 growth process showed the film to appear single-crystalline with very few defects, and perfectly strained to the substrate (Figure 5.1(a)). X-ray diffraction of the film is consistent with a cubic FCC spinel structure, and the OOP (004) peak is conolved with the substrate indicating the small lattice mismatch between film and substrate (Figure 5.3(b)). The OOP lattice parameter cannot be determined from XRD due to peak convolution, but an intensity shoulder next to the substrate peak indicates the value is only slightly higher than MAO's 8.083 Å. In-situ XPS shows a Co 2p spectrum with a satellite feature indicating the mixed 2+ and 3+ character of Co_3O_4, which is comprised of 1/3 Co^{2+} and 2/3 Co^{3+} (Figure 5.5(b)). This satellite shape is consistent with other studies involving XPS of Co_3O_4 [131].

5.3.3 X-ray Absorption Spectroscopy of Co_3O_4

XAS was performed on Co_3O_4 along with other MCO-region samples at a range of stoichiometry. Incident X-rays were linearly polarized allowing for the acquisition of data sensitive to either the in-plane and out-of-plane lattice directions only. A large pre-edge peak is seen in spectra of both polarizations near the cobalt K-edge (Figure 5.6a,b), indicating tetrahedral coordination of Co cations in the sample [94]. As will be seen, this pre-edge peak appears in Co XANES spectra for all MCO-region samples, indicating that tetrahedral sites remain occupied by cobalt and additional manganese occupies octahedral sites. This is also consistent with the presumed inverse-type spinel structure of MCO.

As was the case in CMO, analysis of the EXAFS region allowed for determination of cation-nearest oxygen bond lengths in Co_3O_4 and other MCO-region samples. However, cobalt cations are both tetrahedrally and octahedrally coordinated which means that spectra contain information from both lengths and fitting must account for both contributions. This can be done by introducing additional scattering paths into the fitting algorithm and adjusting the N degeneracy values accordingly. Determining multiple bond lengths from spectra is often challenging due to the large number of fitting parameters and uncertainty in results. A nearly continuous combination of lengths can result in valid fits that match spectra meaning the bond lengths fitted in this way should be heavily scrutinized.

One possible combination of lengths for tetrahedral Co^{2+} and octahedral Co^{3+}, respectively, is 1.91(1) Å and 1.90(1) Å from the in-plane spectrum and 1.92(1) Å and 1.91(1) Å from the out-of-plane spectrum. Despite the fact that these values for tetrahedrally coordinated Co^{2+} are lower than the value of 1.96 Å predicted through theoretical ionic radii [58], fitting error was low (Figure 5.2(a)) and similar bond lengths have been reported in other EXAFS analyses of Co_3O_4 [132,133]. Lattice strain is unrelated to this shrinking in tetrahedral bond length since the lattice mismatch between substrate and film is minor. Such lower bond length values for octahedral Co^{3+} correspond to the theoretical value for a low spin configuration of the cation (1.92 Å) meaning that growth of Co_3O_4 leads to a version in a low spin state. As will be seen, similar bond lengths were determined for other Co spectra of MCO-region samples indicating that values did not vary greatly with the addition of manganese.

While these bond lengths for Co_3O_4 may be physically accurate, other combinations of lengths lead to acceptable fits to the EXAFS data and therefore may be valid. To demonstrate this, Figure 5.2(b) shows the fitting results for in-plane Co in which tetrahedral Co^{2+} was purposefully

assigned to the theoretical value of 1.96 Å and octahedral Co^{3+} was allowed to fit freely. This resulted in the octahedral Co^{3+} bond length taking on a value of 1.92 Å, which makes the bond length values of this fit identical to those predicted through ionic radii [58]. This demonstrates how determination of bond lengths from spectra in which multiple lengths are involved is prone to inaccuracy, and results should be considered possibilities rather than definite values.

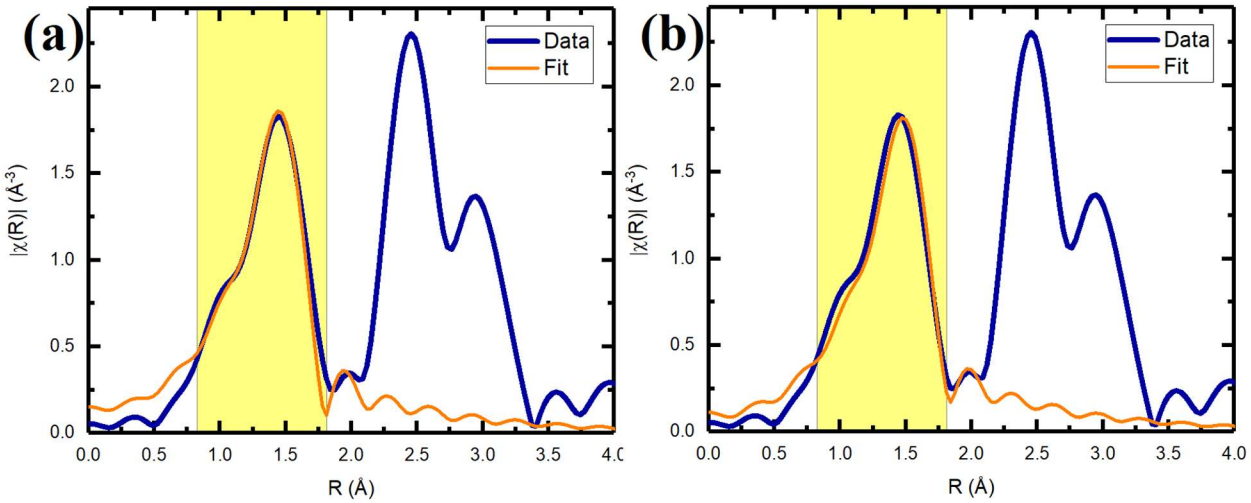

Figure 5.2 Two EXAFS fits for the in-plane cobalt spectrum of Co_3O_4. Fits correspond to bond lengths of a) 1.91(1) Å and 1.90(1) Å and b) 1.96(1) Å and 1.92(1) Å for tetrahedral Co^{2+} and octahedral Co^{3+}, respectively. Fit bound ranges are highlighted.

5.4 Results and Discussion of $Mn_xCo_{3-x}O_4$

5.4.1 X-ray Diffraction and Phase Behavior of $Mn_xCo_{3-x}O_4$

Starting with the characterization results of Co_3O_4 helps in discussing changes in material properties that comes with the introduction of manganese into the spinel system towards $MnCo_2O_4$. MCO-region samples tended to exhibit phase segregation behavior with increasing manganese content. Phase segregation presented itself most clearly in OOP XRD spectra in which secondary

film peak signals were apparent in some samples where a single (004) spinel peak should be. Location, intensity and broadness of peaks varied greatly among phase segregated samples with some examples being shown in Figure 5.3(a). It is not clear if all multiple film peaks are due to the (004) FCC diffraction condition or if some reflect a material with a different crystal structure entirely.

As will be shown later, even samples that appear to be single-phase in XRD show a tendency to display mixed manganese valence character between Mn^{3+} and Mn^{4+}. Single-phase samples appear so in OOP XRD through the existence of only a single (004) film peaks with some examples shown in Figure 5.3(b). This phase segregation and mixed-valence behavior indicates that single-phase structures become more unstable with increasing manganese content. Despite this unstable nature, RSM shows that single-phase MCO samples are strained to the substrate as well as some phase segregated ones.

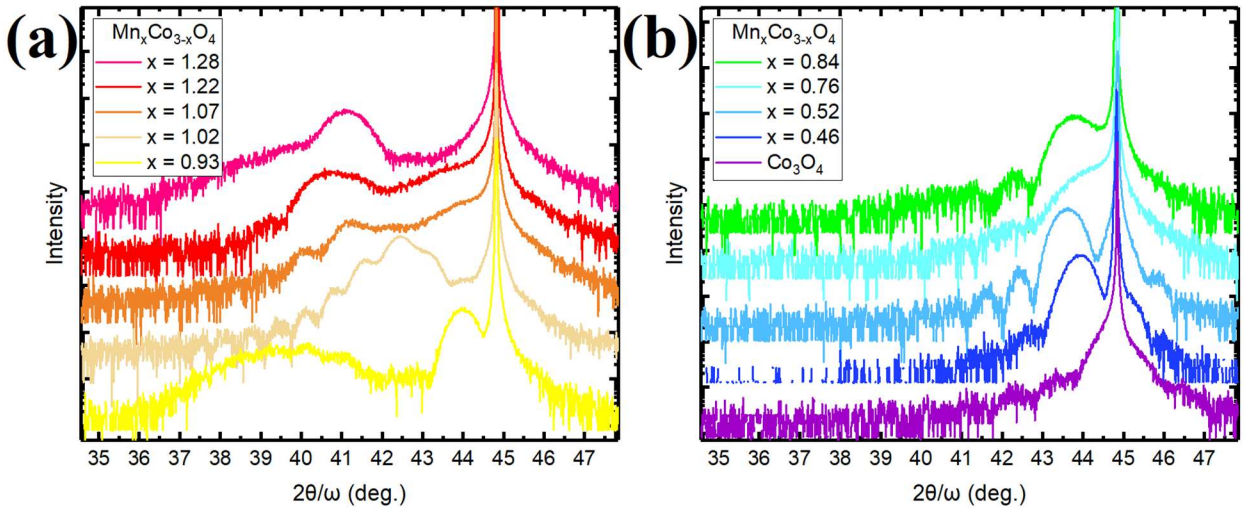

Figure 5.3 OOP XRD spectra of MCO-region samples that are a) phase segregated showing multiple film peaks and b) single-phase showing a single (004) spinel film peak.

As further evidence of phase segregation, Figure 5.4 shows STEM and EDS images for sample x = 1.02 which has close-to-ideal MCO stoichiometry. Contrast is seen in the film portion of the sample cross-section, especially in the medium-angle annular dark field (MAADF) and bright-field (BF) images. MAADF images are sensitive to strain and defects within a material, while BF images are particularly sensitive to lower atomic number atoms such as oxygen. The EDS map showing an overlap of cobalt and manganese cations indicates that the elements have spread inhomogeneously in the film (Figure 5.4(d)), with Mn having migrated towards the sample surface. The phase segregation in this sample that has close-to-ideal $MnCo_2O_4$ stoichiometry leads to the question of whether a stable single-phase version of the material exists, or whether it will seek to form multiple phases as seen in samples of other studies [12,59]. The findings of this study indicate that MCO does have a stable single phase, albeit with uncommon cation valence states for a spinel.

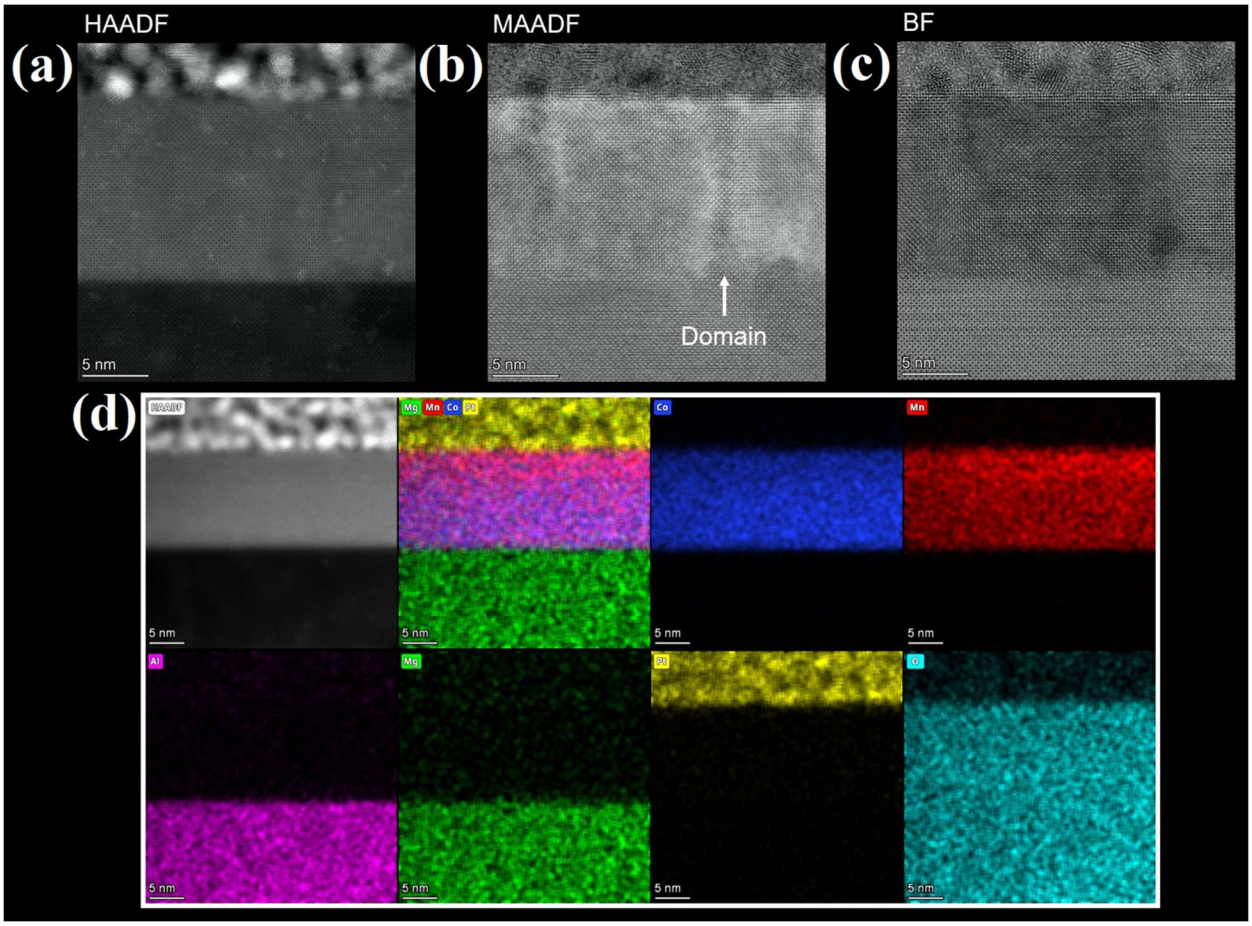

Figure 5.4 (a-c) STEM and (d) EDS of the $Mn_xCo_{3-x}O_4$ sample x = 1.02, depicting phase segregation. Shown are (a) high-angle and (b) medium-angle annular dark field and (c) bright-field images. EDS shows migration of manganese towards sample surface.

Despite showing multiple film peaks, OOP XRD of phase segregated samples generally have an obvious primary peak with greater intensity than others, and the c-lattice parameters corresponding to each primary peak position was determined using Bragg's Law. The c-lattice parameters and phase behavior of MCO-region and CMO-region samples are shown in Table 5.2. Trends are difficult to see from the table but a plot displaying these parameters shows that both phase segregation behavior and c-lattice parameter tend to increase with higher manganese content until samples reach stoichiometries close to $CoMn_2O_4$ (Figure 5.5). MCO-region and CMO-region

indicate samples whose $Mn_xCo_{3-x}O_4$ stoichiometry lies below and above x = 1.5, respectively. The plot indicates a clear increase in c-lattice parameter and phase segregation tendency with increasing manganese content among MCO-region samples. CMO-region samples show no phase segregation and in fact possess single-crystalline tetragonal structures [41].

Table 5.2 c-lattice parameter from primary peaks of OOP XRD spectra and corresponding phase behavior of MCO-region samples.

$Mn_xCo_{3-x}O_4$, x =	c-lattice Parameter (Å)	Phase Behavior
2.12	9.25	Single-Phase
2.08	9.25	Single-Phase
1.99	9.19	Single-Phase
1.86	9.23	Single-Phase
1.77	9.14	Single-Phase
1.76	9.12	Single-Phase
1.28	8.78	Multi-Phase
1.22	8.84	Multi-Phase
1.10	8.52	Multi-Phase
1.07	8.74	Multi-Phase
1.02	8.50	Multi-Phase
0.93	8.23	Multi-Phase
0.84	8.46	Multi-Phase
0.84	8.23	Single-Phase
0.76	Convolved with substrate	Single-Phase
0.74	8.26	Single-Phase
0.67	8.37	Single-Phase
0.52	8.30	Single-Phase
0.47	8.23	Single-Phase
0.46	8.24	Single-Phase
Co_3O_4	Convolved with substrate	Single-Phase

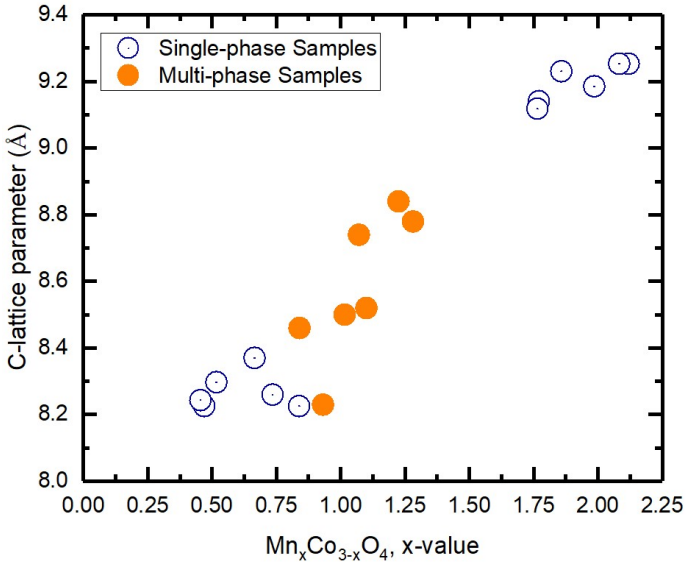

Figure 5.5 Plot of primary peak c-lattice parameters from OOP XRD as a function of $Mn_xCo_{3-x}O_4$ stoichiometry. Data in blue and orange correspond to single-phase and phase segregated samples, respectively.

While possible mechanisms for phase segregation will be discussed later, three possible contributions can be given for the rising c-parameter. One, manganese atoms generally have a larger ionic radius than cobalt atoms leading to longer bond lengths and unit cells. Two, ionic radii of cations and thus bond lengths change depending on their valence state and coordination environment. Samples with octahedral manganese with valence character trending towards Mn^{3+} (1.96 Å or 2.025 Å) rather than Mn^{4+} (1.91 Å) will show longer bond lengths on average [58]. Three, JT distortion of Mn^{3+} octahedra causes immense stretching along the out-of-plane lattice direction as seen in CMO [41]. As will be shown later through multiple analyses, manganese cations appear to occupy octahedral coordination sites in MCO-region samples. Greater manganese content means a higher number of manganese octahedra including Mn^{3+} octahedra

specifically in samples with mixed valence character. Samples with a greater number of Mn^{3+} octahedra would then drive up the c-lattice parameter through JT distortion.

Previous studies of ideal stoichiometry $MnCo_2O_4$ show a supposed cubic structure with a lattice parameter of 8.09 Å to 8.29 Å [134–136], but the sample in this study closest to MCO shows a c-parameter of 8.50(1) Å. This sample also shows phase segregation and multi-valence character, and thus JT distortion of Mn^{3+} octahedra is likely to have contributed to the substantial increase in parameter above what is expected. Since other MCO-region samples exhibit relatively high c-lattice parameters and show mixed-valence character, it is likely that JT distortion takes place in these samples as well. This indicates that manganese cations within the crystal take on octahedral coordination rather than tetrahedral. This claim will be supported through other analyses later and it is consistent with an inverse-type spinel structure.

Notable in Table 5.2 is the $Mn_xCo_{3-x}O_4$ sample x = 0.76 which is a single-phase MCO-region sample with an OOP XRD film peak convolved with the substrate's peak. The significantly lower lattice parameter indicates that there are very few JT-active manganese octahedra and thus the sample exhibits primarily Mn^{2+} or Mn^{4+} character as opposed to Mn^{3+}. As will be shown later, multiple analyses show that the manganese valence for this sample appears to be predominately Mn^{4+}. It will also be argued that this single-phase sample supports the idea that $MnCo_2O_4$ does have a stable single phase that is comprised of Mn^{4+} and Co^{2+} as opposed to Mn^{2+} and Co^{3+} as a typical spinel would have. Also clear from Figure 5.5 are the greater c-lattice parameters of CMO-region samples which stems from the large amount of JT-distortion taking place due to manganese solely occupying octahedra as Mn^{3+} in the spinel structure.

5.4.2 X-ray Photoelectron Spectroscopy of $Mn_xCo_{3-x}O_4$

In-situ XPS of MCO-region samples indicate that all manganese is either in a Mn^{3+} or Mn^{4+} state, with no Mn^{2+} found in any sample (Figure 5.6(a)). This is because the satellite feature characteristic of Mn^{2+}, which would be found between the $2p_{1/2}$ and $2p_{3/2}$ peaks, is not seen in the Mn 2p spectra [52]. Mn 2p spectral shapes of Mn^{3+} and Mn^{4+} appear identical and thus even qualitative determination of manganese valence from this region was not attempted. XPS also shows a general trend from mixed Co^{2+} and Co^{3+} character towards predominately Co^{2+} character with increasing manganese content. This is seen through the changing shape of the satellite feature of the Co 2p XPS region, which is located between the $2p_{1/2}$ and $2p_{3/2}$ peaks (Figure 5.6(b)). The changes show progressively less indication of Co^{3+} in higher-manganese samples, with some samples even depicting ideal Co^{2+} satellite features [41]. All spectra were binding energy shifted appropriately to place their O 1s region peaks at 530 eV (Appendix).

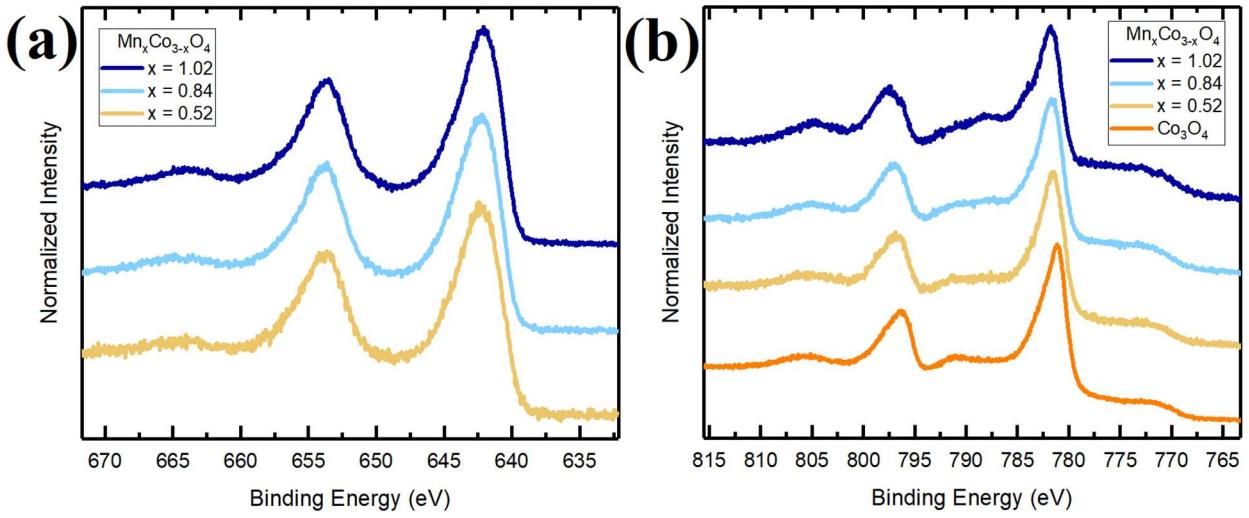

Figure 5.6 XPS spectra of $Mn_xCo_{3-x}O_4$ MCO-region samples for a) Mn 2p region and b) Co 2p region. The changing shape of the Co 2p satellite feature (~788 eV) indicates the trend in valence towards Co^{2+} with increasing manganese.

Assuming additional manganese takes on octahedral coordination as indicated in multiple analyses of this study, this lowering of cobalt valence could correspond with the replacing of Co^{3+} with Mn^{3+} or Mn^{4+} in octahedral sites. In the later case of Mn^{4+} occupation, another Co^{3+} octahedral cation would be incited to reduce to Co^{2+} for charge balancing and thereby leading to $MnCo_2O_4$ valences of Mn^{4+} and Co^{2+}. As will be shown, many of the MCO-region samples of this study show mixed valence character between Mn^{3+} and Mn^{4+} indicating that both octahedral site substitutions may take place, with Mn^{3+} leading to higher c-lattice parameters due to JT distortion. The phase segregation behavior of MCO-region seems closely tied to mixed-valence behavior, and it could be that Mn^{4+} is the proper manganese valence of MCO while Mn^{3+} cations are considered valence state defects that lead to phase segregation behavior.

5.4.3 X-ray Absorption Spectroscopy of $Mn_xCo_{3-x}O_4$

In-plane and out-of-plane polarization XAS was performed on MCO-region samples with a range of stoichiometry from Co_3O_4 to Mn-rich MCO. Co-region spectra for all samples and polarizations look remarkably similar regardless of stoichiometry (Figure 5.7a,b), as do all in-plane Mn-region spectra (Figure 5.7(c)). However, out-of-plane manganese spectra do show variation with changing stoichiometry through the appearance of a pre-edge feature at ~6550 eV of the K-edge (Figure 5.7(d)). This pre-edge feature intensity is similar in appearance to the pre-edge features shown in out-of-plane manganese spectra of CMO samples [41]. This indicates that changing properties between samples, including phase segregation tendency and multi-valence character, is driven by manganese but not cobalt. This also suggests that the changing material properties are rooted in causes that are anisotropic along the out-of-plane direction. This also makes sense considering that RSM shows most films to be strained to the substrate in-plane, indicating their a- and b-lattice parameters are identical.

Mn^{3+} character most likely explains the appearance of the pre-edge feature since most of these MCO-region samples exhibit some mixed manganese valence character between 3+ and 4+, and CMO samples is comprised solely of Mn^{3+} manganese. Considering the relatively large c-lattice parameters of these MCO-region samples and the tetragonal crystal structure of CMO, this pre-edge feature may be a general indication of JT distortion of Mn^{3+} octahedra and of a tetragonal crystal structure. Also, the existence of these pre-edge features further supports the idea that all manganese cations in MCO-region samples take on octahedral coordination. One $Mn_xCo_{3-x}O_4$ sample, x = 0.76, shows no pre-edge feature intensity in its out-of-plane manganese spectrum indicating that this sample is comprised predominately of Mn^{4+} as seen in other analyses as well. While this single-phase, single-valence sample is Co-rich compared to $MnCo_2O_4$ stoichiometry, it may be an indication that ideal MCO does have a stable single phase with Mn^{4+} and Co^{2+} valence states.

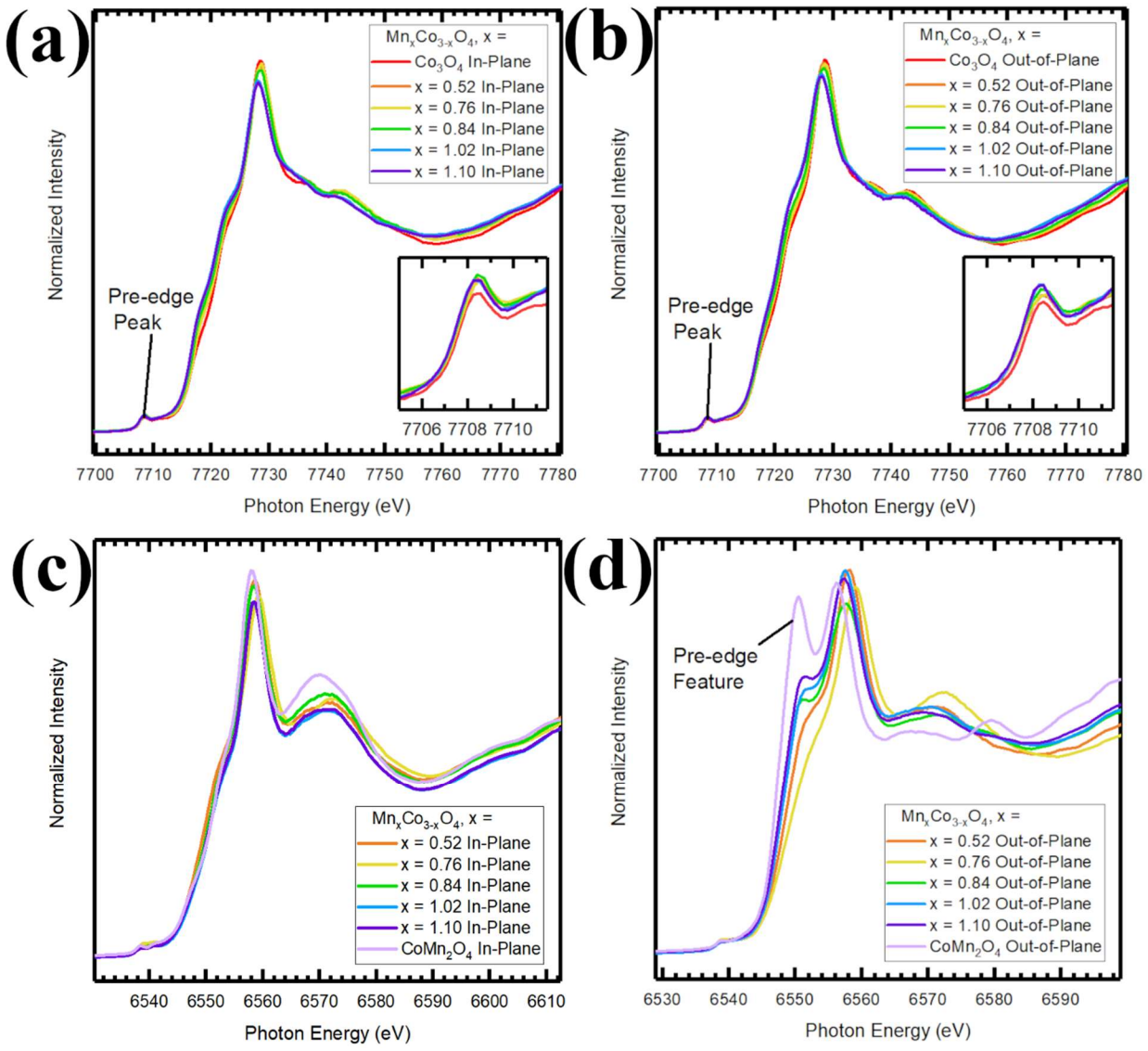

Figure 5.7 XAS spectra for $Mn_xCo_{3-x}O_4$ MCO-region samples showing a) in-plane cobalt region, b) out-of-plane cobalt region, c) in-plane manganese region and d) out-of-plane manganese region (with the addition of CMO sample x = 1.99.) Cobalt region spectra include insets that show pre-edge peaks with consistent intensity between samples.

Cobalt-region XANES for all samples and both polarizations show high-intensity pre-edge peaks at the base of the K-edge (insets of Figure 5.7a,b). The intensities of the peaks are consistent between samples and because pre-edge intensity is an indication of tetrahedral coordination for

cobalt [96], all tetrahedral sites appear to be fully occupied by cobalt regardless of sample stoichiometry. This follows for an inverse-type MCO spinel in which all cobalt would be found in tetrahedral sites and further supports the idea that manganese takes on octahedral coordination.

Linear combination fitting of both in-plane and out-of-plane cobalt region spectra shows a trend in valence character from mixed Co^{2+} and Co^{3+} towards Co^{2+} with increasing manganese stoichiometry (Table 5.3). Fitting was performed by using Co_3O_4 (2.67+ Co valence) and CMO (2+ Co valence) spectra as fitting standards and this trend in cobalt valence confirms what was also seen in comparing Co 2p XPS spectra. Linear combination fitting of in-plane Mn shows no clear trend with varying stoichiometry and indicates the mixed-valence character of the MCO-region samples of this study. Fitting was performed using CMO (3+ Mn valence) and MnO_2 (4+ Mn valence) as standards and results confirm that most samples exhibit mixed Mn^{3+} and Mn^{4+} character. While linear combination fitting can show general trends in cation valences between samples, exact valence determination is not possible since fitted and reference spectra do not share identical structures.

Table 5.3 Linear combination fitting results for MCO-region samples, using Co_3O_4, CMO and MnO_2 spectra as standards.

Sample	In-plane Co spectra		In-plane Mn spectra	
$Mn_xCo_{3-x}O_4$, x =	% Comp. of Co_3O_4 (Co^{2+} and Co^{3+})	% Comp. of CMO (Co^{2+})	% Comp. of MnO_2 (Mn^{4+})	% Comp. of CMO (Mn^{3+})
CMO Sample	0	1	1	0
1.10	0.64	0.36	0.87	0.14
1.02	0.62	0.38	0.84	0.16
0.84	0.77	0.23	0.93	0.07
0.76	0.88	0.12	0.69	0.31
0.52	0.85	0.15	0.98	0.02
Co_3O_4 Sample	1	0	-	-
MnO_2 Standard	-	-	0	1

Analysis of Co-region XAS derivative plots for both polarizations also shows trends in Co valence from mixed 2+ and 3+ towards Co^{2+} with increasing manganese stoichiometry. This trend is seen by comparing each derivative plot's two Co^{2+} and Co^{3+} peak intensity values between samples, which are found at ~7717 eV and ~7727 eV, respectively (Figure 5.8(a)). Table 5.4 shows each peak's maximum intensity value and associated ratio between them for a given spectrum, and it is seen that ratios increase in favor of higher Co^{2+} intensity with additional manganese content in a sample. While XAS derivative plots of Co-regions show two distinct peaks for Co^{2+} and Co^{3+}, analysis of Mn-region plots is challenging since both Mn^{3+} and Mn^{4+} constitute one single peak (at ~6558 eV) that shifts in energy position depending on valence state (Figure 5.8(b)). Table 5.4 shows the energy position of each sample's manganese peak as well as the position relative to a CMO sample's peak position, for all in-plane spectra. CMO represents complete Mn^{3+} character while peaks that trend towards higher binding energy represent increasing Mn^{4+} character towards the position of a MnO_2 standard's peak representing Mn^{4+} character. As in linear combination

fitting of spectra, there are no clear trends in manganese valence with sample stoichiometry, however the peak position of $Mn_xCo_{3-x}O_4$ sample x = 0.76 lies at higher binding energy than the peak position of Mn^{4+}, indicating that this sample is predominately comprised of Mn^{4+} cations as opposed to Mn^{3+}.

Table 5.4 XAS first derivative analysis results for out-of-plane cobalt and manganese spectra. Co-region analysis focuses on a comparison between the maximum intensity values of the 2+ and 3+ peaks, and Mn-region analysis focuses on tracking the energy position of the single Mn^{3+}-Mn^{4+} peak between samples.

Sample	Out-of-plane Cobalt Spectra			Out-of-plane Manganese Spectra	
	Maximum Intensity Value		Ratio	Peak Maximum Position (eV)	
$Mn_xCo_{3-x}O_4$, x =	2+ Peak	3+ Peak	2+/3+	Actual Position	Relative to CMO
CMO Sample	-	-	-	6555.16	0.00
1.10	0.132	0.174	0.76	6555.58	0.42
1.02	0.127	0.169	0.75	6555.58	0.42
0.84	0.140	0.187	0.75	6555.24	0.08
0.76	0.135	0.214	0.63	6557.39	2.23
0.52	0.128	0.202	0.63	6556.34	1.18
Co_3O_4 Sample	0.111	0.229	0.49	-	-
MnO_2 Standard	-	-	-	6556.34	1.18

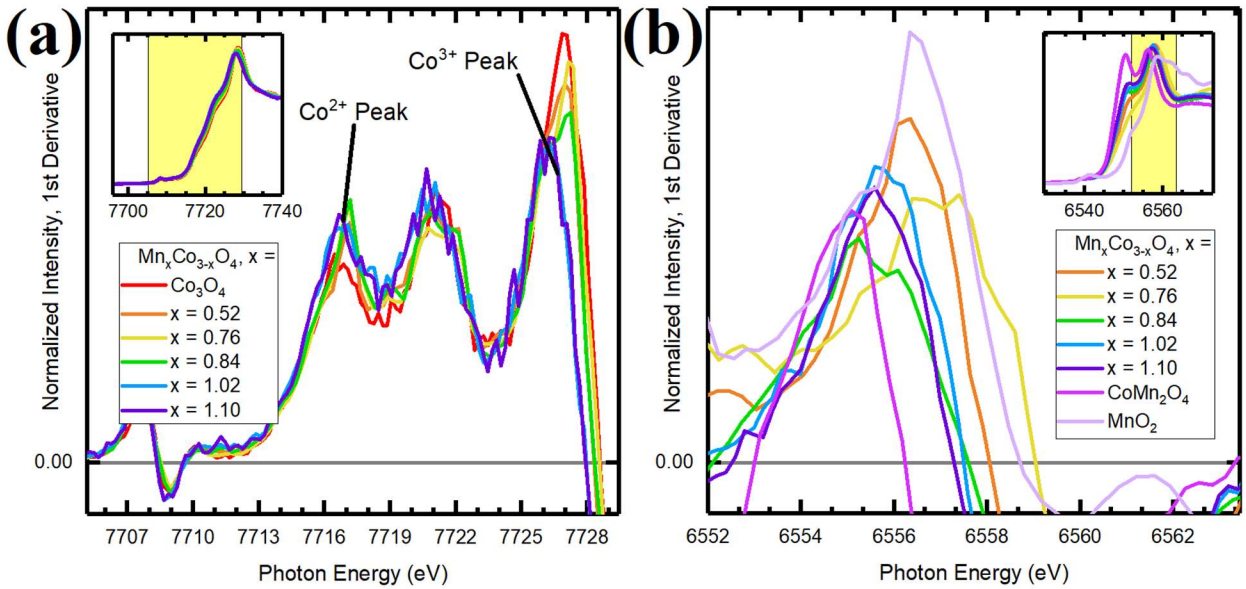

Figure 5.8 First Derivative XAS plots for out-of-plane spectra of a) Co-region and b) Mn-region. Data includes MCO-region samples as well as CMO and MnO2 spectra in Mn-region

5.4.4 Extended X-ray Absorption Fine-Structure Spectroscopy Analysis of $Mn_xCo_{3-x}O_4$

While EXAFS fitting of CMO bond lengths was straightforward, determining lengths for MCO-region samples was more challenging. CMO samples were single-crystalline with one coordination and one valence state for each cation, while MCO-region samples show cations with multiple coordinations and mixed-valence character. Not only do theoretical ionic radii depend on cation coordination and valence state [58], JT distortion drives large changes in bond lengths with the introduction of Mn^{3+} in octahedral sites. This is especially problematic in fitting out-of-plane manganese spectra for samples that show both Mn^{3+} and Mn^{4+}. All this leads to multiple bond lengths in the material for a given cation and must be accounted for in fitting spectra by introducing additional scattering paths into the fitting algorithm. As was discussed previously in regards to fitting Co_3O_4 data, determining multiple bond lengths from one spectrum is difficult because multiple combinations of lengths will lead to acceptable fits.

All fits assume that manganese in the lattice is octahedrally coordinated so that all models assume fully tetrahedral coordination of cobalt and an appropriate number of manganese octahedra according to stoichiometry. This follows from the analysis results discussed previously that show octahedral coordination of manganese and from the nature of an inverse-type MCO spinel. Also, out-of-plane manganese spectra of most MCO-region samples show indications of multiple bond lengths due to the shape of their nearest-neighbor oxygen scattering path peaks. Figure 5.9 shows a spectrum showing a single Mn-O bond length along with two spectra showing multiple Mn-O bond lengths.

The nearest neighbor oxygen peaks are found within the range of about 1 to 2 Å. The general shape of a single-length scattering path is a single peak with a shoulder on its left side, while a peak that appears widened or misshapen appears in the case of multiple scattering paths. The peak for x = 0.34 depicts a single bond length while the peak for x = 0.21 is mishappen and contains signal from multiple bond lengths. x = 0.58 displays two peaks within the 1 to 2 Å radial range and is the clearest indication of multiple bond lengths in MCO-region samples. Multiple lengths appearing in out-of-plane manganese spectra would come about in the case of mixed Mn^{3+} and Mn^{4+} character since Mn^{3+} octahedra will distort to longer bond lengths due to JT distortion alongside undistorted Mn^{3+} octahedra. Thus, the existence of multiple bond lengths in out-of-plane manganese spectra shows the octahedral coordination of manganese cations in MCO-region samples.

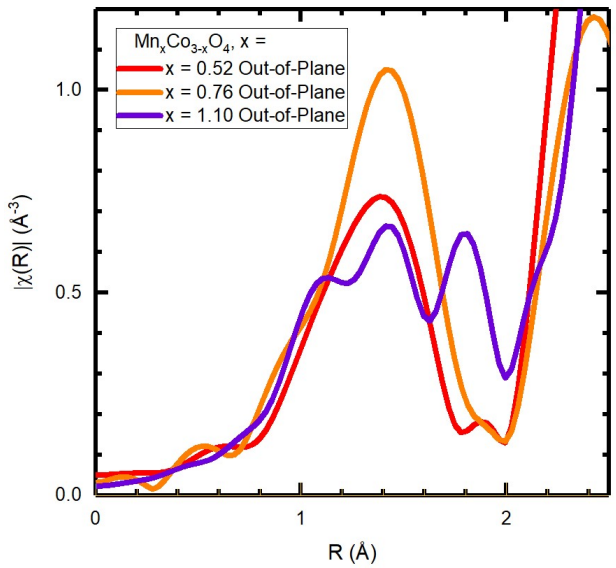

Figure 5.9 Transformed XAS EXAFS plots of out-of-plane manganese spectra for three $Mn_xCo_{3-x}O_4$ samples.

Similar to how fitting was performed for Co_3O_4, two Co-O bond lengths were assumed to exist in MCO-region samples- one for tetrahedral coordination and one for octahedral. This follows from the idea that additional manganese occupies octahedral coordination in the spinel structure thereby allowing a dual-coordination cobalt structure to persist as it does in Co_3O_4. Co-O bond lengths determined for MCO-region samples are shown in Table 5.5 along with those determined for CMO. Bond lengths of MCO-region samples did not significantly deviate from those determined in Co_3O_4 despite the addition of manganese, particularly in the case of in-plane cobalt spectra. This reflects the similar shapes of Co-region XAS spectra between samples. The fact that cobalt bond lengths are relative close between samples indicates that MCO-region samples maintain a similar cobalt polyhedra fine structure to that of Co_3O_4. This leaves manganese cations to drive the majority of material property changes as a function of stoichiometry. The reason for an increased bond length of 1.94 Å in x = 1.02 and x = 1.10 is not known but these

higher-manganese stoichiometry samples show phase segregation while the lower manganese samples are single-phase. Cobalt bond lengths in CMO samples are higher than those of MCO-region samples (ranging from 1.96 Å to 1.98 Å), and a length of 1.94 Å could follow from a stoichiometry transition from $MnCo_2O_4$ towards $CoMn_2O_4$ in which Co-O lengths increase.

Fitting for Mn-O bond lengths was performed using models that placed manganese cations in octahedral coordination only, and results are shown in Table 5.5. Bond lengths could be determined for all in-plane manganese spectra, but most out-of-plane spectra could not be fit due to spectra showing multiple bond lengths. Mixed valence character between Mn^{3+} and Mn^{4+} in samples is a likely contributor to multiple bond lengths through JT distortion stretching Mn^{3+} octahedra but not Mn^{4+}, although phase segregation causing other structural changes in the sample lattices may also contribute. Fitting cobalt spectra for multiple Co-O bond lengths was achievable because the ratio of tetrahedral cobalt to octahedral cobalt was known based on sample stoichiometry, and scattering paths could be weighted properly. However, there was no way to determine the ratio of Mn^{3+} to Mn^{4+} cations using methods within the scope of this study and thus scattering paths would never be weighted properly.

Mn in-plane spectra were able to be fit in a straight-forward manner and showed consistent bond lengths between the values of 1.89 Å and 1.90 Å for all samples regardless of stoichiometry or phase behavior. This is interesting considering the vast differences in out-of-plane spectra in which multiple bond lengths are present due to samples possessing both Mn^{3+} and Mn^{4+} character. This means that both types of octahedra have relatively close in-plane bond lengths regardless of their out-of-plane lengths, although this may be due in part to lattice strain. The theoretical bond lengths based on ionic radii for Mn^{3+} and Mn^{4+} octahedra are 1.91 Å and either 1.96 Å (low spin) or 2.025 Å (high spin), respectively [58]. Therefore, these experimental bond lengths determined

in EXAFS fitting make sense in the case of Mn^{4+} octahedra, but not in the case of Mn^{3+} octahedra. However, JT distortion acts to distort Mn^{3+} octahedra and lead to bond lengths that are longer out-of-plane and shorter in-plane. Bond lengths associated with distorted Mn^{3+} octahedra were already determined from EXAFS fitting of CMO in which fits of in-plane manganese spectra gave Mn-O lengths between 1.91 Å and 1.92 Å. This explains why in-plane spectra of MCO-region samples with mixed Mn^{3+} and Mn^{4+} character can be fit with a single bond length. This also follows from the fact that all in-plane manganese XAS spectra have similar shapes regardless of stoichiometry or valence character.

There is one MCO-region sample, x = 0.76, that does not show multiple bond lengths in its out-of-plane manganese spectrum and can be fit in a straightforward manner. This sample shows in-plane and out-of-plane bond length values of 1.90 Å and 1.91 Å, respectively, both of which correspond closely to theoretical bond lengths for Mn^{4+} [58]. This indicates, as other analyses of this study do, that this single-phase sample exhibits primarily Mn^{4+} character and no Mn^{3+}. While its stoichiometry is Co-rich, this MCO-region sample shows no mixed valence character and may exemplify what ideal $MnCo_2O_4$ would look like in terms of cation valence, namely a manganese valence state of 4+.

Table 5.5 Bond lengths determined by EXAFS for MCO-region samples and CMO samples.

Sample	Co in-plane (Å)		Co out-of-plane (Å)		Mn in-plane (Å)		Mn out-of-plane (Å)	
$Mn_xCo_{3-x}O_4$, x =	Tetra. Coord.	Octa. Coord.	Tetra. Coord.	Octa. Coord.	Tetra. Coord.	Octa. Coord.	Tetra. Coord.	Octa. Coord.
2.08	1.98	-	1.96	-	-	1.92	-	2.23
1.99	1.97	-	1.96	-	-	1.91	-	2.22
1.86	1.97	-	1.96	-	-	1.91	-	2.23
1.10	1.92	1.91	1.90	1.94	-	1.89	-	Multiple
1.02	1.92	1.91	1.94	1.92	-	1.89	-	Multiple
0.84	1.91	1.90	1.91	1.91	-	1.90	-	Multiple
0.76	1.92	1.90	1.92	1.90	-	1.90	-	1.91
0.52	1.91	1.90	1.92	1.90	-	1.90	-	Multiple
Co_3O_4	1.91	1.90	1.92	1.91	-	-	-	-

5.5 Further Discussion

All analyses suggest that manganese in the MCO-region samples of this study are octahedrally coordinated but also show mixed manganese valence character between Mn^{3+} and Mn^{4+}. While other studies of MCO report mixed valence character as well [51,53–55], an ideal spinel should generally show single valence states for each cation meaning that mixed-valence character is a reflection of defects in the material. OOP XRD c-lattice parameters steadily increase with the addition of manganese indicating the action of JT distorted Mn^{3+} octahedra. Co-region XANES pre-edge peaks show consistent high intensity indicating that tetrahedral sites are occupied by cobalt cations leaving manganese to occupy octahedra. The appearance of a pre-edge feature in out-of-plane Mn-region XANES spectra indicates Mn^{3+} octahedra in MCO-region samples, since CMO also shows this feature and contains only Mn^{3+} octahedra. Transformed EXAFS spectra for out-of-plane manganese spectra show multiple nearest-neighbor oxygen bond lengths which most likely comes from the simultaneous occupation of octahedral sites with both Mn^{3+} and Mn^{4+} cations. This octahedral coordination of manganese also confirms the inverse-type

spinel nature of MCO and stoichiometry-varied samples from Co_3O_4 to Mn-rich MCO. While Mn^{3+} may not be the ideal manganese valence for single-phase MCO, the fact that samples show this character allows the octahedral coordination of manganese to be observed in this study, primarily through the act of JT distortion.

It was discussed earlier that phase segregation trends with increasing Mn-content in MCO-region samples. As phase segregation has been observed in the material before [12,59], this supports the suggestion that a stable single-phase version of ideal $MnCo_2O_4$ may be difficult to synthesize or does not exist entirely. However, a possible contributing factor to phase segregation in these samples are varying oxygen conditions during sample growth. Figure 5.10 shows oxygen pressures during growth as a function of stoichiometry, with samples' phase behavior also indicated. It can be seen that phase segregation trends with increasing manganese content, however segregation also trends with oxygen pressure used during growth. All multi-phase samples were grown at oxygen pressures below 2.5E-5 Torr while only single-phase samples were grown at oxygen pressures ~3.0E-5 Torr. This indicates that phase segregation may have taken place due to insufficient oxygen reactivity during sample growth. If this is true, the mechanism may be in the formation of mixed-valence samples with both Mn^{3+} and Mn^{4+} in octahedral sites. Mixed-valence character was seen in most samples grown below 2.5E-5 Torr oxygen pressure, and insufficient oxygen reactivity would act to reduce cation valences due to the lower number of of O^{2-} atoms in the material. Mn^{3+} and Mn^{4+} octahedra show significantly different out-of-plane bond lengths due to JT distortion effects, and these differently shaped polyhedra lead to opposing tetragonal and cubic crystal structures, respectively. If multiple manganese valences form during growth, separate regions comprised predominately Mn^{3+} and Mn^{4+} may concurrently form and naturally cause phase segregation due to physical incompatibilities between tetragonal and cubic structures.

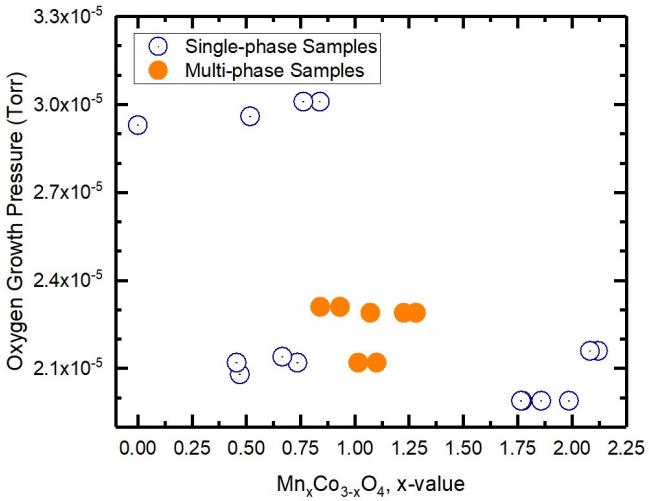

Figure 5.10 Oxygen pressure during sample growth as a function of $Mn_xCo_{3-x}O_4$ stoichiometry. Single-phase samples are marked in blue while multiphase samples are marked in orange.

From the findings of this study, it cannot be stated with certainty that a single-crystalline phase of $MnCo_2O_4$ exists or what its properties would be. The sample closest to this stoichiometry is the $Mn_xCo_{3-x}O_4$ sample x = 1.02 which shows both phase segregation and mixed-valence character between Mn^{3+} and Mn^{4+}. However, a key sample in this study is the single-phase MCO-region material with x = 0.76 and shows solely Mn^{4+} character with no Mn^{3+}. In this sample, out-of-plane manganese XANES shows no indication of a pre-edge feature associated with Mn^{3+} as CMO spectra show. EXAFS fitting shows near-identical Mn-O bond lengths for both in-plane and out-of-plane polarization spectra, the values of which correspond closely to Mn^{4+} octahedra. First derivative XAS also suggests the sample shows predominately Mn^{4+} character. The fact that the sample of this study that shows only Mn^{4+} character was also grown at relatively higher oxygen pressures is no coincidence. The higher oxygen reactivity during growth helped to prevent the reduction of manganese cations from Mn^{4+} to Mn^{3+} as seen in most other MCO-region samples.

OOP XRD also shows that the c-lattice parameter of sample x = 0.76 is far lower than those of other MCO-region samples. This is because the (004) spinel diffraction peak is convolved with the MAO substrate peak, meaning the film's c-parameter is slightly higher than the substrate's value of 8.083 Å. Lower lattice parameters have been reported previously for ideal MCO [134–136] with values trending as low as 8.09 Å. This suggests that the sample x = 0.76 is closer in lattice parameter to true, single-phase MCO than the other MCO-region samples of this study which show greater lattice parameters. It was discussed earlier how these other MCO-region samples show higher c-lattice parameters due to the effects of JT distortion and polyhedral stretching of octahedral Mn^{3+}. Thus, Mn^{4+} seems to be the characteristic valence of ideal MCO while Mn^{3+} represents valence state defects. These defects then act to drive the material into larger lattice parameters through JT distortion, and potential phase segregation in the case simultaneous Mn^{3+} and Mn^{4+} character.

While sample x = 0.76 is Co-rich, its single-phase, single-valence and smaller lattice parameter suggests that ideal $MnCo_2O_4$ does have a stable single-crystalline phase with a manganese valence of Mn^{4+}. Additionally, XPS and XAS shows a trend in cobalt valence from mixed 2+ and 3+ towards Co^{2+} with increased manganese stoichiometry for MCO-region samples. Also, a Co^{2+} valence is required for the purposes of charge balancing in the case of Mn^{4+} cations. This indicates that alongside Mn^{4+} octahedra, ideal MCO would have Co^{2+} character with cobalt occupying tetrahedral sites. In this way, Mn^{2+}, Mn^{3+} or Co^{3+} reflect valence state defects in the material that may come about due to insufficient oxygen conditions during synthesis of MCO. This would mean that studies showing mixed-valence character or phase segregation [12,51,53–55,59] involve non-ideal MCO and should be reviewed with this in mind. Surprisingly, MCO is not known to be a 4-2 spinel in literature and this seems to be the first study to report this.

A transition from ideal $MnCo_2O_4$ (Mn^{4+} and Co^{2+}) towards $CoMn_2O_4$ (Co^{2+} and Mn^{3+}) would see the replacing of Co^{2+} octahedra with Mn^{3+} octahedra in the spinel structure, along with the reduction of other Mn^{4+} octahedra into Mn^{3+} in order to maintain charge balancing. While MCO appears to possess a cubic crystal structure with non-JT-active Mn^{4+} octahedra, CMO exhibits a tetragonal structure due to its distorted Mn^{3+} octahedra. Due to the incompatibility between cubic and tetragonal c-lattice parameters, the transition in stoichiometry from MCO towards CMO and replacing of Mn^{4+} with Mn^{3+} in octahedral sites would see material structures that likely do not have a stable single phase. Instead, the coexistence of Mn^{4+} and Mn^{3+} may lead to regions of cubic and tetragonal structure that would favor phase segregation over a homogenous structure.

Future studies involving MCO and the cobalt-manganese spinel system could involve the synthesis of MCO-region samples at higher oxygen reactivity, using OOP XRD to determine c-lattice parameters and check for phase segregation, and performing XAS experiments to check for mixed-valence character and confirm Mn^{4+} valences through EXAFS fitting. Lower lattice parameters would follow from the absence of JT-active Mn^{3+} octahedral defect sites, and bond lengths that are similar in both in-plane and out-of-plane polarization spectra indicate undistorted manganese spectra that are occupied by Mn^{4+}. An investigation of the transition from MCO to CMO could involve the successful synthesis of Mn-rich MCO and Co-rich CMO to identify the stoichiometries where samples show phase segregation due to incompatible cubic and tetragonal structures.

5.6 Conclusion

This study is the first to synthesize and study MCO-region samples using MBE, and one of the only studies of MCO oriented towards thin films. The samples studied include ideal

stoichiometry $MnCo_2O_4$ and $Mn_xCo_{3-x}O_4$ with x-values ranging from 0 to 1.28. The samples show increasing c-lattice parameters and phase segregation tendencies with additional manganese content. Cobalt valence character also trends towards Co2+ from mixed 2+ and 3+ with increasing manganese. While most samples suggest mixed manganese valence between 3+ and 4+, Mn^{3+} character likely represents valence state defects in MCO-region samples with Mn^{4+} being the proper valence. This means the single-phase valence states of $MnCo_2O_4$ are likely Mn^{4+} and Co^{2+} as opposed to Mn^{2+} and Co^{3+} like most other spinels would show. Mn^{3+} character in MCO-region samples is likely due to insufficient oxygen reactivity during growth. While Mn^{3+} is likely an improper valence state in MCO, it allowed for the observation of manganese cations in octahedral coordination predominately through the effects of JT distortion of Mn^{3+} octahedra. It is this JT distortion of Mn^{3+} octahedra that contributes to the large increases in c-lattice parameters of MCO-region samples. Mixed manganese valence between 3+ and 4+ also likely incites phase segregation in MCO-region samples, where Mn^{4+} and Mn^{3+} octahedra are associated with incompatible cubic and tetragonal crystal structures, respectively. For this reason, MCO-region samples that show proper Mn^{4+} valence states with minimal Mn^{3+} defects would lead to single-phase cubic spinel structures with octahedrally coordinated Mn^{4+} along with Co^{2+} cations.

References:

[1] Cheng F, Shen J, Peng B, Pan Y, Tao Z and Chen J 2011 Rapid room-temperature synthesis of nanocrystalline spinels as oxygen reduction and evolution electrocatalysts *Nat. Chem.* **3** 79–84

[2] Li Y and Lu J 2017 Metal–Air Batteries: Will They Be the Future Electrochemical Energy Storage Device of Choice? *ACS Energy Lett.* **2** 1370–7

[3] Antolini E 2014 Iridium As Catalyst and Cocatalyst for Oxygen Evolution/Reduction in Acidic Polymer Electrolyte Membrane Electrolyzers and Fuel Cells *ACS Catal.* **4** 1426–40

[4] Li C, Han X, Cheng F, Hu Y, Chen C and Chen J 2015 Phase and composition controllable synthesis of cobalt manganese spinel nanoparticles towards efficient oxygen electrocatalysis *Nat. Commun.* **6** 1–8

[5] Bruce P G, Freunberger S A, Hardwick L J and Tarascon J-M 2011 Li-O2 and Li-S batteries with high energy storage *Nat. Mater.* **11** 19–29

[6] Malavasi L, Fisher C A J and Islam M S 2010 Oxide-ion and proton conducting electrolyte materials for clean energy applications: structural and mechanistic features *Chem. Soc. Rev.* **39** 4370–87

[7] Kinoshita K 1992 Electrochemical Oxygen Technology

[8] Debe M K 2012 Electrocatalyst approaches and challenges for automotive fuel cells *Nature* **486** 43–51

[9] Steele B C H and Heinzel A 2001 Materials for fuel-cell technologies *Nature* **414** 345–52

[10] Cong H N, Abbassi K E and Chartier P 2002 Electrocatalysis of Oxygen Reduction on Polypyrrole/Mixed Valence Spinel Oxide Nanoparticles *J. Electrochem. Soc.* **149** A525–30

[11] Rios E, Gautier J-L, Poillerat G and Chartier P 1998 Mixed valency spinel oxides of transition metals and electrocatalysis: case of the MnxCo3−xO4 system *Electrochimica Acta* **44** 1491–7

[12] Yang Y, Xiong Y, Holtz M E, Feng X, Zeng R, Chen G, DiSalvo F J, Muller D A and Abruña H D 2019 Octahedral spinel electrocatalysts for alkaline fuel cells *Proc. Natl. Acad. Sci.* **116** 24425–32

[13] Liang Y, Wang H, Zhou J, Li Y, Wang J, Regier T and Dai H 2012 Covalent Hybrid of Spinel Manganese–Cobalt Oxide and Graphene as Advanced Oxygen Reduction Electrocatalysts *J. Am. Chem. Soc.* **134** 3517–23

[14] McClure D S 1957 The distribution of transition metal cations in spinels *J. Phys. Chem. Solids* **3** 311–7

[15] Zhu H, Zhang S, Huang Y-X, Wu L and Sun S 2013 Monodisperse MxFe3–xO4 (M = Fe, Cu, Co, Mn) Nanoparticles and Their Electrocatalysis for Oxygen Reduction Reaction *Nano Lett.* **13** 2947–51

[16] Li Z, Gao K, Han G, Wang R, Li H, Zhao X S and Guo P 2014 Solvothermal synthesis of MnFe2O4 colloidal nanocrystal assemblies and their magnetic and electrocatalytic properties *New J. Chem.* **39** 361–8

[17] Hu L, Zhong H, Zheng X, Huang Y, Zhang P and Chen Q 2012 CoMn2O4 Spinel Hierarchical Microspheres Assembled with Porous Nanosheets as Stable Anodes for Lithium-ion Batteries *Sci. Rep.* **2**

[18] Zhou L, Zhao D and Lou X W 2012 Double-shelled CoMn2O4 hollow microcubes as high-capacity anodes for lithium-ion batteries *Adv. Mater. Deerfield Beach Fla* **24** 745–8

[19] Li J, Xiong S, Li X and Qian Y 2013 A facile route to synthesize multiporous MnCo2O4 and CoMn2O4 spinel quasi-hollow spheres with improved lithium storage properties *Nanoscale* **5** 2045–54

[20] Kim M H, Hong Y J and Kang Y C 2013 Electrochemical properties of yolk–shell and hollow CoMn2O4 powders directly prepared by continuous spray pyrolysis as negative electrode materials for lithium ion batteries *RSC Adv.* **3** 13110–4

[21] Zhang K, Han X, Hu Z, Zhang X, Tao Z and Chen J 2015 Nanostructured Mn-based oxides for electrochemical energy storage and conversion *Chem. Soc. Rev.* **44** 699–728

[22] Tareen A K, Priyanga G S, Khan K, Pervaiz E, Thomas T and Yang M 2019 Nickel-Based Transition Metal Nitride Electrocatalysts for the Oxygen Evolution Reaction *ChemSusChem* **12** 3941–54

[23] St. Laurent J B, de Buzzaccarini F, De Clerck K, Demeyere H, Labeque R, Lodewick R and van Langenhove L 2007 B.1.I - Laundry Cleaning of Textiles *Handbook for Cleaning/Decontamination of Surfaces* ed I Johansson and P Somasundaran (Amsterdam: Elsevier Science B.V.) pp 57–102

[24] Ramaswamy N and Mukerjee S 2012 Fundamental Mechanistic Understanding of Electrocatalysis of Oxygen Reduction on Pt and Non-Pt Surfaces: Acid versus Alkaline Media *Adv. Phys. Chem.* **2012** e491604

[25] Ma R, Lin G, Zhou Y, Liu Q, Zhang T, Shan G, Yang M and Wang J 2019 A review of oxygen reduction mechanisms for metal-free carbon-based electrocatalysts *Npj Comput. Mater.* **5** 1–15

[26] Anderson A B, Roques J, Mukerjee S, Murthi V S, Markovic N M and Stamenkovic V 2005 Activation Energies for Oxygen Reduction on Platinum Alloys: Theory and Experiment *J. Phys. Chem. B* **109** 1198–203

[27] Vielstich W, Lamm A and Gasteiger H 2003 Handbook of fuel cells. Fundamentals, technology, applications

[28] Agusu L, Alimin, Ahmad L O, Firihu M Z, Mitsudo S and Kikuchi H 2019 Crystal and microstructure of MnFe2O4 synthesized by ceramic method using manganese ore and iron sand as raw materials *J. Phys. Conf. Ser.* **1153** 012056

[29] Long X-Y, Li J-Y, Sheng D and Lian H-Z 2017 Spinel-type manganese ferrite (MnFe2O4) microspheres: A novel affinity probe for selective and fast enrichment of phosphopeptides *Talanta* **166** 36–45

[30] Nguyen T, Boudard M, Rapenne L, Chaix-Pluchery O, Carmezim M J and Montemor M F 2015 Structural evolution, magnetic properties and electrochemical response of MnCo2O4 nanosheet films *RSC Adv.* **5** 27844–52

[31] Sanad M M S, Yousef A K, Rashad M M, Naggar A H and El-Sayed A Y 2020 Robust and facile strategy for tailoring CoMn2O4 and MnCo2O4 structures as high capacity anodes for Li-ions batteries *Phys. B Condens. Matter* **579** 411889

[32] Boucher B, Buhl R and Perrin M 1968 Magnetic Structure of Cobalt Manganite by Neutron Diffraction *J. Appl. Phys.* **39** 632–4

[33] Das D, Biswas R and Ghosh S 2016 Systematic analysis of structural and magnetic properties of spinel CoB2O4 (B = Cr, Mn and Fe) compounds from their electronic structures. *J. Phys. Condens. Matter* **28** 446001

[34] Goodenough J B, Wold A, Arnott R J and Menyuk N 1961 Relationship between crystal symmetry and magnetic properties of ionic compounds containing Mn3+ *Phys. Rev.* **124** 373–84

[35] Goodenough J B and Loeb A L 1955 Theory of Ionic Ordering, Crystal Distortion, and Magnetic Exchange Due to Covalent Forces in Spinels *Phys. Rev.* **98** 391–408

[36] Shoemaker D P, Li J and Seshadri R 2009 Unraveling atomic positions in an oxide spinel with two Jahn-Teller ions: local structure investigation of CuMn2O4 *J. Am. Chem. Soc.* **131** 11450–7

[37] Orgel L E and Dunitz J D 1957 Stereochemistry of Cupric Compounds *Nature* **179** 462–5

[38] Jahn H A, Teller E and Donnan F G 1937 Stability of polyatomic molecules in degenerate electronic states - I—Orbital degeneracy *Proc. R. Soc. Lond. Ser. - Math. Phys. Sci.* **161** 220–35

[39] Housecroft C E and Sharpe A G 2005 *Inorganic Chemistry* (Harlow: Pearson Education Limited)

[40] Brik M G, Suchocki A and Kamińska A 2014 Lattice Parameters and Stability of the Spinel Compounds in Relation to the Ionic Radii and Electronegativities of Constituting Chemical Elements *Inorg. Chem.* **53** 5088–99

[41] Blanchet M D, Heath J J, Kaspar T C, Matthews B E, Spurgeon S R, Bowden M E, Heald S M, Issacs-Smith T, Kuroda M A and Comes R B 2021 Electronic and structural properties of single-crystal Jahn–Teller active Co1+xMn2-xO4 thin films *J. Phys. Condens. Matter* **33** 124002

[42] Suchow L 1976 A detailed, simple crystal field consideration of the normal spinel structure of Co3O4 *J. Chem. Educ.* **53** 560

[43] Dunitz J D and Orgel L E 1957 Electronic properties of transition-metal oxides-II: Cation distribution amongst octahedral and tetrahedral sites *J. Phys. Chem. Solids* **3** 318–23

[44] Mo S-D and Ching W Y 1996 Electronic structure of normal, inverse, and partially inverse spinels in the MgAl2O4 system *Phys. Rev. B* **54** 16555–61

[45] Spencer C D and Schroeer D 1974 Mössbauer study of several cobalt spinels using Co57 and Fe57 *Phys. Rev. B* **9** 3658–65

[46] Pelton A D, Schmalzried H and Sticher J 1979 Thermodynamics of Mn3O4 — Co3O4, Fe3O4 — Mn3O4, and Fe3O4 — Co3O4 Spinels by Phase Diagram Analysis *Berichte Bunsenges. Für Phys. Chem.* **83** 241–52

[47] Goodarz Naseri M, Saion E B and Kamali A 2012 An Overview on Nanocrystalline ZnFe2O4, MnFe2O4, and CoFe2O4 Synthesized by a Thermal Treatment Method *ISRN Nanotechnol.* **2012** e604241

[48] Singh S, Pramanik P, Sangaraju S, Mallick A, Giebeler L and Thota S 2017 Size-dependent structural, magnetic, and optical properties of MnCo2O4 nanocrystallites *J. Appl. Phys.* **121** 194303

[49] Kim K J and Heo J W 2012 Electronic structure and optical properties of inverse-spinel MnCo2O4 thin films *J. Korean Phys. Soc.* **60** 1376–80

[50] Liu S, Ni D, Li H-F, Hui K N, Ouyang C-Y and Jun S C 2018 Effect of cation substitution on the pseudocapacitive performance of spinel cobaltite MCo2O4 (M = Mn, Ni, Cu, and Co) *J. Mater. Chem. A* **6** 10674–85

[51] Garg N, Mishra M, Govind and Ganguli A K 2015 Electrochemical and magnetic properties of nanostructured CoMn2O4 and Co2MnO4 *RSC Adv.* **5** 84988–98

[52] Matzen S, Moussy J-B, Mattana R, Bouzehouane K, Deranlot C, Petroff F, Cezar J C, Arrio M-A, Sainctavit Ph, Gatel C, Warot-Fonrose B and Zheng Y 2011 Epitaxial growth and ferrimagnetic behavior of MnFe2O4(111) ultrathin layers for room-temperature spin filtering *Phys. Rev. B* **83** 184402

[53] Zou L, Cheng J, Jiang Y, Gong Y, Chi B, Pu J and Jian L 2016 Spinel MnCo2O4 nanospheres as an effective cathode electrocatalyst for rechargeable lithium–oxygen batteries *RSC Adv.* **6** 31248–55

[54] Mitran G, Chen S and Seo D-K 2020 Selective oxidation of n-buthanol to butyraldehyde over MnCo2O4 spinel oxides *RSC Adv.* **10** 25125–35

[55] Ahuja B L, Dashora A, Heda N L, Tiwari S, Rajeevan N E, Itou M, Sakurai Y and Kumar R 2010 Reversal of orbital magnetic moment on substitution of Bi in multiferroic Co2MnO4: A magnetic Compton scattering study *Appl. Phys. Lett.* **97** 212502

[56] Wood D L and Remeika J P 1967 Optical Absorption of Tetrahedral Co3+ and Co2+ in Garnets *J. Chem. Phys.* **46** 3595–602

[57] Biagioni C and Pasero M 2014 The systematics of the spinel-type minerals: An overview† *Am. Mineral.* **99** 1254–64

[58] Shannon R D 1976 Revised effective ionic radii and systematic studies of interatomic distances in halides and chalcogenides *Acta Crystallogr. A* **32** 751–67

[59] Yang Y, Zeng R, Xiong Y, DiSalvo F J and Abruña H D 2019 Rock-Salt-Type MnCo2O3/C as Efficient Oxygen Reduction Electrocatalysts for Alkaline Fuel Cells *Chem. Mater.* **31** 9331–7

[60] Wu G, Wang J, Ding W, Nie Y, Li L, Qi X, Chen S and Wei Z 2016 A Strategy to Promote the Electrocatalytic Activity of Spinels for Oxygen Reduction by Structure Reversal *Angew. Chem.* **128** 1362–6

[61] Zhou Y, Xi S, Wang J, Sun S, Wei C, Feng Z, Du Y and Xu Z J 2018 Revealing the Dominant Chemistry for Oxygen Reduction Reaction on Small Oxide Nanoparticles *ACS Catal.* **8** 673–7

[62] Huang K, Liu J, Wang L, Chang G, Wang R, Lei M, Wang Y and He Y 2019 Mixed valence CoCuMnOx spinel nanoparticles by sacrificial template method with enhanced ORR performance *Appl. Surf. Sci.* **487** 1145–51

[63] Oh T, Ryu S, Oh H and Kim J 2019 MnCo2O4 nanoparticles supported on nitrogen and sulfur co-doped mesoporous carbon spheres as efficient electrocatalysts for oxygen catalytic reactions *Dalton Trans.* **48** 945–53

[64] Baji D S, Jadhav H S, Nair S V and Rai A K 2018 Porous MnCo2O4 as superior anode material over MnCo2O4 nanoparticles for rechargeable lithium ion batteries *J. Solid State Chem.* **262** 191–8

[65] Thapa S, Provence S R, Jessup D, Lapano J, Brahlek M, Sadowski J T, Reinke P, Jin W and Comes R B 2021 Correlating surface stoichiometry and termination in SrTiO3 films grown by hybrid molecular beam epitaxy *J. Vac. Sci. Technol. A* **39** 053203

[66] Lin S-C, Kuo C-T, Comes R B, Rault J E, Rueff J-P, Nemšák S, Taleb A, Kortright J B, Meyer-Ilse J, Gullikson E, Sushko P V, Spurgeon S R, Gehlmann M, Bowden M E, Plucinski L, Chambers S A and Fadley C S 2018 Interface properties and built-in potential profile of a LaCrO3/SrTiO3 superlattice determined by standing-wave excited photoemission spectroscopy *Phys. Rev. B* **98** 165124

[67] Kaspar T C, Bowden M E, Varga T, Wang C M, Shutthanandan V, Joly A G, Wirth B D and Kurtz R J 2012 Structural characterization of epitaxial CrxMo1-xalloy thin films *J. Phys. Condens. Matter* **24** 095001

[68] Cheng K Y 2013 Development of molecular beam epitaxy technology for III–V compound semiconductor heterostructure devices *J. Vac. Sci. Technol. A* **31** 050814

[69] Uusi-Esko K, Rautama E-L, Laitinen M, Sajavaara T and Karppinen M 2010 Control of Oxygen Nonstoichiometry and Magnetic Property of MnCo2O4 Thin Films Grown by Atomic Layer Deposition *Chem. Mater.* **22** 6297–300

[70] Kwak Y, Song J and Koo T 2016 Growth and giant coercive field of spinel-structured Co3−xMnxO4 thin films *J. Korean Phys. Soc.* **69** 263–7

[71] Kaiser N 2002 Review of the fundamentals of thin-film growth *Appl. Opt.* **41** 3053–60

[72] Chambers S A 2000 Epitaxial growth and properties of thin film oxides *Surf. Sci. Rep.* **39** 105–80

[73] Mishra R K and Thomas G 1977 Surface energy of spinel *J. Appl. Phys.* **48** 4576–80

[74] Bredar A R C, Blanchet M D, Burton A R, Matthews B E, Spurgeon S R, Comes R B and Farnum B H 2022 Oxygen Reduction Electrocatalysis with Epitaxially Grown Spinel MnFe2O4 and Fe3O4 *ACS Catal.* 3577–88

[75] Mahan J E, Geib K M, Robinson G Y and Long R G 1990 A review of the geometrical fundamentals of reflection high-energy electron diffraction with application to silicon surfaces *J. Vac. Sci. Technol. A* **8** 3692–700

[76] Hasegawa S 2012 Reflection High-Energy Electron Diffraction *Characterization of Materials* (John Wiley & Sons, Ltd) pp 1–14

[77] Kumari S, Mottaghi N, Huang C-Y, Trappen R, Bhandari G, Yousefi S, Cabrera G, Seehra M S and Holcomb M B 2020 Effects of Oxygen Modification on the Structural and Magnetic Properties of Highly Epitaxial La0.7Sr0.3MnO3 (LSMO) thin films *Sci. Rep.* **10** 3659

[78] Sorokina K L and Tolstikhina A L 2004 Atomic force microscopy modified for studying electric properties of thin films and crystals. Review *Crystallogr. Rep.* **49** 476–99

[79] Gavara N 2017 A beginner's guide to atomic force microscopy probing for cell mechanics *Microsc. Res. Tech.* **80** 75–84

[80] Tong Y-X, Zhang Q-H and Gu L 2018 Scanning transmission electron microscopy: A review of high angle annular dark field and annular bright field imaging and applications in lithium-ion batteries *Chin. Phys. B* **27** 066107

[81] Prencipe I, Dellasega D, Zani A, Rizzo D and Passoni M 2015 Energy dispersive x-ray spectroscopy for nanostructured thin film density evaluation *Sci. Technol. Adv. Mater.* **16** 025007

[82] Segmüller A, Noyan I C and Speriosu V S 1989 X-ray diffraction studies of thin films and multilayer structures *Prog. Cryst. Growth Charact.* **18** 21–66

[83] Yang P, Liu H, Chen Z, Chen L and Wang J 2014 Unit-cell determination of epitaxial thin films based on reciprocal-space vectors by high-resolution X-ray diffractometry *J. Appl. Crystallogr.* **47** 402–13

[84] Fujii Y 2013 Recent Developments in the X-Ray Reflectivity Analysis for Rough Surfaces and Interfaces of Multilayered Thin Film Materials *J. Mater.* **2013** e678361

[85] LaRose J D, Huang M, Bersch E, Di M, Diebold A C, Consiglio S, Clark R D and Leusink G J 2009 High-Resolution Rutherford Backscattering Analysis of Nanoscale Thin Films *AIP Conf. Proc.* **1173** 80–3

[86] Thapa S, Paudel R, Blanchet M D, Gemperline P T and Comes R B 2021 Probing surfaces and interfaces in complex oxide films via in situ X-ray photoelectron spectroscopy *J. Mater. Res.* **36** 26–51

[87] Groot F de 2005 Multiplet effects in X-ray spectroscopy *Coord. Chem. Rev.* **249** 31–63

[88] Lotz W 1970 Electron Binding Energies in Free Atoms* *JOSA* **60** 206–10

[89] Biesinger M C, Payne B P, Grosvenor A P, Lau L W M, Gerson A R and Smart R St C 2011 Resolving surface chemical states in XPS analysis of first row transition metals, oxides and hydroxides: Cr, Mn, Fe, Co and Ni *Appl. Surf. Sci.* **257** 2717–30

[90] Gilbert J B, Rubner M F and Cohen R E 2013 Depth-profiling X-ray photoelectron spectroscopy (XPS) analysis of interlayer diffusion in polyelectrolyte multilayers *Proc. Natl. Acad. Sci.* **110** 6651–6

[91] Thapa S, Provence S, Heald S M, Kuroda M A and Comes R B 2021 Surface Stability of SrNbO3+δ Grown by Hybrid Molecular Beam Epitaxy *ArXiv211015341 Cond-Mat*

[92] Comini N, Huthwelker T, Diulus J T, Osterwalder J and Novotny Z 2021 Factors influencing surface carbon contamination in ambient-pressure x-ray photoelectron spectroscopy experiments *J. Vac. Sci. Technol. A* **39** 043203

[93] Zimmermann P, Peredkov S, Abdala P M, DeBeer S, Tromp M, Müller C and van Bokhoven J A 2020 Modern X-ray spectroscopy: XAS and XES in the laboratory *Coord. Chem. Rev.* **423** 213466

[94] Yano J and Yachandra V K 2009 X-ray absorption spectroscopy *Photosynth. Res.* **102** 241

[95] Sarangi R 2013 X-ray absorption near-edge spectroscopy in bioinorganic chemistry: Application to M-O2 systems *Coord. Chem. Rev.* **257** 459–72

[96] Yamamoto T 2008 Assignment of pre-edge peaks in K-edge x-ray absorption spectra of 3d transition metal compounds: electric dipole or quadrupole? *X-Ray Spectrom.* **37** 572–84

[97] Ohta A, Tsuno H, Kagi H, Kanai Y, Nomura M, Zhang R, Terashima S and Imai N 2006 Chemical compositions and XANES speciations of Fe, Mn and Zn from aerosols collected in China and Japan during dust events *Geochem. J.* **40** 363–76

[98] Datta S, Rule A M, Mihalic J N, Chillrud S N, Bostick B C, Ramos-Bonilla J P, Han I, Polyak L M, Geyh A S and Breysse P N 2012 Use of X-Ray Absorption Spectroscopy (XAS) to Speciate Manganese in Airborne Particulate Matter from 5 Counties Across the US *Environ. Sci. Technol.* **46** 3101–9

[99] G. Kirste K, Laassiri S, Hu Z, Stoian D, Torrente-Murciano L, J. Hargreaves J S and Mathisen K 2020 XAS investigation of silica aerogel supported cobalt rhenium catalysts for ammonia decomposition *Phys. Chem. Chem. Phys.* **22** 18932–49

[100] Yildirim B and Riesen H 2013 Coordination and Oxidation State Analysis of Cobalt in Nanocrystalline LiGa5O8by X-ray Absorption Spectroscopy *J. Phys. Conf. Ser.* **430** 012011

[101] Xi L, Schwanke C, Xiao J, Abdi F F, Zaharieva I and Lange K M 2017 In Situ L-Edge XAS Study of a Manganese Oxide Water Oxidation Catalyst *J. Phys. Chem. C* **121** 12003–9

[102] Garcia F A, Kaneko U F, Granado E, Sichelschmidt J, Hölzel M, Duque J G S, Nunes C A J, Amaral R P, Marques-Ferreira P and Lora-Serrano R 2015 Magnetic dimers and trimers in the disordered S=3/2 spin system BaTi1/2Mn1/2O3 *Phys. Rev. B* **91** 224416

[103] Noronha F B 1999 EXAFS as a tool for catalyst characterization: a review of the data analysis methods *Braz. J. Chem. Eng.* **16** 309–17

[104] Desai H B, Hathiya L J, Joshi H H and Tanna A R 2020 Synthesis and Characterization of Photocatalytic MnFe2O4 Nanoparticles *Mater. Today Proc.* **21** 1905–10

[105] Wei C, Feng Z, Baisariyev M, Yu L, Zeng L, Wu T, Zhao H, Huang Y, Bedzyk M J, Sritharan T and Xu Z J 2016 Valence Change Ability and Geometrical Occupation of Substitution Cations Determine the Pseudocapacitance of Spinel Ferrite XFe2O4 (X = Mn, Co, Ni, Fe) *Chem. Mater.* **28** 4129–33

[106] Kuo C-H and Huang M H 2008 Facile Synthesis of Cu2O Nanocrystals with Systematic Shape Evolution from Cubic to Octahedral Structures *J. Phys. Chem. C* **112** 18355–60

[107] Ge X, Sumboja A, Wuu D, An T, Li B, Goh F W T, Hor T S A, Zong Y and Liu Z 2015 Oxygen Reduction in Alkaline Media: From Mechanisms to Recent Advances of Catalysts *ACS Catal.* **5** 4643–67

[108] Permien S, Hain H, Scheuermann M, Mangold S, Mereacre V, Powell A K, Indris S, Schürmann U, Kienle L, Duppel V, Harm S and Bensch W 2013 Electrochemical insertion of Li into nanocrystalline MnFe2O4: a study of the reaction mechanism *RSC Adv.* **3** 23001–14

[109] Zhuang L, Zhang W, Zhao Y, Shen H, Lin H and Liang J 2015 Preparation and Characterization of Fe3O4 Particles with Novel Nanosheets Morphology and Magnetochromatic Property by a Modified Solvothermal Method *Sci. Rep.* **5** 9320

[110] Yamashita T and Hayes P 2008 Analysis of XPS spectra of Fe2+ and Fe3+ ions in oxide materials *Appl. Surf. Sci.* **254** 2441–9

[111] Cerrato J M, Hochella M F, Knocke W R, Dietrich A M and Cromer T F 2010 Use of XPS to Identify the Oxidation State of Mn in Solid Surfaces of Filtration Media Oxide Samples from Drinking Water Treatment Plants *Environ. Sci. Technol.* **44** 5881–6

[112] Koo T Y, Kim J-Y, Jeong Y H and Song J H 2014 Growth and morphological evolution of Co3-xMnxO4 (x = 1, 2) thin films *J. Korean Phys. Soc.* **65** 200–4

[113] Kutty R K N, Kasturi P R, Jaganath J, Padmanapan S, Lee Y S, Meyrick D and Selvan R K 2019 Structural and magnetic properties of CoMn2O4 synthesized by auto combustion method *J. Mater. Sci. Mater. Electron.* **30** 975–81

[114] Barón-González A J, Frontera C, García-Muñoz J L, Roqueta J and Santiso J 2010 Magnetic, structural properties and B-site order of two epitaxial La2CoMnO6films with perpendicular out-of-plane orientation *J. Phys. Conf. Ser.* **200** 092002

[115] Farges F 2005 Ab initio and experimental pre-edge investigations of the Mn K-edge XANES in oxide-type materials *Phys. Rev. B* **71** 155109

[116] Herrero-Martín J, García J, Subías G, Blasco J and Sánchez M C 2005 Polarized x-ray absorption spectra of La1-xSr1+xMnO4: Electronic state of Mn atoms *Phys. Rev. B* **72** 085106

[117] Ravel B, Stern E A, Vedrinskii R I and Kraizman V 1998 Local structure and the phase transitions of BaTiO3 *Ferroelectrics* **206** 407–30

[118] Nelson-Cheeseman B B, Chopdekar R V, Iwata J M, Toney M F, Arenholz E and Suzuki Y 2010 Modified magnetic ground state in NiMn2O4 thin films *Phys. Rev. B* **82** 144419

[119] Sun Z, Yan W, Zhang G, Oyanagi H, Wu Z, Liu Q, Wu W, Shi T, Pan Z, Xu P and Wei S 2008 Evidence of substitutional Co ion clusters in Zn1−xCoxO dilute magnetic semiconductors *Phys. Rev. B* **77** 245208

[120] Gorlin Y, Lassalle-Kaiser B, Benck J D, Gul S, Webb S M, Yachandra V K, Yano J and Jaramillo T F 2013 In Situ X-ray Absorption Spectroscopy Investigation of a Bifunctional Manganese Oxide Catalyst with High Activity for Electrochemical Water Oxidation and Oxygen Reduction *J. Am. Chem. Soc.* **135** 8525–34

[121] Kaspar T C, Droubay T, Heald S M, Nachimuthu P, Wang C M, Shutthanandan V, Johnson C A, Gamelin D R and Chambers S A 2008 Lack of ferromagnetism inn-type cobalt-doped ZnO epitaxial thin films *New J. Phys.* **10** 055010

[122] Habjanič J, Jurić M, Popović J, Molčanov K and Pajić D 2014 A 3D Oxalate-Based Network as a Precursor for the CoMn2O4 Spinel: Synthesis and Structural and Magnetic Studies *Inorg. Chem.* **53** 9633–43

[123] Popović J, Jurić M, Pajić D, Vrankić M, Zavašnik J and Habjanič J 2017 Effect of the Cation Distribution and Microstructure on the Magnetic Behavior of the CoMn2O4 Oxide *Inorg. Chem.* **56** 3983–9

[124] Friš P, Munzar D, Caha O and Dubroka A 2018 Direct observation of double exchange in ferromagnetic La0.7Sr0.3CoO3 by broadband ellipsometry *Phys. Rev. B* **97** 045137

[125] Lu F-H and Dieckmann R 1993 Point defects and cation tracer diffusion in (CoxMn1−x)3−δO4 spinels *Solid State Ion.* **67** 145–55

[126] Kang M, Zhou H, Kang M and Zhou H 2015 Facile Synthesis and Structural Characterization of Co_3O_4 Nanocubes *AIMS Mater. Sci.* **2** 16–27

[127] Chen J, Wu X and Selloni A 2011 Electronic structure and bonding properties of cobalt oxide in the spinel structure *Phys. Rev. B* **83** 245204

[128] Vaz C A F, Henrich V E, Ahn C H and Altman E I 2009 Growth and characterization of thin epitaxial Co3O4(111) films *J. Cryst. Growth* **311** 2648–54

[129] Kormondy K J, Posadas A B, Slepko A, Dhamdhere A, Smith D J, Mitchell K N, Willett-Gies T I, Zollner S, Marshall L G, Zhou J and Demkov A A 2014 Epitaxy of polar semiconductor Co3O4 (110): Growth, structure, and characterization *J. Appl. Phys.* **115** 243708

[130] Vaz C A F, Prabhakaran D, Altman E I and Henrich V E 2009 Experimental study of the interfacial cobalt oxide in Co3O4/α-Al2O3(0001) epitaxial films *Phys. Rev. B* **80** 155457

[131] Cole K M, Kirk D W and Thorpe S J 2021 Co3O4 nanoparticles characterized by XPS and UPS *Surf. Sci. Spectra* **28** 014001

[132] Bai L, Pravica M, Zhao Y, Park C, Meng Y, Sinogeikin S V and Shen G 2012 Charge transfer in spinel Co3O4at high pressures *J. Phys. Condens. Matter* **24** 435401

[133] Bashir A, Shukla S, Lew J H, Shukla S, Bruno A, Gupta D, Baikie T, Patidar R, Akhter Z, Priyadarshi A, Mathews N and Mhaisalkar S G 2018 Spinel Co3O4 nanomaterials for efficient and stable large area carbon-based printed perovskite solar cells *Nanoscale* **10** 2341–50

[134] Mouhib Y, Belaiche M, Briche S, Ferdi C A and Iffer E 2018 Elaboration, characterization and first principle studies of MnCo2O4 nanomaterials prepared from non-standard raw materials *Mater. Res. Express* **6** 035508

[135] Yuvaraj S, Vignesh A, Shanmugam S and Kalai Selvan R 2016 Nitrogen-doped Multi-walled Carbon Nanotubes-MnCo2O4 microsphere as electrocatalyst for efficient oxygen reduction reaction *Int. J. Hydrog. Energy* **41** 15199–207

[136] Krishnan S G, Rahim M H A and Jose R 2016 Synthesis and characterization of MnCo2O4 cuboidal microcrystals as a high performance psuedocapacitor electrode *J. Alloys Compd.* **656** 707–13

Appendix:

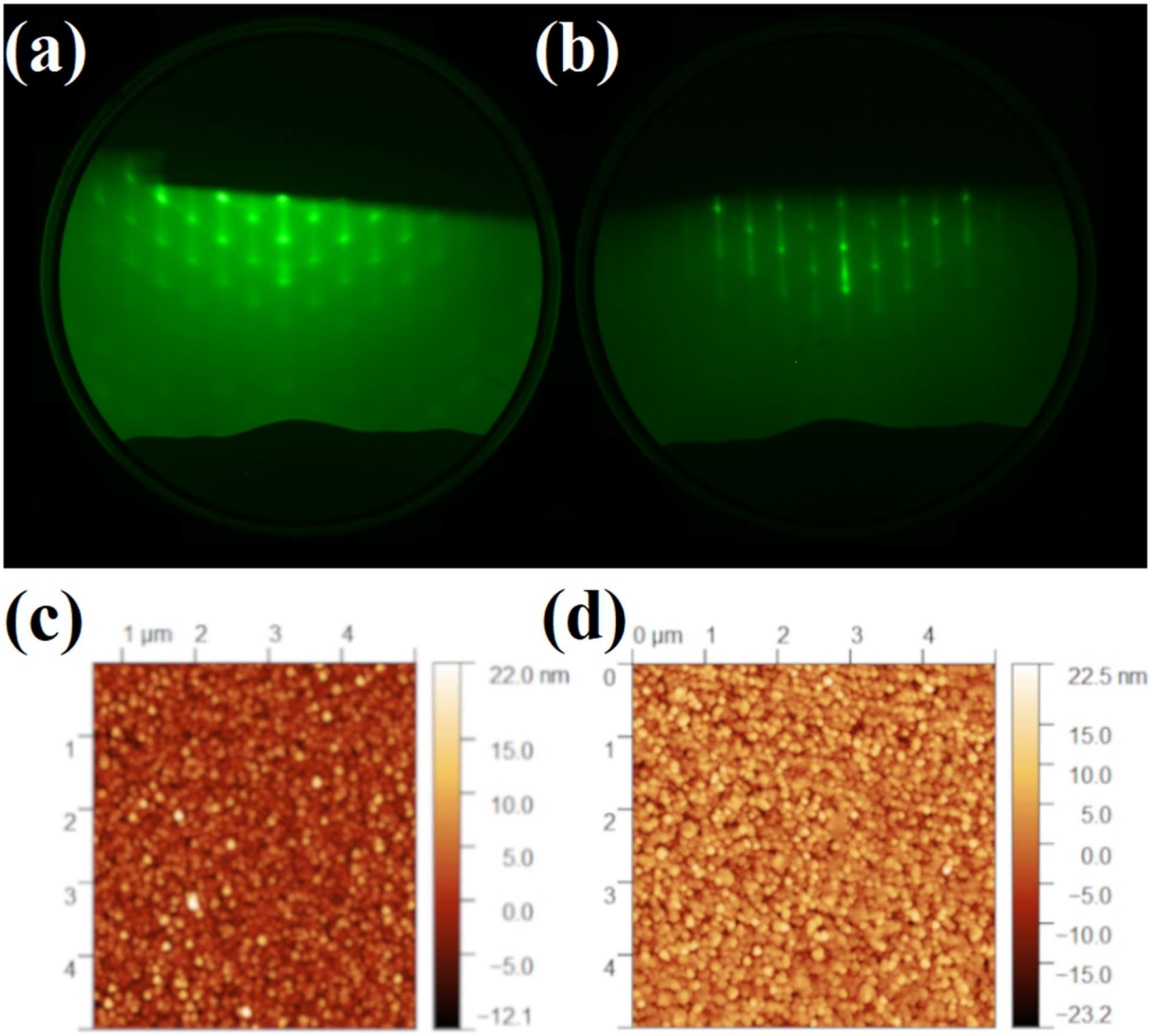

Appendix 1: RHEED and AFM of the (a,c) 16 nm MFO sample and (b,d) 21 nm Fe_3O_4 sample.

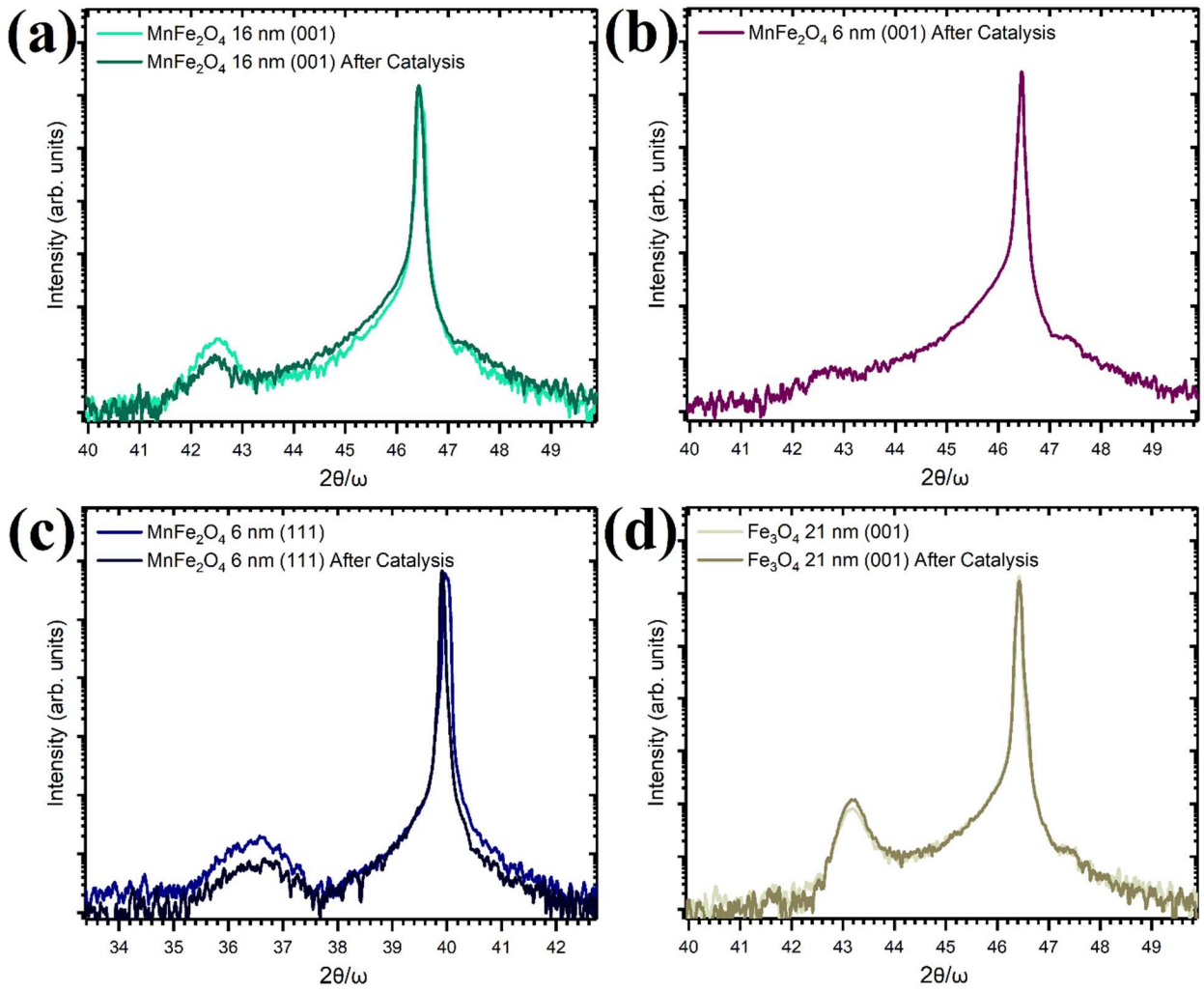

Appendix 2: XRD of MFO and Fe_3O_4 both before and after catalysis experiments were performed on the samples (missing one before-catalysis measurement).

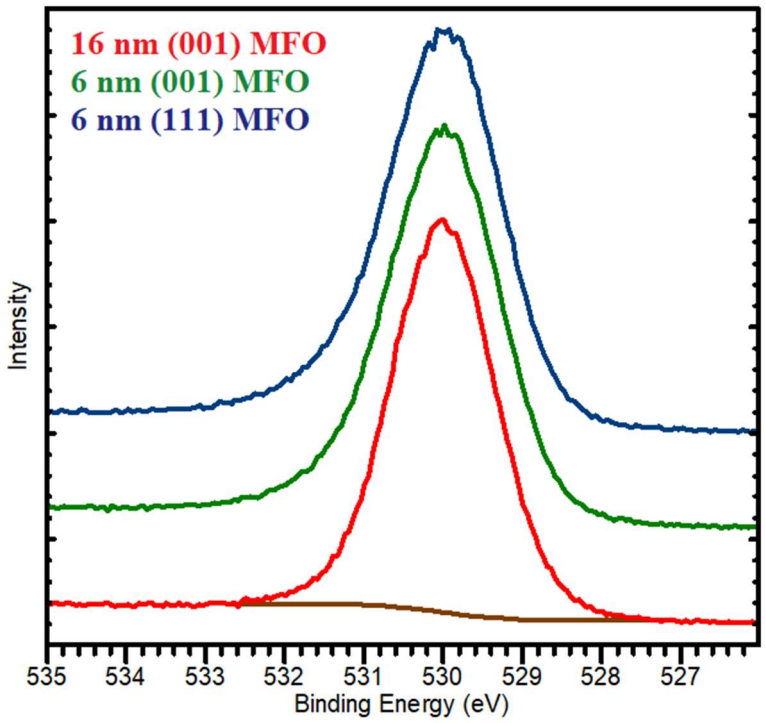

Appendix 3: XPS O 1s region spectra of all MFO samples while under vacuum. All spectra appropriately shifted to place O 1s peaks to 530 eV.

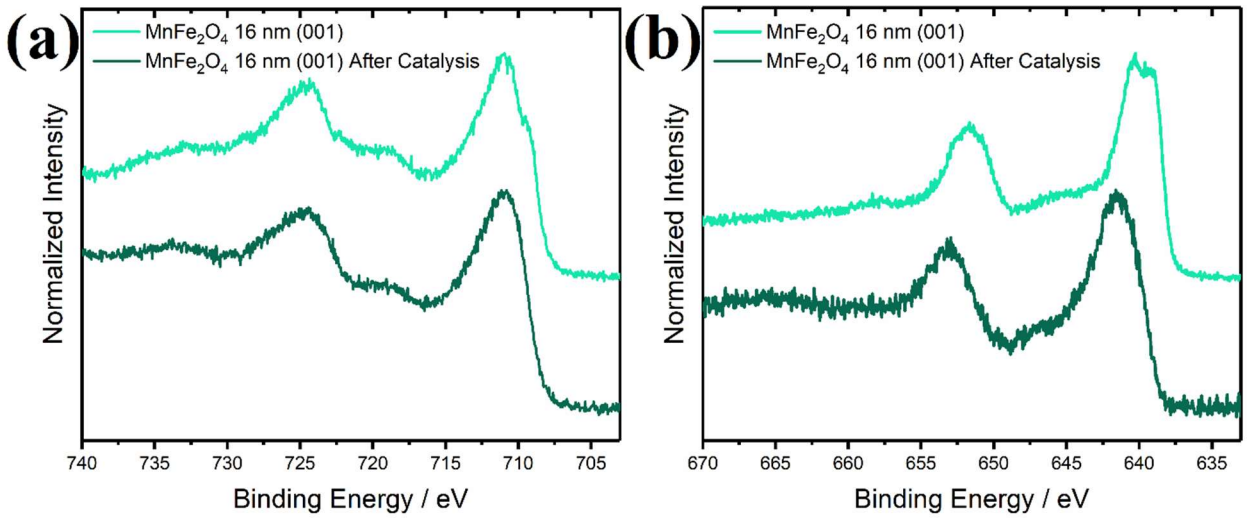

Appendix 4: XPS (a) Fe 2p and (b) Mn 2p region spectra of the 16 nm MFO sample before and after catalysis experiments were performed. Fe^{3+} and Mn^{2+} valence states remain unchanged.

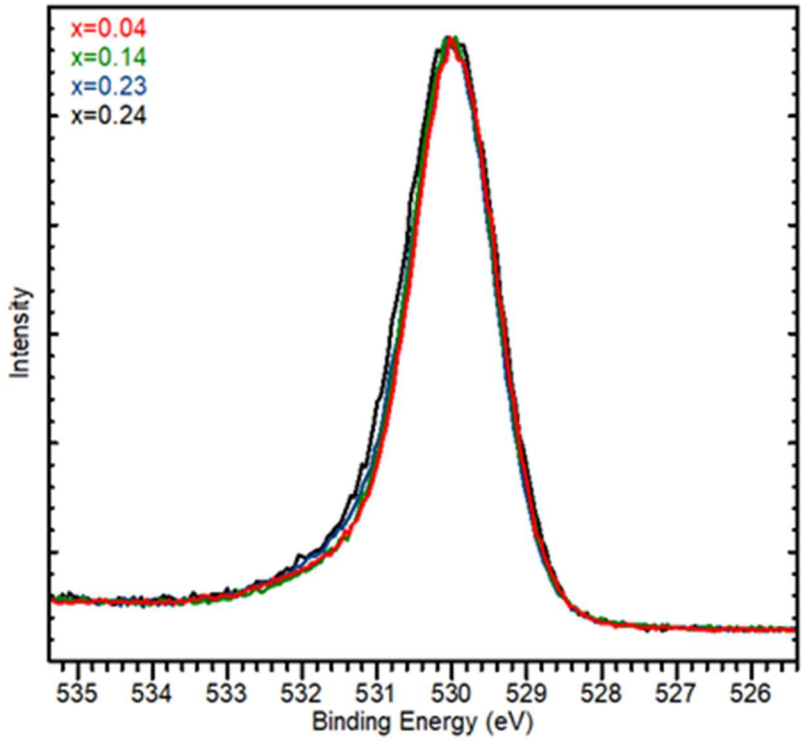

Appendix 5: XPS O 1s region spectra of all CMO samples while under vacuum. All spectra appropriately shifted to place O 1s peaks to 530 eV.

$Co_{1+x}Mn_{2-x}O_4$ Sample	**Thickness (Å)**
x = 0.04	127
x = 0.14	84
x = 0.23	104
x = 0.24	120

Appendix 6: $Co_{x+1}Mn_{2-x}O_4$ sample thicknesses. All were determined with RBS data except for the case of x = 0.24 which was determined with XRR data. These thicknesses were used to fit spectroscopic ellipsometry data.

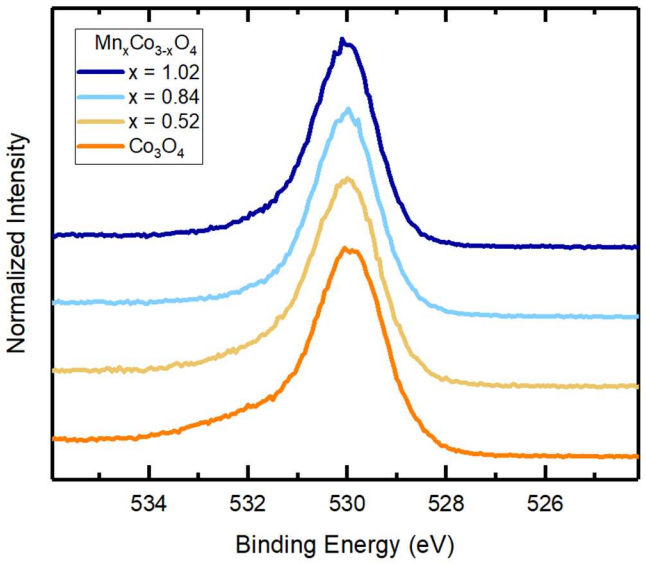

Appendix 7: XPS O 1s region spectra of all MCO samples while under vacuum. All spectra appropriately shifted to place O 1s peaks to 530 eV.